Modélisation et optimisation de capteurs de pression piézorésistifs

Michal Olszacki

To cite this version:

Michal Olszacki. Modélisation et optimisation de capteurs de pression piézorésistifs. Micro et nanotechnologies/Microélectronique. INSA de Toulouse, 2009. Français. NNT : . tel-00432886

HAL Id: tel-00432886
https://theses.hal.science/tel-00432886

Submitted on 17 Nov 2009

THÈSE

En vue de l'obtention du

DOCTORAT DE L'UNIVERSITÉ DE TOULOUSE

Délivré par *INSA de Toulouse*
Discipline ou spécialité : *conception des circuits microelectroniques et microsystemes*

Présentée et soutenue par *Michal Olszacki*
Le *8 juillet 2009*

Titre : *Modelling and optimization of piezoresistive pressure sensors*

JURY
Jean Yves FOURNIOLS, president
Sylvain BALLANDRAS, rapporteur
Jan DZIUBAN, examinateur
Andrzej NAPIERALSKI, directeur de these
Patrick PONS, directeur de these
Robert PUERS, rapporteur

Ecole doctorale : *GEET*
Unité de recherche : *LAAS-CNRS*
Directeur(s) de Thèse : *Patrick PONS*
Andrzej NAPIERALSKI
Rapporteurs : *Sylvain BALLANDRAS*
Robert PUERS

Table of Contents

Preface

This thesis was carried out at Laboratoire d’Analyse et d’Architecture des Systemes (LAAS) in Toulouse, France which is a part of the French National Center for the Scientific Research (CNRS) and at the Department of Microelectronics and Computer Science (DMCS) at Technical University of Lodz, Poland (TUL). All research included in this thesis was conducted in order to obtain the joint diploma between INSA Toulouse, France and Technical University of Lodz, Poland.

Acknowledgments

I would like to express my gratitude to those who inspired and guided me during the course of the Project. I would like to acknowledge Mr. Patrick PONS and Mr. Andrzej NAPIERALSKI for their scientific and personal guidance. Furthermore, I would like to express my gratitude to Mr. Cezary MAJ and Mohamad AL BAHRI for their support. I want to thank also Mr. Lucjan JANOWSKI, Hikmat ACHKAR, David PEYROU and Piotr ZAJAC for fruitful discussions that helped me during the duration of the project. Finally, I would like to acknowledge to my parents: Anna and Roman and also to Agata for their personal support during the redaction of this document.

1 Introduction

1.1 Introduction

When in 1947 the first transistor was introduced, no one could imagine how huge impact it would have on the development of the microtechnologies. While Feyman was rather the pioneer who predicted that “There’s plenty of room at the bottom”, probably even him was rather surprised by the level of the advancement that has taken place after. Since at the beginning semiconductors have been used due to their specific electrical properties, soon the advancement in the fabrication processes offered us the possibility of easy miniaturization of the electronic devices. One may say that forty years ago probably many of us thought that there is no limit in such a process what leaded us to some general laws describing it, including the Moore’s law.

In 1967 [1], Nathanson *et al*. decided to use the existing fabrication processes in order to create not only small electrical devices but also small, very simple mechanical structure which was the resonating MOS gate made of gold that was used in standard processes as the interconnection layer. Such a device opened the discussion about the possible application of the well known technological processes (and relatively simple those days) used for the electronics circuits for the fabrication of simple mechanical structures. Of course, such an approach caused that engineers started to study not only electrical but also mechanical properties of silicon and other materials used for the electronics circuits fabrication. Soon, it became obvious that the silicon is very promising material that may be used for both applications and then, the Microsystems idea arisen.

1.1.1 Microsystems and their economical impact

What are MEMS?

MEMS is an abbreviation for the Micro Electro Mechanical System and, as it indicates, it describes the small scale (ranging from about 0.1µm to a few mm) systems that combines both electrical and mechanical components. In such a system we may have simple mechanical structures like membranes, bridges, cantilevers etc. as well as transistors, resistors, diodes and other electronic components. Such a variety of “low level” devices is then combined in order to create the system level component. The main advantage of such a solution are small dimensions that allow us to fabricate extremely small devices like sensors or actuators. Moreover, we may try to integrate peripherals that are needed to assure them correct operating conditions. Such a combination is called the System on Chip (SoC) which is now an extensively developed approach. The advantages of such a system are numerous like the elimination of long interconnections which occupy space and add some parasitic effects or the possibility of the collective packaging. As the fabrication process is similar to the one used in the microelectronic industry, we are able to fabricate multiple systems at the same time at high yield what drastically reduce costs. Thus, this branch of the microelectronics industry is one of the most expansive one in the last decade.

Moreover, since last few years many functional materials and processes were developed in order to increase the functionality of such microdevices so nowadays, we may easily say that the MEMS branch is almost developing faster than the pure microelectronics industry. The range of applications becomes wider and wider starting with typical “oldest” ones like pressure sensors or accelerometers ending with sophisticated microfluidic lab-on-chips for DNA analysis or microrobots.

Microsystems roadmap

According to the report published in 2006 by NEXUS [2] and Electronics Industry Market Research and Knowledge Network [3], the overall MEMS market was estimated for 5 billion US dollars in 2005 and it is forecasted to grow to 15 billion US dollars in 2012 with the average annual growth rate of about 15%. It may indicate that we are now on the expansive track for the next years and the advancement in research and development of MEMS devices should be impressive. As it is shown in Fig. 1.1, the main domain of today’s MEMS devices are hard disk RW heads as introduction of such elements reduces drastically costs of fabrication. As one can remark, values presented on graph are higher that it was cited and the reason is that for complete systems where, for example in printer heads, not all elements are classified as MEMS. Nevertheless, an important issue is the application area of MEMS, where one of the most promising one is the “life science” domain which covers very wide spectrum of interest like medical applications or biological and chemical science. It has to be said that many research successes in these domains were possible only by using specialized MEMS systems like DNA analyzers or chemical sensors based on functional layers.

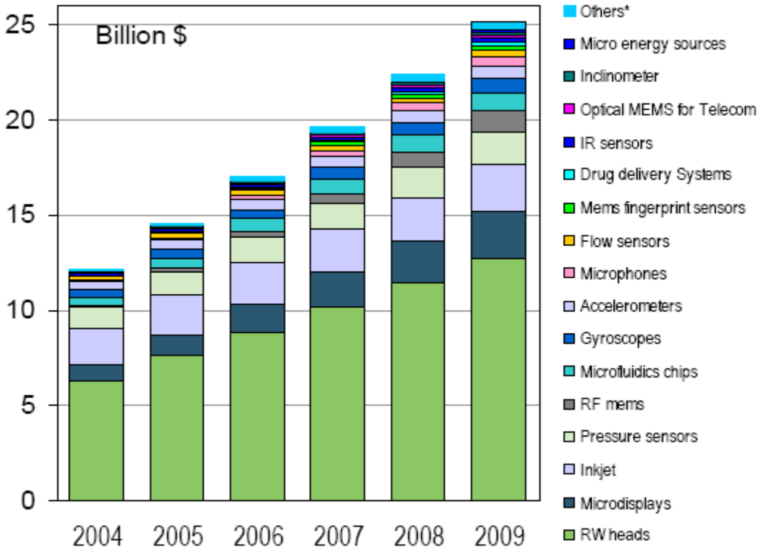

Fig. 1.1 The MEMS market evolution by products category [3].

Also, the medical domain was even affected by the expansion of microtechnologies. According to some reports [4], the MEMS technology opens us the way to use a completely different techniques and methods in diagnosis, surgery and the monitoring of our health. For example, the surgeons need the fast feedback during operation what may be assured by the use of miniaturized sensors. Therefore, the Minimally Invasive Surgery (MIS) idea appeared and it is predicted that in the next 15 years almost 80% of the surgery intervention will be done by using this technique [5,6]. Engineers then applied their imagination and Fig. 1.2 shows us the possible surgery tools that may be used in the near future and which are already in the phase of early development like micro submarine “fighting” with diseases [7].

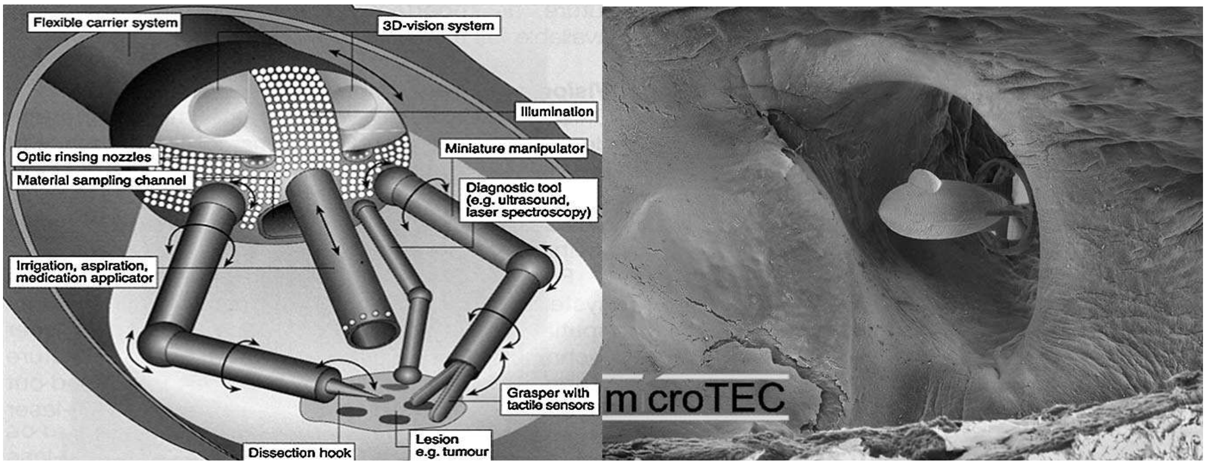

Fig. 1.2 The future surgery tools based on MEMS components [4].

The second important part of medical applications is the diagnosis. There are a lot of attempts in order to develop sensors that may be easily used in the places that are difficult to reach and thus, the small dimension of MEMS is one of the most promising feature in such applications. Of course, there are a lot of chemical, biological and physical sensors that exists but there is still a lot of challenges in medical domain where the environment forces some project constraints that are not simple to fulfill. Starting with biocompatible packaging and ending with power consumption. Moreover, the integration of many sensors and actuators, as well as integrated circuits is desirable in order to obtain the complete system. Such a device may be implanted in a permanent way, monitor online our physiology and react if necessary what may be easily imagined on blood analyzers [8] example or diabetic when the insulin could be dosed when necessary at the right dose.

1.1.2 Pressure sensors in the MEMS family

About 18% of the MEMS sold in the world are various pressure sensors [2]. They are mostly applied in automotive, aeronautic and medical applications where small weight and dimensions are crucial. The advancement in microtechnologies allowed us to fabricate extremely small and sensitive sensors at low cost and thus, this branch of MEMS is still growing, offering cheaper and more reliable solutions. Moreover, if we call the TREAD (Transportation Recall Enhancement, Accountability and Documentation) act, all vehicles manufactured after 2007 in the United States of America have to be equipped with the tyre pressure monitoring unit. Having in mind that the U.S. vehicle market is the biggest in the world and such a regulations may affect soon the other countries, we may easily see the perspective for the pressure sensors market.

Basically, there are many different pressure transduction mechanism including two main ones: piezoresistive and capacitive but in fact, the main principle of the pressure sensing remains unchanged since few decades. The choice between two mechanisms is application driven and all advantages and drawbacks have to be considered in order to choose the one that suits best the project requirements. Even though, still the good design of such a device is not a trivial task. Mainly, because in order to fabricate the proper sensors we have to simulate their behavior in order to reduce cost of development and thus, time-to-market. If one wants then to apply the common approach of the “virtual prototyping”, models and simulation tool must take into account all phenomena that occurs in such a device and mainly three domains have to be considered: mechanical, electrical and thermal one. It leads us to the multidomain, coupled analysis which is often tedious. Thus, since few decades along with the development of functional materials and fabrication processes, the advancement in the design and simulation tools based on the Finite Element Method [9] or Compact Modeling [10] is also visible.

1.1.3 Project context

All works on modeling and optimization of the piezoresistive pressure sensor included in this thesis were conducted in the frame of the national project of the French National Agency for Scientific Research (ANR). The main goal of the project was to develop the micro pressure sensor for the intracranial pressure measurement. The medical aspect of the project is extremely important while the measurement of the intracranial pressure (ICP) is indicated in neuro-traumatology in cases of a serious cranial injury. The necessity of such a device may by confirmed by the fact that only in Europe, about 6000 pressure sensors are implanted each year for such a purpose. As such a project is definitely application driven, there are many partners involved including clinical consultants and the industry.

Despite some existing solutions that allow us to perform such a task, two main problems arise: wire based communication and the temporal drift. Existing solutions are based on the small sensor implanted into the human's head whereas data are transmitted via long wire to the measurement unit. The schematic view of such a system and a photo of the real system that is commercially available are shown below (Fig. 1.3).

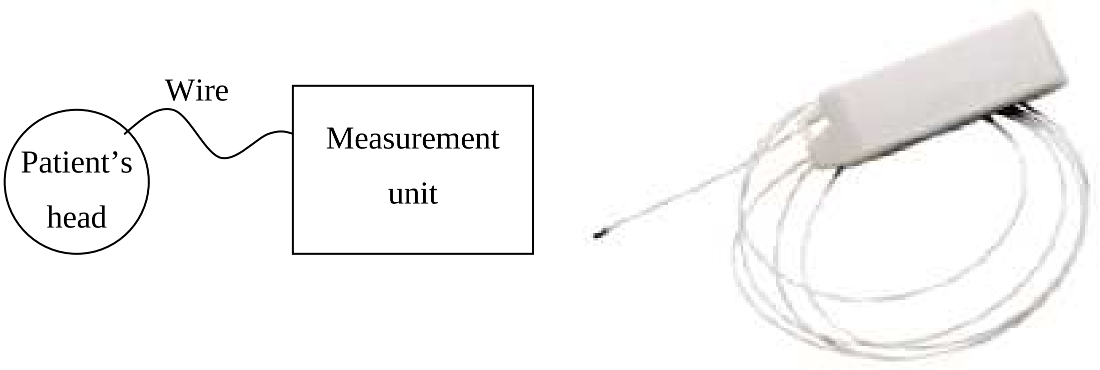

Fig. 1.3 The schematic view of the ICP measurement system and an example of the existing sensor (courtesy of CODMAN®).

As one may easily noticed, such a method is not very convenient for the patient as his ability to move freely is strongly reduced during the measurement. Additionally, if we consider the fact that in many cases such a procedure of ICP monitoring lasts a few weeks, we may easily imagine how difficult it can be for the patient.

The second, and even more important problem from the medical point of view, is the temporal drift. As the sensor operates in the “living” environment and once implanted have to stay in the human body till the end of monitoring period, it is affected by the different processes like the contact with proteins that may deposit on the membrane and, as a result, changes its mechanical properties and the output signal. As a solution, we added an auto-calibration feature that may overcome this problem by the in-vivo self-testing procedure. Such a feature is possible by adding the micromachined electrode under the sensor membrane what allows us to apply the voltage between them and generate the “electrostatic pressure”. Such a generated pressure will influence the sensor output signal and, as a result, allow to correct the sensor response.

Such an application, however, sets a lot of project constraints that have to be fulfilled. For example, if we want to transmit data via wireless communication protocol and thus increase the mobility level of the patient, the transceiver circuit must be an integral part of the sensor. As such a circuit needs a lot of power, the sensor itself should operate at power consumption level that is the lowest possible. In many cases, the capacitive transduction is envisaged as the sensor cell itself consumes a very little amount of power. Nevertheless, the circuit that converts the capacitance change into the frequency shift does. Moreover, as we plan to connect the sensor cell into the readout electronics via about 20 cm long cable, the parasitic capacitance may become a serious issue. Thus, the piezoresistive transduction mechanism was chosen as it does not need any complicated electronic circuits to convert the capacity change into the useful voltage signal even if the sensor itself will consume some steady state power used for the Wheatstone bridge supply what will be further elaborated.

Having in mind that the implanted device should be as less invasive as possible, it implicates that the lateral size of the membrane should be small. Moreover, addition of the second electrode under the membrane in order to use the auto-calibration feature limits the membrane vertical movement. Such a limit is due to the fact that the generated “electrostatic pressure”, which is a function of the distance, should be as high as possible in order to influence the output signal as much as possible.

To summarize, as we want to maximize the sensitivity of the sensor, we may not just increase it by simple decreasing of the membrane rigidity what is usually done but it has to be achieved by the proper choice of the strain gauge parameter. Moreover such a proper design of our sensor may decrease significantly other unwanted phenomena as temperature drift or generated noise.

It causes that the optimization phase is essential in order to deal with tradeoffs that have to be made in order to fulfill the project constraints and, at a time, obtain the best possible sensor performance. As a result of this work, the complete simulation tool based on analytical models that deals with all above mentioned problems is presented along with it advantages and drawbacks that come from some simplifications due to the analytical origin of the mechanical models. The electrostatic generator is a subject of a different work and will not be presented here. However, it has to be emphasized that all work that have been done and presented in this work take into account all project requirements that were mentioned above including the limits added by the built-in generator.

1.2 Thesis layout

This thesis is divided into three major blocks. At the beginning, the principles of piezoresistive pressure sensors design will be presented. All phenomena that occurs in such a device will be explained in details along with the theoretical background that is needed in order to understand the design logic. Additionally, the alternative method of simulation will be presented along with it advantages and drawbacks and an alternative method will be explained. It will be followed by the comparison between them in order to validate the proposed method.

The second part of this work will be dedicated to the design and optimization of the pressure sensor design in general. The proposed optimization method will be presented as well as the CAD tools that were created in order to help the designer in such a task. Moreover, the statistical approach will be presented as a simple solution that may be (under some conditions) useful in a simple preproduction yield analysis.

Last part of this work is focused on the fabrication of the sensor and its characterization. The complete technological process that was developed will be presented as well as the measurement setup that was used for the sensor characterization. Then, experimental results that confirm some simulation based results will be given. Additionally, the author’s own investigation concerning the experimental verification of the thermal coefficient of resistance for uniformly doped layers will be presented. Finally, the overall conclusion as well as the perspectives for the future work will be given.

2 Piezoresistive pressure sensor theory

In this chapter, an overview on the principle and modeling of MEMS piezoresistive pressure sensors will be presented. At the beginning, the basic mechanical transduction mechanism, which is the core of every pressure sensor, will be presented along with some theory and its mathematical description. That will be followed by the in-deep insight on the piezoresistive phenomenon in Silicon including the basic physical description, modeling approaches and experimental data published by now. Consequently, it will bring us to the section that will be sacrificed on the fabrication method and modeling of the implanted strain gauges which use the piezoresistive effect to the mechanical into electrical signal conversion. Moreover, the description of all fabrication related modeling issues such as: diffused layer modeling, process parameters identification as well as noise issues will be explained. Then, we will focus on the brief description of the Wheatstone bridge, the simple electronic readout circuit which is used in order to obtain a voltage signal at the output of the sensor, what will explain us the main advantages and drawbacks of such a transduction and will help us to understand why it is the most common type of the conversion.

As we presented in the previous chapter, there are some different approaches to modeling where the Finite Element Method is mainly used in the Microsystems design so at the end, some discussion about drawbacks of such an approach will be presented and, as an alternative, all previously mentioned facts will be combined in order to create a complete, piezoresistive pressure sensor analytical model which is the base of the created design and simulation tool.

2.1 Mechanical signal transduction

If we are talking about the pressure measurement, it would be highly desirable to know exactly what in fact is measured, so let us cite the basic definition as follows.

Pressure – the force per unit area applied to an object in the direction perpendicular to the surface. The basic unit in SI units system is Pascal (1 Pa = N/m^2)

In other words, the pressure is a mechanical value (force) that has to be measured. It has to be emphasized, that in micro scale sensors the amount of particles is enormous in comparison to sensor dimensions and they are in constant random motion in every direction what implies, that the pressure value do not depend on the position or the direction of the sensor in the measured medium. Such an assumption may fails only if we are working under conditions of the extremely low pressures were the number of molecules is very low.

2.1.1 Sensor layout – absolute and relative

As Einstein said "Everything is relative", so the pressure should also obey this well known rule, and it does. There are mainly three modes of pressure measurement that are in use: an absolute, a differential and a relative one (Fig. 2.1) which are somehow similar but the basic differences exist.

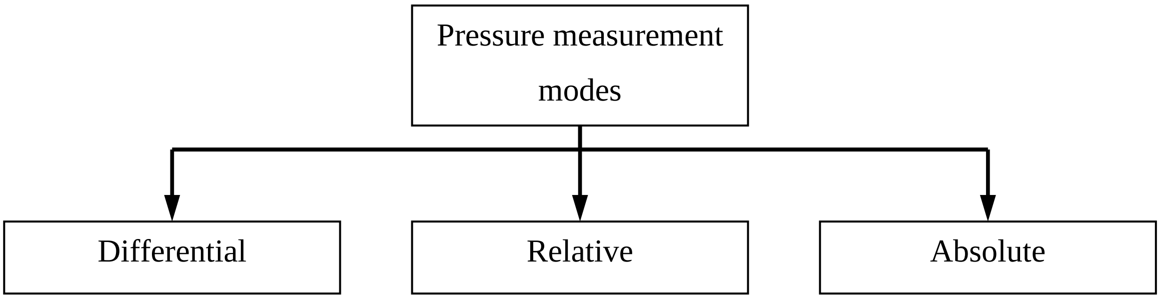

Fig. 2.1 Three basic modes of the pressure measurement.

In the differential mode, two different external pressures P_1 and P_2 are supplied to the sensor inputs and as a result, the signal which is proportional to the difference between them ($\Delta P=P_1-P_2$) is generated at the output.

The relative mode, however, needs only one input signal P_1 and instead of second pressure as in the previous case, the reference pressure P_{ref} is used to calculate the output signal. The P_{ref} is thus, an integrated part of the measurement system.

A special case of the relative mode, where the reference pressure is equal to the vacuum pressure is called an absolute mode which, for example, is widely use in the atmospheric pressure measurement.

As it was written in the first chapter, the main principle of micro pressure sensors remains unchanged since a few decades and actually, it is based on the conversion of the applied pressure into the mechanical movement of a membrane (Fig. 2.2).

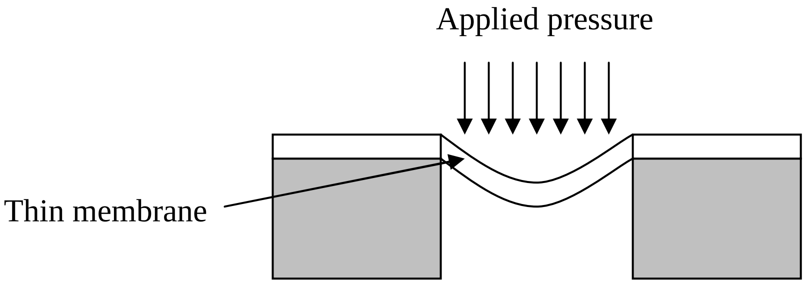

Fig. 2.2 The basic principle of the micromachined pressure sensor.

Because, as we said, there are three basic modes of the pressure measurement, the sensor layout for each mode should be different what is presented in Fig. 2.3.

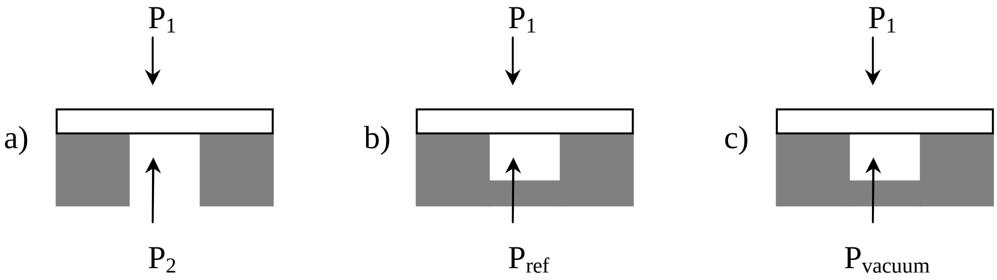

Fig. 2.3 Exemplary sensor layouts for differential a), relative b) and absolute c) pressure measurement.

Considering any type of the pressure sensor, the most important part of it is its membrane, and thus, in order to fully understand the conversion mechanism we need to know the mechanics that rules the behavior of it.

2.1.2 Membrane mechanical behavior

When some solid material has no mechanical load applied on it, all atoms in within it are arranged in a way where the potential energy of a system is minimal - a stable equilibrium state (Fig. 2.4 a). If we, however, apply some load onto it, it will try to rearrange the atomic structure. Considering, for example, a tensile loading we will observe the relative elongation $\Delta l/l$ of the solid which is called the strain ε. It may be considered as a result of a force that will be applied on each atom in a structure what, according to the third law of Newtonian dynamics, will cause a reaction forces that will appear between atoms (Fig. 2.4 b).

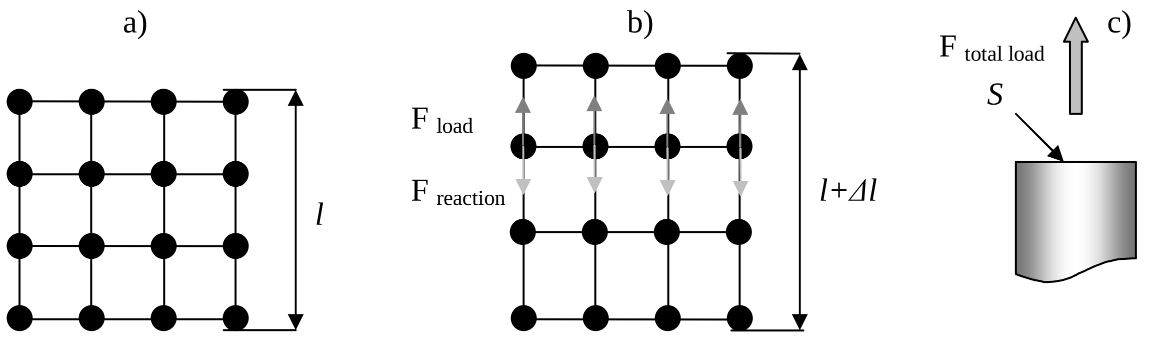

Fig. 2.4 A two-dimensional view of the crystal lattice and the corresponding macroscopic representation of a solid material under tensile loading.

Such a reaction force exerted per unit area is called the stress σ. The macroscopic applied force $F_{total\ load}$, is an integral of the stress over the sample surface S (2.1).

$$F_{totalload} = \int_S \sigma dS \tag{2.1}$$

Stress and strain values are related by the known relation, called the Hook's law (1678) (2.2). The coefficient of relation is called the Young's modulus E and, as we can see, the relation is linear.

$$\sigma = E \cdot \varepsilon \tag{2.2}$$

where

$$\sigma = \frac{F}{S} \text{ and } \varepsilon = \frac{\Delta l}{l}$$

The reason why the linearity occurs is that we consider that all strains (tensile or compressive) caused by the external load are **small** (about few %) and thus, we consider that the potential energy of atoms in a function of their relative distance obeys the quadratic law as it is depicted in Fig. 2.5.

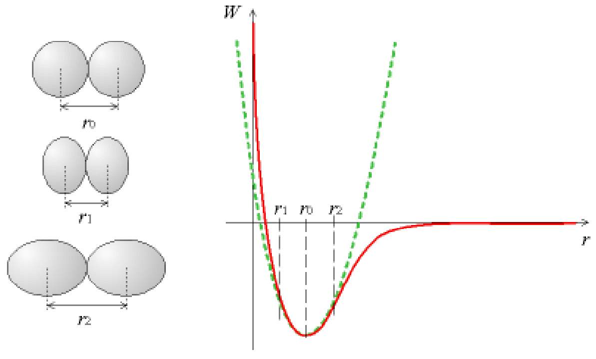

Fig. 2.5 The potential energy *W* of two atoms as a function of the relative distance between them *r*. r_0 is the equilibrium distance, r_1 and r_2 are effects of compressive and tensile loading respectively [11].

If we consider the potential energy W in the neighborhood of the equilibrium distance r_0, we may express it as follows (2.3).

$$W(r) = w_0 + k(r - r_0)^2 \tag{2.3}$$

As we know, the force is the first derivative of the energy over the distance so it leads us to the relation (2.4).

$$F = \frac{\partial W(r)}{\partial r} = 2k(r - r_0) \tag{2.4}$$

It proves that the force has to be the linear function of the relative elongation if we are working in the small deformation regime and it has to be emphasized that all mechanical calculations which are used in following chapters obey this rule.

Timoshenko's model

Until now, we used the word membrane to describe the thin diaphragm which is used in the mechanical signal conversion but at this moment, in order to avoid confusion, we have to precise our language according to the mechanical nomenclature. In general, we can distinguish three basic theories concerning the diaphragms:

- Thick plate theory
- Thin plate theory
- Membranes theory

The factor that distinguishes between these three approaches is the length a to height h ratio [12] what is provided in Fig. 2.6.

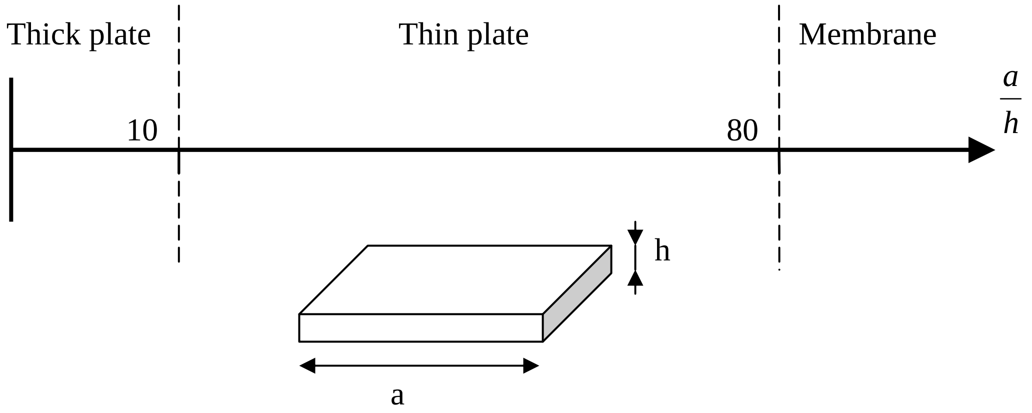

Fig. 2.6 Distinguishing limits that separate thick plate, thin plate and the membrane.

The problem of the analytical description of such a system is not new and throughout the years, many outstanding scientists such as: Euler (1766) [13], Bernoulli (1789) [14] or Kirchhoff (1850) [15], to name but a few, have worked on it. It has to be noticed that in almost all pressure sensors, thin plates and membranes are used (length to height ratio over 10) and the simple explanation for it is that thick plates provide us with the sensitivity which is not enough what will be explained later. Because the membrane theory is a simplification of a thin plates theory, in further investigations we will always consider that the sensing part of a sensor as a thin plate but for the reason of daily language we will call it the membrane.

Among many theories that have been worked out like the Lagrange equation (1828) [16], which was corrected by Poisson (1829) [17], one of the most important is the Kirchhoff's plate theory which was describe in his thesis (1850). After that, as a continuation and development of Kirchhoff's theory, the outstanding work was presented by Timoshenko (1913) [18], but just some decades later in 1959 together with Woinowsky-Krieger a textbook [19] that is fundamental in the plate bending analysis was published. Thus, all analyses that will be performed in next sections are based on that work.

Basically, the out-of-plane deformation of a membrane, which has an uniform thickness and is perfectly clamped, in the steady state is governed by the Lagrange equation (2.5) which allows us to calculate the out-of-plane membrane deflection *w(x,y)* as a function of Cartesian coordinates *(x,y)*.

$$\frac{\partial^4 w(x,y)}{\partial x^4} + 2\alpha \frac{\partial^4 w(x,y)}{\partial x^2 \partial y^2} + \frac{\partial^4 w(x,y)}{\partial y^4} = \frac{P}{D \cdot h^3} \tag{2.5}$$

P represents the differential pressure applied on the membrane; h is its thickness; D is a rigidity parameter which depends on material properties whereas α is an anisotropy coefficient which depends on the crystallographic orientation.

Material properties

It is a good moment to say some words about the material which the sensor is made of before we proceed to the solution of the equation (2.5). The knowledge about the silicon has advanced dramatically since it became the core of the microelectronics industry and thus, we can easily say that it is one of the most known materials in the world which was characterized in almost all possible ways for the needs of new devices with outstanding performances. The main reasons [20] why silicon is so popular also in Microsystems are:

- High Young modulus (comparable to the steel) while the weight is close to the aluminum
- Melting point at about 1400ºC what causes that it may be processed at high temperatures
- Low coefficient of thermal expansion
- No mechanical hysteresis, silicon remains elastic in a very wide range of loads.

The monocrystalline silicon is a part of the IV group of the periodic table and its lattice is considered to be face-centered diamond cubic structure with the lattice constant *b* of 5.43Å [21] (Fig. 2.7). Thus, its properties are moderately anisotropic, what makes the mathematical description much more complex and the crystal orientation has to be taken into account in any mechanical calculations.

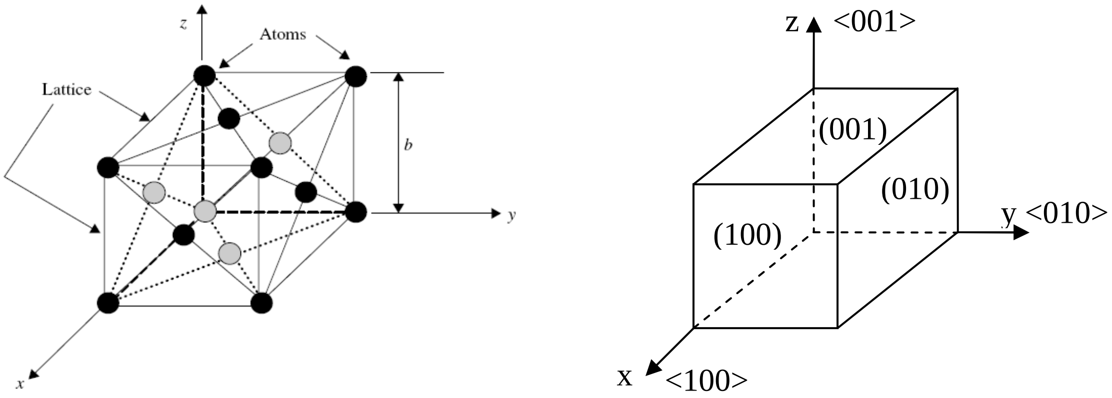

Fig. 2.7 The model of the crystal lattice of silicon [21] and corresponding crystallographic directions expressed as Miller indices.

Normally, each element of a cubic shape crystal lattice under mechanical loading will be exposed to normal and shear stresses as it is shown in a Fig. 2.8.

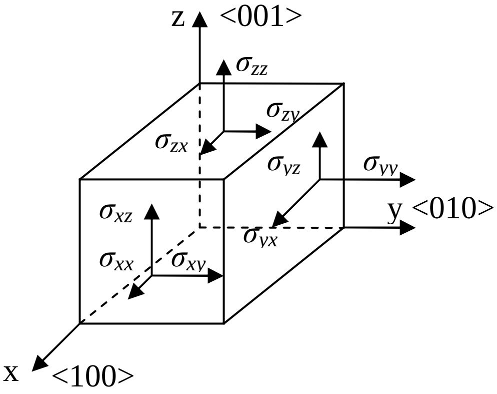

Fig. 2.8 Stress components in a small cubic element of the material.

Thus, the stress in a small volume of such a material has to be expressed as a tensor with nine independent elements what implies that the generalized Hooke's law (2.2) for anisotropic coefficients has to be rewritten, in more general form (2.6).

$$\boldsymbol{\sigma} = C\boldsymbol{\varepsilon} \tag{2.6}$$

Stress vector $\boldsymbol{\sigma}$ consists of nine independent stress components (Fig. 2.8) and strain vector $\boldsymbol{\varepsilon}$ contains nine corresponding strain components while C is called the stiffness matrix and is described by eighty-one coefficients.

If we, however, consider that the material is in the state of equilibrium, what causes that there is no torsional movement, some of the stress components will have the same value ($\sigma_{xy}= \sigma_{yx}$; $\sigma_{zy}= \sigma_{yz}$; $\sigma_{xz}= \sigma_{zx}$) and thus, the stress and strain vector may be reduced to only six components.

There is, however, another feature of the silicon that makes all the calculation much easier. Fortunately, because of the diamond-like structure, the orthogonal directions have the same mechanical properties [22] what causes that the tensor of elasticity, which is used to fully describe the stress-strain relation in silicon crystal, which now can be considered as an orthotropic material, has only three different nonzero valued coefficients. Generally, after all simplifications and applying the following convention of indexing (2.7), the stress-strain relation for crystalline silicon, instead of its basic form (2.2) in case of isotropic materials, may be provided by the following equation (2.8) if we consider that the wafer is cut along the (100) plane what is usually done.

$$\begin{aligned} xx &\rightarrow 1 \\ yy &\rightarrow 2 \\ zz &\rightarrow 3 \\ yz &\rightarrow 4 \\ xz &\rightarrow 5 \\ xy &\rightarrow 6 \end{aligned} \tag{2.7}$$

$$\begin{bmatrix} \varepsilon_1 \\ \varepsilon_2 \\ \varepsilon_3 \\ \varepsilon_4 \\ \varepsilon_5 \\ \varepsilon_6 \end{bmatrix} = \begin{bmatrix} \frac{1}{E} & \frac{-v}{E} & \frac{-v}{E} & 0 & 0 & 0 \\ \frac{-v}{E} & \frac{1}{E} & \frac{-v}{E} & 0 & 0 & 0 \\ \frac{-v}{E} & \frac{-v}{E} & \frac{1}{E} & 0 & 0 & 0 \\ 0 & 0 & 0 & \frac{1}{G} & 0 & 0 \\ 0 & 0 & 0 & 0 & \frac{1}{G} & 0 \\ 0 & 0 & 0 & 0 & 0 & \frac{1}{G} \end{bmatrix} \cdot \begin{bmatrix} \sigma_1 \\ \sigma_2 \\ \sigma_3 \\ \sigma_4 \\ \sigma_5 \\ \sigma_6 \end{bmatrix} \tag{2.8}$$

The *E* symbol represents the Young's modulus whereas *v* corresponds to the Poisson's ratio. The factor *G* in (2.8) is called the shear modulus or Coulomb modulus and it describes the reaction of the material to the shear stress. The anisotropy coefficient α that appeared in (2.5) is then easily calculated using (2.9) and (2.10).

$$G = \frac{E}{2(1+\nu)} \tag{2.9}$$

$$\alpha = \nu + \frac{2G(1-\nu^2)}{E} \tag{2.10}$$

Nevertheless we have to be conscious about different values of the basic parameters depending on the crystallographic directions. In table 2.1, the basic mechanical parameters of Silicon are presented for the most popular directions <100> and <110> [23].

Table 2.1 Mechanical parameters of silicon in a function of crystallographic direction [23].

Direction	Young modulus [GPa]	Shear modulus [GPa]	Poisson coefficient	Anisotropy coefficient
<100>	129.8	79.5	0.278	1.4067
<110>	168.9	50.4	0.0625	0.6621

As we can easily notice, differences are remarkable and they are essential to perform a proper analysis of our system, especially if we consider the piezoresistivity phenomenon what will be shown later in this work.

Solution of the mechanical system

Let us go back to the equation (2.5) that governs the steady state mechanical behavior of the membrane under the uniform loading. To start with, in order to interpret results correctly, we have to define the Cartesian coordination system by setting its origin (*0,0*) in the center of our plate. The *XY* plane is then considered to be parallel to the membrane plane where *a* and *b* represent the plate lateral dimensions (Fig. 2.9).

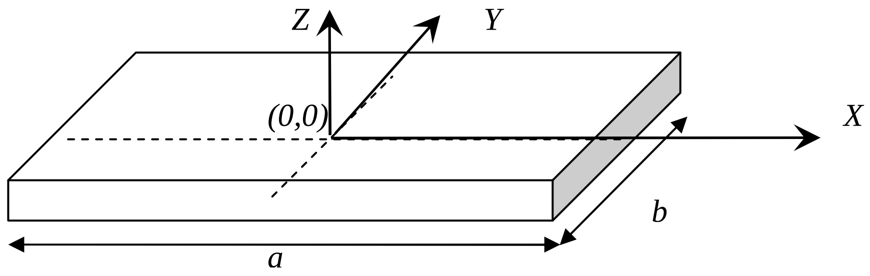

Fig. 2.9 Cartesian coordination system that is used for computing of the membrane mechanical behavior.

As it is the differential equation, in order to solve it, a set of boundary conditions has to be defined. In our case the assumption about the perfectly clamping is enough to formulate them as follows (2.11).

$$w\left(\pm\frac{a}{2},y\right)=0\,;\;w\left(\pm\frac{b}{2},x\right)=0 \qquad \text{and} \qquad \frac{\partial w\left(\pm\frac{a}{2},y\right)}{\partial x}=0\,;\;\frac{\partial w\left(\pm\frac{b}{2},x\right)}{\partial y}=0 \tag{2.11}$$

As we can remark, the model supports only the simplest shapes of the membrane like square and the rectangular one, what in real applications is rather enough. The circular shapes are also supported but for the reason of easier calculations, the coordinates system has to be changed into the polar one. During the next few pages we will try to present the solution of (2.5) for each of the basic shape and finally we will say some words about the stress distribution in the deformed plate.

Rectangular and square membranes

The exact solution of (2.5) does not exist and thus, some approaches [24, 25, 26] were presented in order to approximate it. The most popular is the polynomial approximation [27] where the general formula that provides us with the membrane deformation $w(x,y)$ as a function of coordinates is given by a series (2.12). It is valid for rectangular shape and a special case of it, a square one.

$$w(x,y)=w_0\left(1-\left(\frac{2x}{a}\right)^2\right)^2\left(1-\left(\frac{2y}{b}\right)^2\right)^2\left[\sum_{i=0}^{n}\sum_{j=0}^{n}k_{ij}\left(\frac{2x}{a}\right)^i\left(\frac{2y}{b}\right)^j\right] \tag{2.12}$$

$$w_0=c\,\frac{Pa^2b^2\left(1-v^2\right)}{16Eh^3}$$

The correction coefficient c in a formula which describes the maximal deflection value w_0, is dependent on the membrane shape (more precisely on a/b ratio) whereas k_{ij} is the matrix of coefficients. Both values are calculated using the potential energy minimization method proposed by Galerkin [28]. For typical, a/b ratios (ranging from 1 to about 4), the series (2.12) is enough approximation if we limit its order n to 3 [29]. Thus, the matrix k_{ij} consists of nine values. Precise calculations of these coefficients are quite tedious and they are presented in details in the literature [30], so here we limit ourselves to provide calculated values for typical a/b ratios (tables 2.2 and 2.3).

Table 2.2 Correction coefficient *c* for the maximal deflection value in a function of the membrane shape.

a/b ratio	1	2	3
c coefficient	0.0164	0.0314	0.0319

Table 2.3 k_{ij} matrix coefficients computed by using the Galerkin method [29].

a/b ratio	1	2	3
k_{00}	1	1	1
k_{02}	0.214	1.3025	1.9056
k_{20}	0.214	0.0134	0.005
k_{22}	0.2748	0.166	-0.2237
k_{24}	0.9801e-1	0.6994	1.5084
k_{42}	0.9801e-1	-0.0205	-0.0232
k_{40}	-0.6227e-2	-0.0013	0.004
k_{04}	-0.6227e-2	0.4133	3.0122
k_{44}	-0.1035	0.0801	0.0506

Circular membrane

The things look a little bit different if one wants to consider the isotropic circular membrane which is characterized by its radius *R*. Such a system is characterized by the axial symmetry (Fig. 2.10), so in order to simplify calculations, the out-of-plane deformation *w(r)* is considered to be dependent only on the distance form its center *r* (2.13).

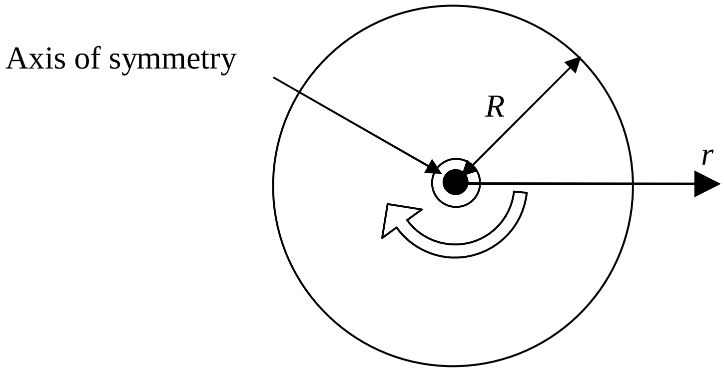

Fig. 2.10 Axial symmetry of the circular membrane.

$$w(r) = w_0\left(1-\frac{r^2}{R^2}\right)^2; w_0 = \frac{12P\left(1-\nu^2\right)R^4}{64Eh^3} \tag{2.13}$$

At this moment, one can ask a question: what about the anisotropy? The answer is that the anisotropy, in case of circular membranes, is taken into account only in the maximal deformation calculations [31] and the form of the membrane is not considered to be orientation dependent.

Stress distribution

Having computed the membrane deflection, for our application, the more important thing that has to be calculated is the stress distribution over the membrane surface. According to the Hooke's law, for rectangular membrane the in-plane (*XY*) stress value as a function of the position on the membrane surface (*x*,*y*) may be expressed by using formulas (2.14) and (2.15).

$$\sigma_X(x,y) = \frac{h \cdot E}{2 \cdot (1-\nu^2)} \left(\frac{\partial^2 w(x,y)}{\partial x^2} + \nu \frac{\partial^2 w(x,y)}{\partial y^2} \right) \tag{2.14}$$

$$\sigma_Y(x,y) = \frac{h \cdot E}{2 \cdot (1-\nu^2)} \left(\frac{\partial^2 w(x,y)}{\partial y^2} + \nu \frac{\partial^2 w(x,y)}{\partial x^2} \right) \tag{2.15}$$

Whereas for the circular membrane the only radius dependent formula is given by (2.16).

$$\sigma(r) = -\frac{E \cdot z}{\left(1-\nu^2\right)} \frac{\partial^2 w(r)}{\partial r^2} \tag{2.16}$$

As we can see, the stress values are independent of the Z-axis. The reason of that is the assumption about the thin plate where the thickness of the plate does not influence the stress distribution at its surface. In the reality, the bended plate with finite thickness will be exposed to tensile stresses at on side and to compressive ones at the opposite side (Fig. 2.11 b). Thus, according to the theory of plates and shells [19], the stress value changes linearly form its maximal value σ_{max} to - σ_{max} along the membrane thickness, reaching the zero value at the midpoint (Fig. 2.11 c).

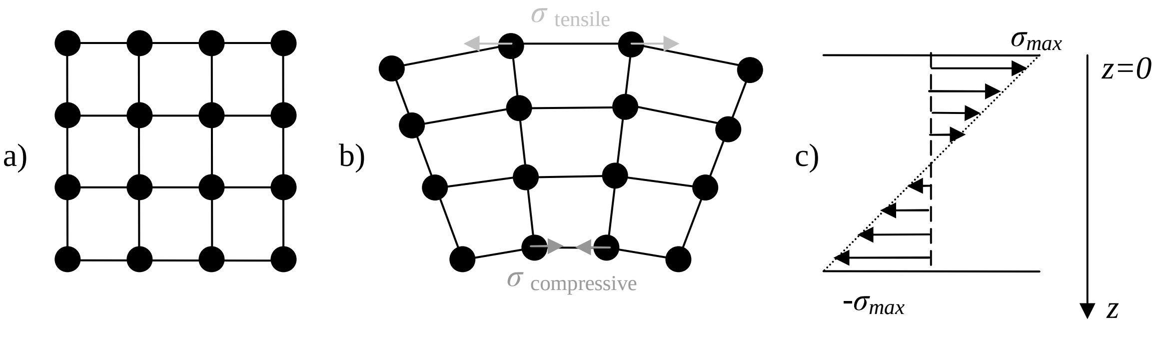

Fig. 2.11 The simplified model of the unloaded structure a), bended structure with compressive and tensile stresses b), model of stress distribution along the membrane thickness c).

In other words, the stress value *σ(z)* at any point inside the membrane, for given (*x,y*) coordinates, may be calculated with help of the following formula (2.17). The maximal stress value σ_{max} is calculated by using formulas (2.14) and (2.15).

$$\sigma(z) = \sigma_{max}\left(-\frac{2}{h}z + 1\right) \tag{2.17}$$

where *h* is the plate thickness.

As we may notice, the mechanical behavior of a thin plate under uniform loading is rather known problem that is well described in a literature. Presented model has one strong limitation which is the perfectly clamping assumption and consequences of that will be explained later. Nevertheless, we put some light on the first stage of our sensor where pressure conversion into mechanical response (stress) occurs and now we may proceed to the second stage where the mechanical value will be converted into response in the electrical domain.

2.2 Phenomenon of the piezoresistivity

2.2.1 Theory

The piezoresistivity phenomenon is not at all a new discovery. If we look back to the history in 1856 Sir Thompson (Lord Kelvin), remarked that the resistance value of metallic bars changes when they are exposed to the mechanical loading. Let us look more carefully at this phenomenon.

Basics

To start with, let us consider the bar of the unknown material with the spatial dimensions of *L*, *w* and *t* as it is shown in Fig. 2.12.

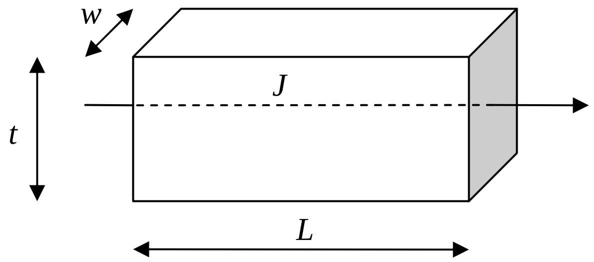

Fig. 2.12 The bar of material under electrical loading.

If we force a current flow *J*, that passes along its length *L*, through it, we are able to compute its electrical resistance *R* by using the definition (2.18).

$$R = \rho \frac{L}{wt} \tag{2.18}$$

The coefficient ρ is called the resistivity and it is one of the material properties. As one can see, in order to change the electrical resistance, one may perform following actions: change dimension or change the resistivity. What Lord Kelvin did, was the observation of resistance variation of the metallic bars under tensile loading that changes the lateral dimension of the sample (Fig. 2.13).

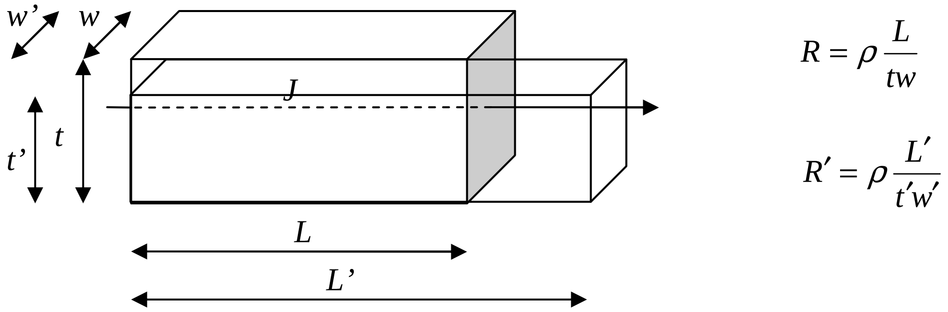

Fig. 2.13 The simplified Lord's Kelvin experiment.

Such a behavior was called the piezoresistance effect. Because, such a kind of transducer transforms mechanical value (strain) into the electrical one (resistance) it is called a strain gauge. In order to compare different gauges or, let us say, different materials, the dimensionless coefficient called the gauge factor was introduced. The gauge factor *K* is defined as a relative change of resistance to the applied strain ratio (2.19).

$$K = \frac{\Delta R / R}{\Delta L / L} \tag{2.19}$$

One of the pioneers that started to use the metallic strain gauges in metrology was Bridgman in 1932 [32]. He experimented with different materials and he has been looking for the one with the highest gauge factor. Unfortunately, in case of metals or their alloys, gauge factors are relatively weak (2 to 4) and thus, the useful output signal is hard to detect. In fact for the metallic strain gauges, the piezoresistive effect appears mostly due to the dimension changes not to the change in the resistivity parameter. It was reported by Bridgman as the following relation (2.20).

$$\frac{\Delta \rho}{\rho} = C \frac{\Delta V}{V} \tag{2.20}$$

The *C* is called the Bridgeman constant whereas *V* is the volume of the sample.

Smith's discovery

The real milestone in the history was the discovery of the piezoresistive effect in silicon by Smith in 1954 [33]. Silicon in the fifties was very promising material since microelectronics technology has became more and more mature those days and thus, a lot of work has been done in order to characterize it. Smith presented the results of studies on both N and P type silicon and Germanium samples and estimated piezoresistive coefficients. Amazingly, those first results showed that the estimated possible gauge factors are about 30 times higher comparing to those that were achieved in metallic gauges. It is caused by the fact, that in silicon, the resistance change is caused mainly by the resistivity then dimensions variation. Thus, it is called the piezoresistive effect. It showed that silicon is the material that not only may be used as a semiconductor to produce new electronic devices such as transistors, but it also offers excellent sensing possibilities.

Three years later (1957), Mason and Thurston [34] presented the result of study on possible application of the piezoresistive effect in silicon based force sensors; it took a four years when in 1961 Pfann and Thurston [35] presented the first working device.

Another important date was the year 1963 when Tufte and Stelzer [36], followed by Kerr and Milnes [37] published their studies on dependence of the piezoresistance coefficient on temperature, doping level and the crystallographic orientation.

2.2.2 Modeling

Let us consider again, the bar of material under tensile loading (Fig. 2.13). As we know from the previous part of this chapter, each element of the cubic shape crystal will be exposed to normal and shear stresses (Fig. 2.8). It was mentioned that there are two components that may change the electrical resistance value: resistivity and geometrical dimensions. Unlike in metallic bars, in silicon the variation of resistance is in 99% due to the resistivity change than the geometry change and thus, for all calculations we will neglect the second source of the piezoresistive effect. Assuming additionally **small stresses** and thus, small deformations of the crystal lattice, if we consider the isotropic material, the piezoresistance effect may be expressed by the equation 2.21, where ρ is the resistivity, ρ_0 is the resistivity value for unstressed sample, σ is an induced stress value and π is called the piezoresistance coefficient.

$$\rho = \rho_0 + \rho_0 \pi \sigma \tag{2.21}$$

Introducing a more general approach for the anisotropic diamond-like structure of silicon, we may apply analogous description as it was used in case of the mechanical behavior. Let us then to formulate an Ohms law (2.22) for the three dimensional, cubic element of the Silicon (Fig. 2.13) which is exposed to the vector ***E*** of the electrical field that stimulates the current flow defined as a vector ***J***.

$$\begin{bmatrix} E_x \\ E_y \\ E_z \end{bmatrix} = \begin{bmatrix} \rho_{xx} & \rho_{xy} & \rho_{xz} \\ \rho_{yx} & \rho_{yy} & \rho_{yz} \\ \rho_{zx} & \rho_{zy} & \rho_{zz} \end{bmatrix} \cdot \begin{bmatrix} J_x \\ J_y \\ J_z \end{bmatrix} \tag{2.22}$$

In case of the silicon structure there is again some symmetry that may reduce the piezoresistivity tensor to the six elements. Moreover, for unstressed silicon, only the diagonal elements of the sensor (ρ_{xx}, ρ_{yy}, ρ_{zz}) will have the nonzero values and will have an equal value ρ, so if we apply again the conversion (2.7), the tensor $\boldsymbol{\rho}$ may be rewritten as follows (2.23).

$$\boldsymbol{\rho} = \begin{bmatrix} \rho_1 & 0 & 0 \\ 0 & \rho_2 & 0 \\ 0 & 0 & \rho_3 \end{bmatrix} = \begin{bmatrix} \rho & 0 & 0 \\ 0 & \rho & 0 \\ 0 & 0 & \rho \end{bmatrix} \tag{2.23}$$

Finally, it lead us to the final form of the equation that describes the relation between the stress and resistivity for anisotropic silicon crystal (2.24).

$$\begin{bmatrix} \rho_1 \\ \rho_2 \\ \rho_3 \\ \rho_4 \\ \rho_5 \\ \rho_6 \end{bmatrix} = \begin{bmatrix} \rho_1^0 \\ \rho_2^0 \\ \rho_3^0 \\ 0 \\ 0 \\ 0 \end{bmatrix} + \begin{bmatrix} \rho_1^0 \\ \rho_2^0 \\ \rho_3^0 \\ 0 \\ 0 \\ 0 \end{bmatrix} \cdot \begin{bmatrix} \pi_{11} & \pi_{12} & \pi_{12} & 0 & 0 & 0 \\ \pi_{12} & \pi_{11} & \pi_{12} & 0 & 0 & 0 \\ \pi_{12} & \pi_{12} & \pi_{11} & 0 & 0 & 0 \\ 0 & 0 & 0 & \pi_{44} & 0 & 0 \\ 0 & 0 & 0 & 0 & \pi_{44} & 0 \\ 0 & 0 & 0 & 0 & 0 & \pi_{44} \end{bmatrix} \cdot \begin{bmatrix} \sigma_1 \\ \sigma_2 \\ \sigma_3 \\ \sigma_4 \\ \sigma_5 \\ \sigma_6 \end{bmatrix} \tag{2.24}$$

Three coefficients π_{11}, π_{12} and π_{44} describe completely the piezoresistive behavior of the anisotropic material with diamond-like crystal lattice. Their values were experimentally estimated by Smith for the low doped silicon, both N and P type (Table 2.4).

Table 2.4 Piezocoefficients values obtained by Smith for low doped silicon [33].

Piezocoefficient	π_{11} [10^{-11} Pa^{-1}]	π_{12} [10^{-11} Pa^{-1}]	π_{44} [10^{-11} Pa^{-1}]
P-type	+6.6	-1.1	+138.1
N-type	-102.2	+53.4	-13.6

Kanda's model

Euler's angles

It has to be emphasized that all above cited formulas are valid for the crystal orientation that was presented on Fig. 2.7 and Fig. 2.8, so the stress component σ_{xx} is parallel to the <100> direction. The basic relation (2.21) for the bar of material (Fig. 2.13) should now be written for more general case when the direction of our sample is freely chosen. Such calculations were presented by Kanda [38], what is commonly presented as (2.25).

$$\frac{\Delta\rho}{\rho} = \pi_l\sigma_l + \pi_t\sigma_t \tag{2.25}$$

Where pairs π_l and π_t are called longitudinal and transversal piezoresistance coefficients whereas σ_l and σ_t are respectively longitudinal and transversal stress components. The factor $\Delta\rho/\rho$ is a relative resistivity change. As a longitudinal, we understand the direction that is parallel to the current flow in the bar. Such a convention force us to find the way of translation of the description (2.25) to be used for any direction of the current flow in the crystal.

Such a translation is made by using the transformation based on Euler's angles because every rotation (around all three axes) of any Cartesian coordination system may be described by using three angles values what is shown below (Fig. 2.14).

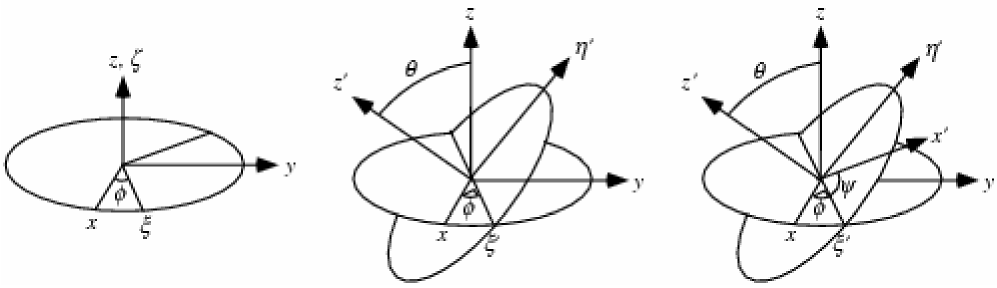

Fig. 2.14 Transformation of Cartesian coordination system defined by Euler angles.

In order to perform the translation, the transformation matrix *R* has to be defined as follows. (2.26).

$$R = \begin{bmatrix} l_1 & m_1 & n_1 \\ l_2 & m_2 & n_2 \\ l_3 & m_3 & n_3 \end{bmatrix} \tag{2.26}$$

The transformation between two coordination system XYZ into X'Y'Z' is then given by (2.27).

$$\begin{bmatrix} x \\ y \\ z \end{bmatrix} = R \cdot \begin{bmatrix} x' \\ y' \\ z' \end{bmatrix} \tag{2.27}$$

The transformation is performed in three steps. In the beginning, axes are rotated along *Z* axis with the rotation angle of φ and then the rotation along the *X* axis with an angle of θ occurs. At the end, the third rotation **again** along the *Z* axis is done with the angle of ψ. In such a case, the matrix *R* is expressed by (2.28).

$$R = \begin{bmatrix} \cos\varphi\cos\psi - \sin\varphi\cos\theta\sin\psi & \cos\varphi\sin\psi + \sin\varphi\cos\theta\cos\psi & \sin\varphi\sin\theta \\ -\cos\varphi\cos\psi - \cos\varphi\cos\theta\sin\psi & -\sin\varphi\sin\psi + \cos\varphi\cos\theta\cos\psi & \cos\varphi\sin\theta \\ \sin\theta\sin\psi & -\sin\theta\cos\psi & \cos\theta \end{bmatrix} \tag{2.28}$$

By using this matrix, we are able to calculate the longitudinal and transversal coefficient of piezoresistance if we know the rotational angles that indicate the direction of the current flow relatively to the <100> direction.

As an example, the longitudinal coefficient of piezoresistance in P-type silicon will be traced as a function of the crystallographical direction for (100) plane (Fig. 2.15).

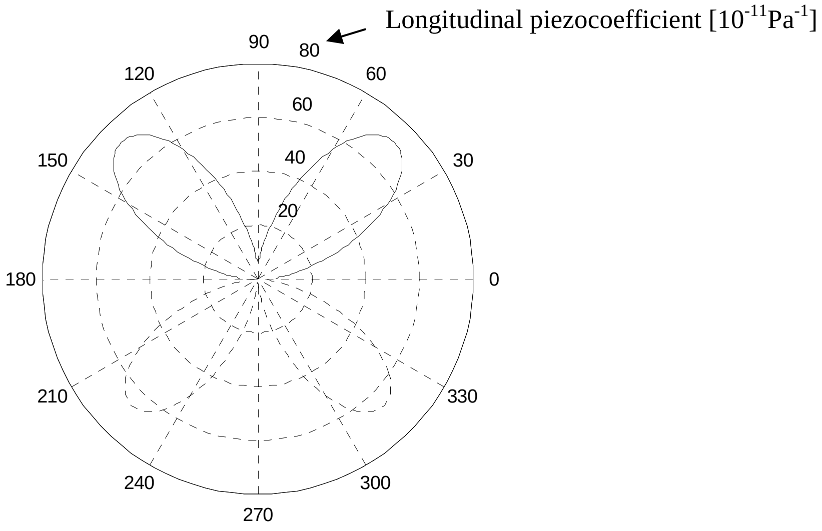

Fig. 2.15 The longitudinal coefficient of piezoresistance plotted for P-type silicon in (100) plane.

As we may notice, the highest value is reached for <110> direction what is used in practical applications during the transducer design stage.

The physical source of the piezoresistive effect is a shift of the material bandgap due to the applied stress. Such a bandgap modification causes that the effective mass of holes and electrons changes and thus, carriers mobility is affected what influences the resistivity. Although such an approach is rather known, the exact model of piezoresistance effect does not exist. Moreover, the piezoresistance description differs for N and P type silicon and thus, some relevant works for both type of conductivity were performed separately.

The piezoresistance in P type silicon has been thoroughly studied by Suzuki [39] and Kleimann [40] but they both considered that almost all holes are located at wave vector $k = 0$ what is true but only for very small hole energies (very low temperatures in range of a few K). Thus, their model could not be considered for normal operating temperatures. Ohmura [41] developed the model that took into account that for room temperature, holes are usually located off $k = 0$ what was presented by Pikus and Bir [42].

Another attempt was the model developed by Kim [43] which takes into account also spin-orbit split off band. His results were used by Lenkkeri [44] which studied the piezoresistance at a room temperature.

One of the work that thoroughly describes the piezoresistance is the work of Toriyama and Sugiyama [45] where they used the model of Pikus and Bir and traced the piezocoefficient as a function of doping and temperature for P-type silicon.

Kanda, however earlier in his work [38], presented the model that enables us to calculate the piezocoefficients as a function of doping level and temperature for both N and P type silicon in a relatively simple manner and correlated it to the experimental values so for further calculation such a model will be used because of above mentioned capabilities.

Temperature and doping level dependency

The basic conclusion of Kanda's work is that the piezoresistance coefficient obeys the following relation (2.29).

$$\pi(N,T) = \pi(N_0, 300K) \cdot P(N,T) \tag{2.29}$$

The coefficient $\pi(N_0, 300K)$ stands for piezocoefficient value for the low-doped silicon as depicted in a Table 2.4, N is a doping level value and T is an absolute temperature value. $P(N,T)$ is a correction function that depends on temperature and doping level and is given by the formula (2.30).

$$P(N,T) = \frac{300}{T} \frac{F'_{s+\frac{1}{2}}\left(\frac{E_f}{k_b T}\right)}{F_{s+\frac{1}{2}}\left(\frac{E_f}{k_b T}\right)} \tag{2.30}$$

where

$$F_{s+\frac{1}{2}}\left(\frac{E_f}{k_bT}\right)=\int_0^{\infty}\frac{E^{s+\frac{1}{2}}}{1+\exp\left(E-\frac{E_f}{k_bT}\right)}dE \tag{2.31}$$

Formula (2.31) is called the Fermi integral [46] where E_f represents the Fermi energy in doped silicon and k_b is the Boltzmann's constant. The s value is called the scattering component and according to [47] is equal to -1/2 if we consider the lattice scattering mechanism. Although, such an approach gives a good results for N type silicon, it is also used for P type one.

The Fermi energy is dependent on doping level and thus, the relation between them is expressed by (2.32).

$$N=v\frac{\sqrt{2}}{\pi^2}\cdot\left(\frac{m_dk_bT}{h}\right)^{\frac{3}{2}}\cdot F_{\frac{1}{2}}\left(\frac{E_f}{k_bT}\right) \tag{2.32}$$

Parameter v is a number of energy valleys and for silicon is equal to 6, h is a Planck constant and m_d is the density-of-state effective mass of carriers which values published by Smith [48] are presented below (Table 2.5).

Table 2.5 Density-of-state effective masses of carriers for both N and P type silicon [48].

Silicon	N type	P type
m_d	0.33	0.55

The most difficult problem with the calculation of the term $P(N,T)$ by using equations (2.30-2.32) in a function of doping level N is the inversion of the Fermi integral of order +1/2 (2.31). In fact, the Fermi integral is noninvertable and thus, it is not analytically possible so we are forced to use an approximate solution. In the literature, one can find many different solutions like the simplest Boltzman or Joyce-Dixon [49] approximations as well as more complicated solutions such as Nilson [50] approximations. As a result, the procedure of calculations is not straightforward and it will be presented now. To start with, let us define two dimensionless variables η_f and ξ as follows (2.33).

$$\eta_f=\frac{E_f}{k_bT}\qquad \xi=\frac{N}{N_s} \tag{2.33}$$

where N is the current doping level in a semiconductor and N_s corresponds to the effective density of states in the conduction band which for the P type silicon is given by (2.34).

$$N_s=\frac{\sqrt{\pi}}{2}\cdot 2.5e+19\cdot\left(\frac{0.59}{300}T\right)^{\frac{3}{2}} \tag{2.34}$$

The Fermi integral of order +1/2 then may be rewritten as a relation (2.35)

$$F_{\frac{1}{2}}(\eta_f) = \int_0^\infty \frac{\sqrt{\eta}}{1 + exp(\eta - \eta_f)} d\eta \tag{2.35}$$

We now use the simplified approximation of Joyce-Dixon (2.36)

$$\eta_f = \ln(\xi) + \frac{1}{\sqrt{8}}\xi \tag{2.36}$$

As we remember, the scattering component that corresponds to the lattice scattering is equal to -1/2 for P type silicon so if we consider again the equation (2.31), we are obliged to calculate the Fermi integral of order zero (2.37) and its first-order derivative (2.38).

$$F_{s+\frac{1}{2}}\left(\frac{E_f}{k_b T}\right) = \ln\left(1 + \exp\left(\frac{E_f}{k_b T}\right)\right) \tag{2.37}$$

$$F'_{s+\frac{1}{2}}\left(\frac{E_f}{k_b T}\right) = \frac{1}{1 + \exp\left(-\frac{E_f}{k_b T}\right)} \tag{2.38}$$

Our term $P(N,T)$ may now be rewritten as (2.39).

$$P(N,T) = \frac{1}{\left(1 + exp\left(-\frac{E_f}{k_b T}\right)\right) \cdot \left(ln\left(1 + exp\left(\frac{E_f}{k_b T}\right)\right)\right)} \tag{2.39}$$

Considering now (2.33) and putting (2.36) into (2.39), we can easily trace the function $P(N,T)$ (Fig. 2.16).

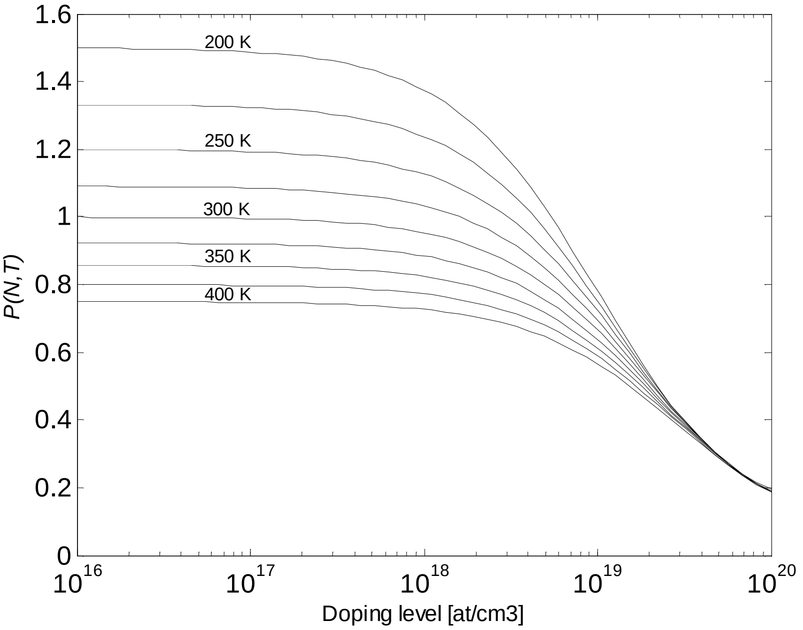

Fig. 2.16 The *P*(*N*,*T*) factor in a function of the doping level *N* and temperature *T* for the P type Silicon.

2.2.3 Experimental data

It has to be clearly said, that every model has its limitations and they have to be precisely known if one wants to predict the characteristic of the device during the design stage. In the next section we will try to give an overview on data published by now by different research groups and analyze how accurate results may be achieved by using the Kanda's model.

Results reported by now

A good synthesis of all works that have been done in experimental evaluation and modeling of piezoresistivity phenomena was published in 2002 by Toriyama and Sugiyama [45]. In fact, it has to be said that there are just a few works that focus on experimental verification of piezoresistance coefficients and even in them, measurements are limited to a few values and for narrow ranges of temperatures or doping levels. The most important conclusion from [45], is the Fig. 2.17.

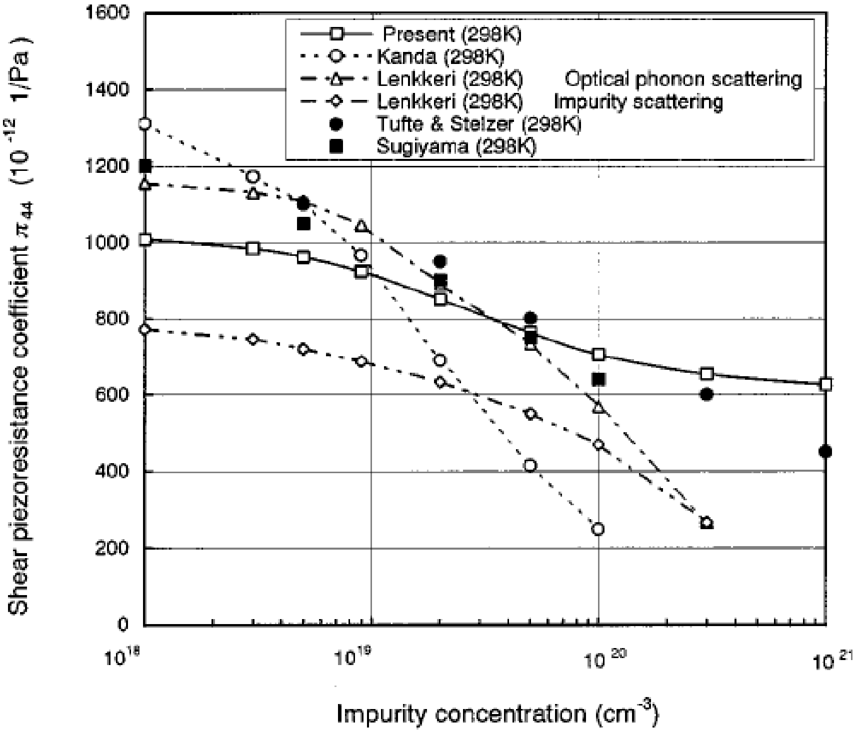

Fig. 2.17 The shear piezoresistance coefficient π_{44} for the P type silicon as a function of the doping level: existing experimental data (solid dots) and models (dashed lines) [45].

As one can see, experimental data presented by Tufte and Stelzer are quite coherent with those published by Sugiyama. Unfortunately, measurements were taken only at the room temperature. If we look carefully, we can easily remark that the piezoresistance coefficient may be the linear function (in a semilogarithmic scale) of the doping level for a range of impurity concentration of about $10^{18} \div 10^{21}$ at/cm^3 what is sometimes done for engineering approximations [51]. There is, however, a great inconvenient of such an approximation, namely that it tells us nothing about the temperature dependence and thus, the thermal drift of sensitivity can not be foreseen.

Considering models presented by different authors, it may be remarked that there is a large spread between them what is a result of different approaches and it confirms that the problem of clear and precise description of piezoresistivity is not a trivial task. First thing that we can see is that for very high concentrations ($>10^{20}$ at/cm^3) only one model is close to the experimental data but on the other hand it underestimates the piezocoefficient for the low doping concentrations. Moreover it saturates at 10^{18} at/cm^3 and will never reach the values for low doped silicon published by Smith (Table 2.4). For the reasons that will be explained later like strong thermal coefficient of resistance and taking into account that sensitivity drops rapidly for high doping levels, there is no need to design a strain gauges with the impurity concentration higher than a few of 10^{19} at/cm^3, so for the device design, model should be rather precise for lower doping levels. Looking again at Fig. 2.17, we may conclude that the best model that we could use is the Lenkkeri model based on the theory of optical phonon scattering but unfortunately, it is valid only for the room temperature. Thus, in conclusion, the only model that is temperature dependent, easy to compute and, at a time, it fits well the very wide range of doping concentrations $10^{16} \div 3\cdot10^{19}$ at/cm^3 is the Kanda model and thus, it was chosen to design our device.

2.2.4 Mobility issue

Another important parameter that has to be precisely known in order to build a good model of strain gauge is the carriers' mobility, which is a crucial factor determining the resistance value and its thermal drift.

The carriers are drifting in a bulk material when exposed to the electric field, but their motion is somehow limited by various scattering mechanisms that have many sources such as crystal lattice or material defects, to name but a few. In fact, we may distinguish three basic scattering mechanisms as follows:

- Defect scattering
- Carrier-carrier scattering
- Lattice scattering

As one can easily remark, the physically-based model that takes into account all above mentioned phenomena should be quite complex as the mobility value, as well as the piezoresistance coefficient value, are doping and temperature dependent. As a results, often the physically-based model do not correspond to measured values and semi-empirically models are used where some parameters are tuned in order to fit data.

Over the years, the mobility was thoroughly studied and there were several attempts that have been presented. In fact, if one wants to model exactly the mobility, three basic issues have to be taken into account. Firstly, at low electric fields the main scattering mechanism is the phonon scattering and the so-called low field mobility has to be calculated. Then, at the other end for the higher fields, the maximal mobility value is limited by carrier-carrier scattering and increased lattice scattering what oblige us to find the saturation carrier velocity. Finally, one has to find the suitable transition between these two extremes. In literature, the mostly known mobility models are:

- Caughey and Thomas model [52]
- Arora model [53]
- Klassen model [54]
- Dorkel-Leturq model [55]

All these approaches are widely used to calculate the mobility as a function of temperature and the doping level.

Mobility dependence on the doping level and temperature

It seems to be intuitive that for higher doping levels, the increased number of carriers causes that the carrier-carrier scattering component plays an important role in limiting the saturation velocity and thus, the mobility has to decrease with higher impurities concentration. Nevertheless, for ultra high concentration there are some additional effects like impurities clustering which affects the mobility. Also it was observed in literature there is also much stronger temperature dependency for lower doping concentrations. In the work of Boukabache and Pons [56], the models that were presented above were used to calculate the thermal coefficient of resistance *TCR* using the resistivity definition (2.40), which was compared to the experimental data obtained by Bullis in early fifties [57] (Fig. 2.18).

$$\rho = \frac{1}{q\mu N} \tag{2.40}$$

where q is an elementary charge, μ is a carrier mobility and N is a doping level. It has to be emphasized that such an approximation is only valid if we consider that the resistance is a linear function of the temperature.

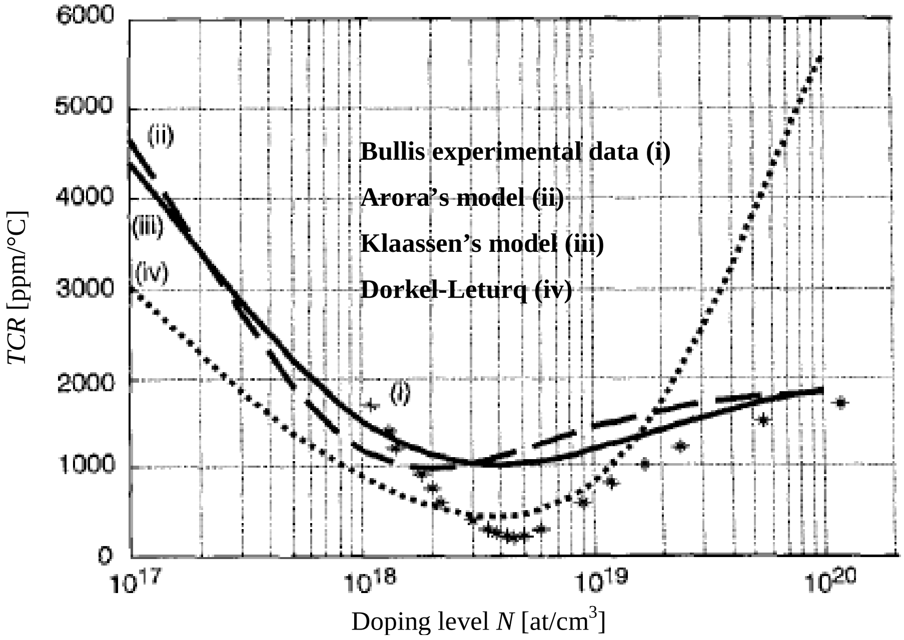

Fig. 2.18 Thermal coefficient of resistance *TCR* as a function of doping level *N* [55].

What can be easily remarked form this figure is that models fit experimental data only at some regions i.e. Dorkel-Leturq model suits best the range of $10^{18} – 10^{19}$ at/cm^3 while it fails completely for the higher concentration values. Nevertheless, the proper choice of model has to be done basing on the literature or self obtained experimental data.

In chapter four, we will present the results of the experiment that provided us with data obtained by fabricating the samples of different doping concentration and measuring their *TCR* coefficient but now, basing on the literature data [59], we will chose the Arora's model that suits best experimental data.

The model developed by Arora is a classical semi-empirical approach when theory based model taking into account the lattice scattering effect in range of 150-400K and hole-hole scattering for the same temperatures range was fitted to the experimental data.

In the final form, the holes mobility in a bulk semiconductor μ in a function of doping level N and temperature T is given by the following formula (2.41).

$$\mu = 54.3 \cdot T_N^{-0.57} + \frac{1.36 \cdot 10^8 \cdot T^{-2.23}}{1 + \left[\left(\frac{N}{2.35 \cdot 10^{17} \cdot T_N^{2.4}}\right)\right] \cdot 0.88 \cdot T_N^{-0.146}} \tag{2.41}$$

where

$$T_N = \frac{T}{300}$$

The mobility value as a function of two variables *N, T* may be then traced as it is presented in Fig. 2.19.

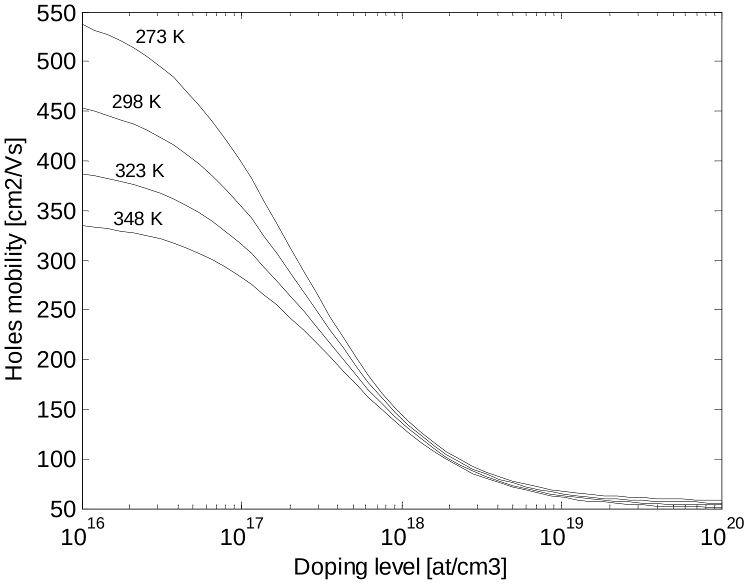

Fig. 2.19 Holes mobility value in bulk silicon as a function of Doping concentration *N* and temperature *T*.

At this moment, we are able to predict membranes mechanical deformation due to the applied pressure and calculate corresponding stresses that appear in it. We then know how strain gauges resistance will be affected by knowing the piezoresistance model. Moreover, we can predict how strain gauges will response on temperature by using both piezoresistance and mobility model. Now we will deal with the basic electronic read-out circuit that allows us to obtain useful electrical signal at the output of the sensor that is proportional to the applied pressure.

2.2.5 Electrical readout circuit

In this short subchapter, a theory and properties of the simple circuit used for the resistance measurement along with some supply issues that may significantly affect its performances will be discussed.

Wheatstone bridge

The Wheatstone bridge, which is one of the oldest and simplest instrument for the measurement of the unknown resistance, was invented in 1833 by Samuel Hunter Christie and then improved in 1843 by Sir Charles Wheatstone. The basic schematic of such a device is presented in Fig. 2.20.

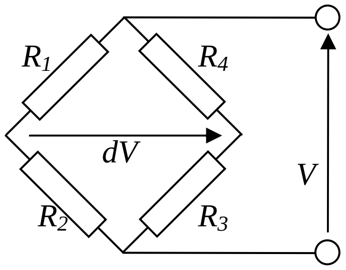

Fig. 2.20 The basic layout of the Wheatstone bridge.

The principle of the measurement is based on an assumption that one of the resistance i.e. R_1 is unknown while in other two branches resistors R_2, R_3 have fixed values and R_4 is an adjustable resistance. During the measurement, the bridge is supplied by the voltage V and by adjusting the resistance value of R_4 we search for the bridge equilibrium which occurs at the zero current flow between two brunches (dV=0). The unknown resistance value R_1 may be then calculated by applying Kirchhoff's laws to the bridge what leads us to the formula (2.42).

$$R_1 = \frac{R_4 R_2}{R_3} \tag{2.42}$$

Let us consider the more general case in which all four resistors may change. In such a case, the output voltage dV in a function of four resistances and supply voltage is given by (2.43).

$$\frac{dV}{V} = \frac{R_2}{R_1 + R_2} - \frac{R_3}{R_3 + R_4} = \frac{R_2 R_4 - R_1 R_3}{(R_1 + R_2)(R_3 + R_4)} \tag{2.43}$$

If we assume that each resistance value R_i will change by the ΔR_i and the following relation (2.44) is fulfilled, we can rewrite (2.43) in the general form (2.45).

$$R_1 \approx R_2 \approx R_3 \approx R_4 \approx R_0 \tag{2.44}$$

$$\begin{aligned}\frac{dV}{V} = \frac{1}{4R_0}\Bigg\{&\left[R_2\frac{\Delta R_2}{R_0} + R_4\frac{\Delta R_4}{R_0} - R_1\frac{\Delta R_1}{R_0} - R_3\frac{\Delta R_3}{R_0}\right] + \\ &-2\left[R_1\left(\frac{\Delta R_2}{R_0}\right)^2 + R_3\left(\frac{\Delta R_4}{R_0}\right)^2 - R_2\left(\frac{\Delta R_1}{R_0}\right)^2 - R_4\left(\frac{\Delta R_3}{R_0}\right)^2\right]\Bigg\}\end{aligned} \tag{2.45}$$

As one can notice, it is possible to distinguish two terms of (2.45), the linear and the nonlinear one. Because resistance variations ΔR_i are usually much smaller than the resistances R_i themselves, we can easily neglect the second-order term. If we apply additionally (2.44), the general relation (2.45) may be simplified to (2.46).

$$\frac{dV}{V}=\frac{1}{4R_0}\left(\Delta R_2+\Delta R_4-\Delta R_1-\Delta R_3\right) \tag{2.46}$$

As it can be remarked, in order to maximize the bridge sensitivity, ideal solution is to use four strain gauges system where two pairs of resistors will change their resistance by the same value but with the opposite sign, then the sensitivity of the bridge for resistance change may be expressed as follows (2.47).

$$\frac{dV}{V}=\frac{\Delta R}{R_0} \tag{2.47}$$

One feature that makes the Wheatstone bridge very convenient for sensor application is its ability to compensate the temperature effects on the measurement. Let us consider that each resistance R_i may change with temperature T obeying the quadratic law (2.48).

$$R_i(T)=R_{i0}\cdot\left[1+\alpha_i T+\beta_i T^2\right] \tag{2.48}$$

Where α_i and β_i are respectively first and second order thermal coefficients of resistance. Then (2.43) may be extended to the following form (2.49).

$$\begin{aligned}\frac{dV(T)}{V}&=\frac{R_1R_2}{\left(R_1+R_2\right)^2}\cdot\left[(\alpha_2-\alpha_1)T+(\beta_2-\beta_1)T^2\right]+\ldots\\ &\ldots+\frac{R_3R_4}{\left(R_3+R_4\right)^2}\cdot\left[(\alpha_4-\alpha_3)T+(\beta_4-\beta_3)T^2\right]\end{aligned} \tag{2.49}$$

Applying again (2.44) we then obtain (2.50).

$$\frac{dV(T)}{V}=\frac{1}{4}\left\{\left[(\alpha_2-\alpha_1)+(\alpha_4-\alpha_3)\right]\cdot T+\left[(\beta_2-\beta_1)+(\beta_4-\beta_3)\cdot T^2\right]\right\} \tag{2.50}$$

The general conclusion that may be formulated is that the thermal drift of the output voltage *dV* is caused only by the differences between thermal coefficients of resistances among resistors that form the bridge. In other words, in the ideal case when the process reproducibility is perfect, even if each resistor is characterized by an enormous *TCR* value, the bridge will compensate it and the thermal coefficient of output voltage will be equal to zero.

Supply issues

There is one issue that may affect significantly the performance of the designed sensor, namely the supply type. If we look again at Fig. 2.20, in order to obtain a useful output signal *dV,* the bridge has to be biased by the supply voltage *V*. There is, however another possibility where we may force the constant current. The advantage of such a solution was presented in details by Tanaskovic in [58] and will be now recalled. One of the most important parasitic effects that influence the sensor performance is the temperature and thus, it is highly desirable that sensor output signal would be temperature independent. As we showed in the previous section, the thermal drift of the output voltage is directly compensated by the bridge itself, but there is also the second parameter that is influenced by the temperature, namely the sensitivity. Considering again equations (2.25) and (2.47) we may formulate the simplified relation that describes the sensitivity of the bridge on the applied pressure for two cases: constant voltage supply S_v (2.51) and constant current supply S_i (2.52).

$$S_v = \frac{dV}{\Delta P}\frac{1}{V} = \frac{\Delta R}{\Delta P}\frac{1}{R} = \frac{1}{\Delta P}\pi \cdot \sigma \tag{2.51}$$

$$S_i = \frac{dV}{\Delta P}\frac{1}{I} = \frac{\Delta R}{\Delta P} = \frac{R}{\Delta P}\pi \cdot \sigma \tag{2.52}$$

where ΔP is an applied differential pressure while π represents effective piezocoefficient that depends on both, the doping level and the crystallographic orientation. Symbol σ is an average stress induced by the applied differential pressure (detailed calculations will be explained in the next chapter). We may then, calculate the thermal drift of sensitivity for two cases (2.53-2.54).

$$TCS_v = \frac{1}{S_v}\frac{\partial S}{\partial T} = \frac{1}{\pi}\frac{\partial \pi}{\partial T} + \frac{1}{\sigma}\frac{\partial \sigma}{\partial T} \tag{2.53}$$

$$TCS_i = \frac{1}{S_i}\frac{\partial S}{\partial T} = \frac{1}{\pi}\frac{\partial \pi}{\partial T} + \frac{1}{R}\frac{\partial R}{\partial T} + \frac{1}{\sigma}\frac{\partial \sigma}{\partial T} \tag{2.54}$$

If we analyze these two expressions and assume that the thermo-mechanical stresses that appear in the structure are small, we may then neglect the last term of each equation and formulate general conclusions about these two solutions. Firstly, if we supply our bridge with the constant voltage, the thermal drift of the sensitivity TCS_v will depend only on the thermal drift of the piezocoefficient itself $TC\pi$. Thus, if we look again at the Fig. 2.16, it is quite clear that the trade-off between the sensitivity on the applied pressure and the TCS_v is unavoidable. More precisely, the doping level which allows us to obtain very low TCS_v is greater than about $2 \cdot 10^{19}$ at/cm^3 what implies the significant drop of the piezocoefficient value in comparison to its maximal possible value.

On the other hand, analyzing (2.54) we can easily remark that TCS_i depends on both $TC\pi$ and TCR value. If we take into consideration the fact that $TC\pi$ is always negative and TCR is always positive, we may easily imagine that if temperature increase, the loss of sensitivity caused by $TC\pi$ may be partially compensated by the increase of resistances values in the bridge and thus, increased voltage bias. Moreover, if it is possible to choose the doping level in such a way that absolute value of $TC\pi$ and TCR are equal and according to (2.54), it would be possible to obtain TCS_i which is equal to **zero** what offers the passive temperature compensation of the sensitivity (Fig. 2.21).

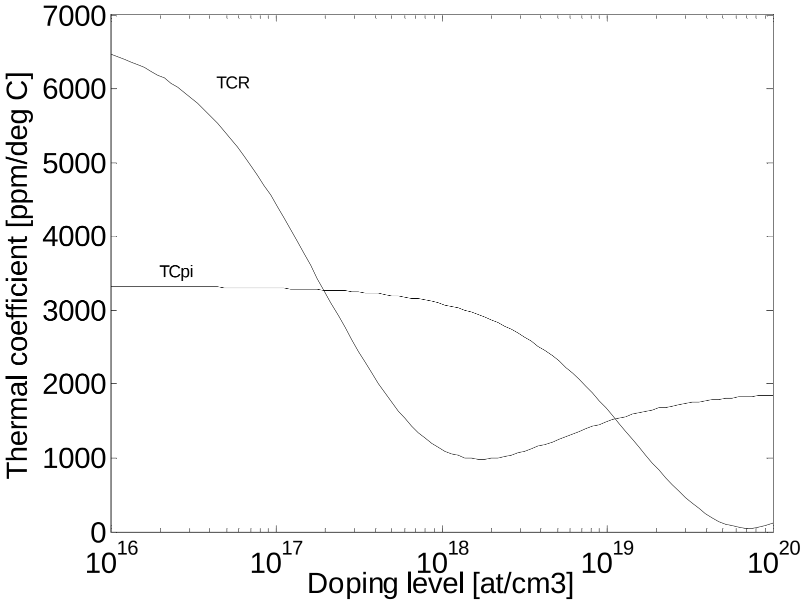

Fig. 2.21 Absolute values of the $TC\pi$ and TCR in function of the doping level.

It may be observed that there are two points where curves cross and if we compare it again to Fig. 2.16, we may notice that the most convenient uniform doping level, if one wants to keep high sensitivity and its low thermal drift, is about $2\cdot10^{17}$ at/cm^3. One thing that should be emphasized, is that both curves are based on models that differs from the experimental data, so in the reality the doping level that should be used may be rather chosen at higher doping level especially if we analyze data published by Bullis [57] (Fig. 2.18).

2.3 Analytical model

All previously presented mathematical descriptions like mechanical behavior or piezoresistivity modeling, may now serve us as a base that allows us to create the complete mathematical description of the piezoresistive pressure sensor at a system level.

2.3.1 Basics

An overview of the model

As it was shown earlier, in general, the piezoresistive pressure sensor is based on a thin plate called the membrane which bends due to applied the differential pressure, what causes that bending stresses appear in it. Those stresses are translated into the relative resistance change of the strain gauge by the piezoresistivity phenomenon. The four gauges form the Wheatstone bridge that allows us to obtain at its output, the voltage signal which is proportional to the applied differential pressure.

To start with, let us use an output-input approach. Recall that if we consider that our bridge is supplied by constant voltage *V*, the output voltage is given by (2.46) and the maximum of output voltage (maximal sensitivity) is reached when two pairs of resistors will change their resistance by the same value but with the opposite sign. In order to understand how to achieve it, let us remind the general formula that links stress value with corresponding resistance change (2.55).

$$\frac{\Delta R}{R} = \pi_l \sigma_l + \pi_t \sigma_t \tag{2.55}$$

Considering Fig. 2.15, and keeping in mind that almost all standard silicon wafers are cut in (100) plane, we may easily conclude that the best direction for strain gauge for such a plane is <110> family (Fig. 2.15). Such a strain gauge, conducting current *I* is exposed two the longitudinal and transversal stress components as shown in Fig. 2.22.

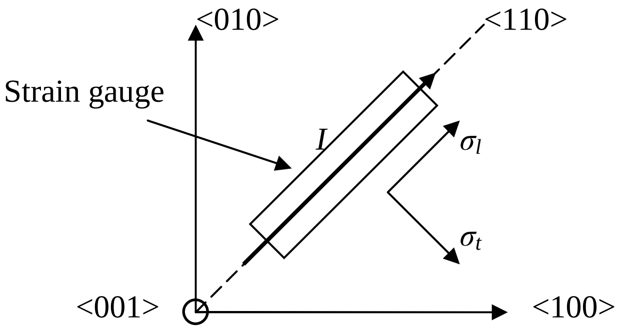

Fig. 2.22 A strain gauge in (100) plane placed along <110> direction and conducting current *I*, corresponding longitudinal σ_l and transversal σ_t stress components are also shown.

Going further, corresponding longitudinal and transversal piezocoefficients π_l and π_t must be then calculated by using the transformation based on Euler's angles (2.28) with the following angles values:

- $\varphi = 45^o$
- $\psi = 0^o$
- $\theta = 0^o$

Then, necessary stress components are given by the following relations (2.56-2.57).

$$\pi_l = \frac{\pi_{11} + \pi_{12} + \pi_{44}}{2} \tag{2.56}$$

$$\pi_t = \frac{\pi_{11} + \pi_{12} - \pi_{44}}{2} \tag{2.57}$$

If we put (2.56) and (2.57) into (2.55) we obtain (2.58).

$$\frac{\Delta R}{R} = \frac{\pi_{11} + \pi_{12} + \pi_{44}}{2}\sigma_l + \frac{\pi_{11} + \pi_{12} - \pi_{44}}{2}\sigma_t = \frac{\pi_{11} + \pi_{12}}{2}(\sigma_l + \sigma_t) + \frac{\pi_{44}}{2}(\sigma_l - \sigma_t) \tag{2.58}$$

Considering the values of piezocoefficients given in a Table 2.4, we may easily estimate that the main contribution to the resistance change is given by the second term of (2.58) $(\pi_{44} / 2) \cdot (\sigma_l - \sigma_t)$. According to that, in order to control the sign of the resistance change, gauges are placed in regions where always one of the stress component is much higher that the second one. For a positive resistance change the longitudinal stress component should be higher whereas for the negative change the situation should be opposite.

Gauge position issues

Let us consider two basic shapes of the membranes: the square and the rectangular one. The stress distributions are calculated by using the theory presented in the first part of this chapter. On Fig. 2.23, the difference between longitudinal and transversal stress components $(\sigma_l - \sigma_t)$, which is the crucial factor in (2.58), is shown for such a square membrane. Similar distribution is presented for the rectangular membrane with the length to width ratio equal to four in Fig. 2.24.

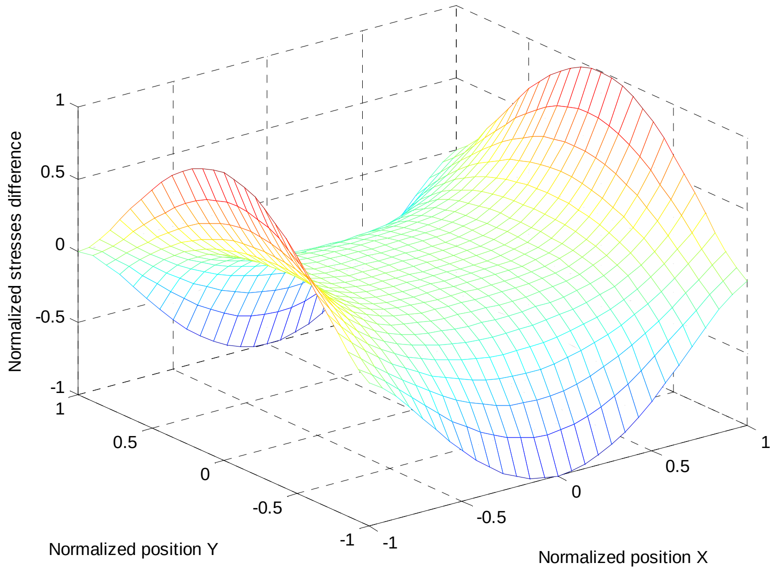

Fig. 2.23 Normalized longitudinal σ_x and transversal σ_y stress difference for square membrane with lateral dimensions 2 by 2 units.

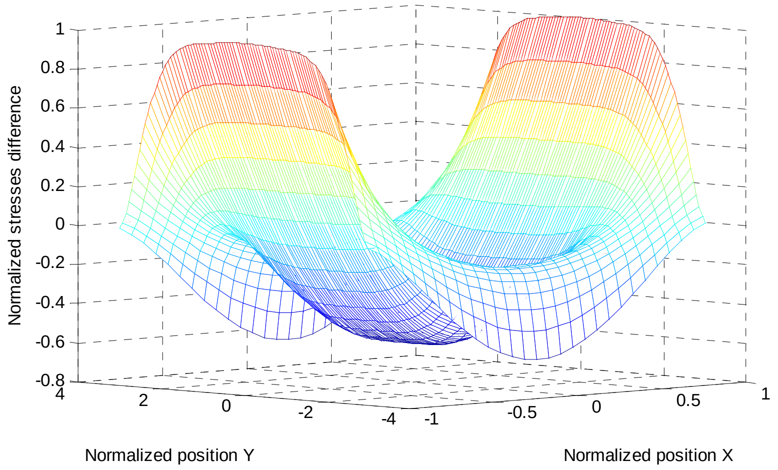

Fig. 2.24 Normalized longitudinal σ_x and transversal σ_y stress difference for rectangular membrane with lateral dimensions 2 by 8 units.

As one can see, in case of the square membrane, gauges should be placed at membranes borders and each gauge in one pair should be located at the opposite edges. Moreover, all gauges should be parallel and follow the same direction (Fig. 2.25 a). In case of the rectangular membrane, if we keep the gauges parallel, one pair (placed on shorter edges) should be positioned analogically like in case of square membrane but the second one, should be shifted to the membrane centre in order to obtain the same magnitude of the resistance change (Fig. 2.25 b). There is, however, one other interesting possibility. If we place two pairs of gauges in the middle of the rectangular membrane, but positioning one pair perpendicularly to the second one (Fig. 2.25 c), we may obtain similar sensitivity value as in the first configuration, but the stress gradient will be significantly lower and, as a result, less sensitive to the misalignment errors.

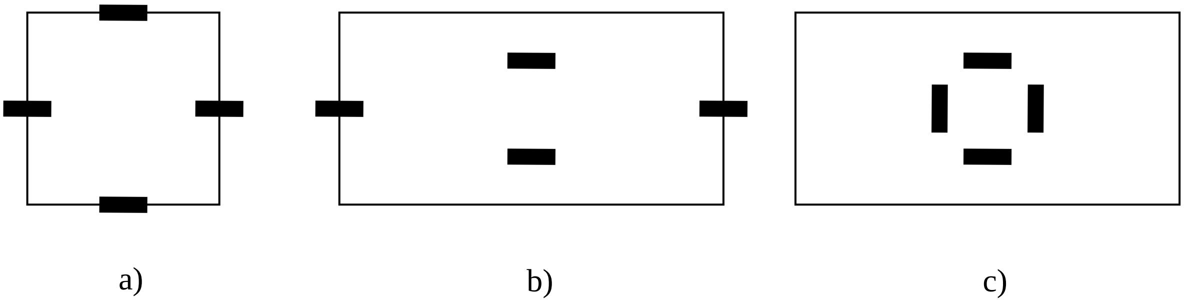
a) b) c)

Fig. 2.25 The possible configuration of four strain gauges for different types of the membranes.

To summarize, it has to be remarked that the choice of proper configuration has to be adapted for the application and there is no easy answer which configuration is the best one. The square membrane offers high sensitivity and occupy small amount of space but the stress gradient is high so any mistakes caused by the fabrication process at the alignment stage may significantly affect sensor performance. On the other hand, rectangular membrane with gauges in configuration shown at Fig. 2.25 c, offers much lower stress gradient, but slightly reduced sensitivity and additionally occupies more space.

The stress gradient and gauges length

The stress gradient issue becomes important when we are talking about gauges resistance value. The gauge resistance R affects the power consumption of the bridge supplied by the constant voltage V, where total dissipated power P (neglecting interconnections) is equal to (2.59).

$$P = \frac{V^2}{R} \qquad (2.59)$$

As one can easily see, in order to decrease the power consumption, the resistance should be as high as possible. The problem is that the resistance value according to its definition depends only on its resistivity which is a function of doping level and resistor dimensions. So generally, for a fixed doping level which is chosen rather to reach the desired piezoresistance coefficients and thermal drifts (see chapters 2.2.2 and 2.2.5), increasing the resistance value may be done only by increasing the gauge length. If we then take into account that the total resistance variation is caused by the **average** stress in the strain gauge, it become obvious why the high stress gradient is limiting the resistance dimensions.

2.3.2 Gauges modeling

Recall that until now, we considered our system as a membrane with for strain gauges that response to mechanical stresses and a Wheatstone bridge that converts such a response in the electrical output signal. We even discussed basic gauge parameters as its lateral dimensions or doping level and presented its impact on sensors performances such a sensitivity or thermal drifts. Now we will put some light on the gauge itself. We will discuss its simplified fabrication process and present parameters that are necessary to model it correctly.

Fabrication process

The implanted strain gauge is fabricated by performing the ion implantation into crystalline structure of silicon membrane and thus, creation of P type resistors isolated by the P-N junction. Because, as we said earlier, highest piezoresistance coefficients are achievable for the P type silicon (see Table 2.4), usually the Boron implantation into N-type substrate is performed. As it was described earlier, the stress value is the highest at the membrane surface, so in order to obtain highest possible sensitivity, a low junction depth is desired. Thus, avoiding the channeling effect, which is observed [60] when ion implantation is performed directly into crystalline silicon, we use a thin SiO_2 layer (called the screening oxide) through which the implantation is done. Such a layer is used to force scattering of implanted Boron atoms and simulates the amorphic behavior of dopants. Simplified view of the whole process that creates the strain gauges is presented below (Fig. 2.26).

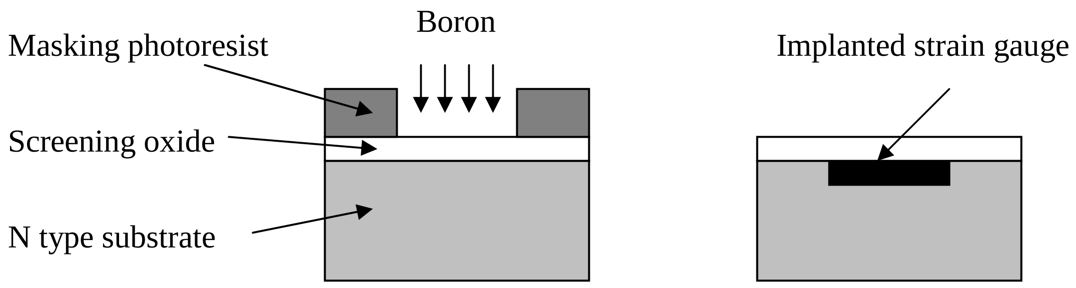

Fig. 2.26 The simplified process of the P type gauge formation on the N type substrate.

Because of such a fabrication processes, gauges have usually extremely high length-to-deep ratio. Moreover the doping profile is not uniform over the gauge depth what has its consequences that will now be presented.

Diffused layers modeling

The dopants, which are introduced to the crystalline structure, do not contribute to the current conduction because they are electrically inactive (no chemical bonds between implanted Boron and Silicon atoms). In other words, the impurities atoms have to replace the silicon ones in the crystal lattice in order to accept some electrons form silicon and create holes that may participate in the current conduction. Thus, an energy that is needed to replace silicon atoms has to be delivered to dopants. The most common method is a very high temperature annealing (about 1000 ºC) which increases particles movement and facilitate atoms exchange. Such an approach, however, causes that dopants may easily "flow" in the atomic structure and the redistribution of impurities due to diffusion process is unavoidable. Such a phenomenon is clearly presented in Fig. 2.27. Basically, after the implantation process impurities are placed in a relatively thin layer which is located at the depth which corresponds to the maximal dopants concentration *Nmax*. Such a depth *Rp* is a function of implantation energy but also depends on the dopant type (more precisely on the impurity atom weight) and on the screening oxide thickness. It was shown [61], that impurity profile may be successfully described by using the Gaussian distribution, so dopants will be distributed with some statistical spread around *Rp* value.

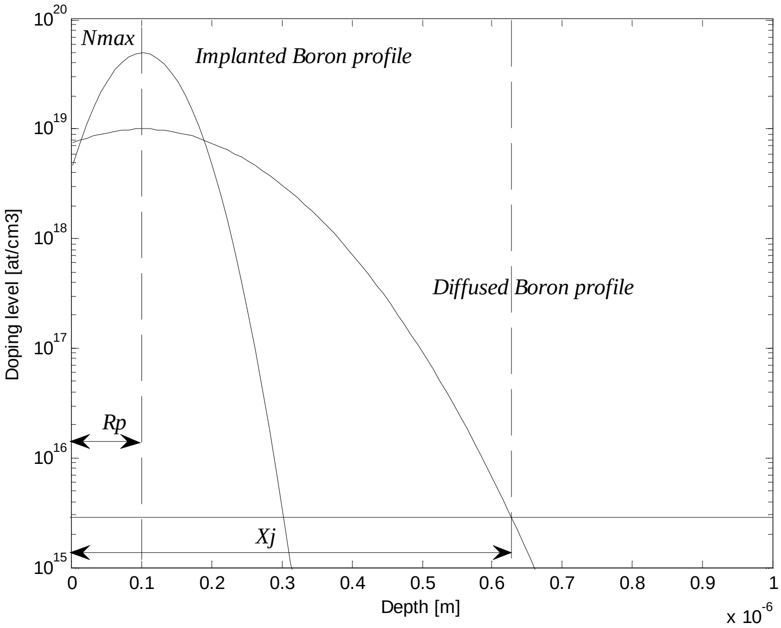

Fig. 2.27 Implanted profile evolution due to the high temperature thermal treatment.

During the high temperature annealing, impurities will diffuse naturally because of their gradient according to the Fick's law [62]. It causes that the Gaussian distribution will "lower" and the junction depth *Xj* increase. The junction depth *Xj* is defined as a distance from the surface at which the concentration of dopants is equal to the intrinsic impurities concentration in the substrate.

It has to be emphasized that the Gaussian approximation of the doping profile may be used with success only if we apply a classical high thermal treatment. The modern techniques of rapid thermal annealing that base on the extremely rapid and extremely high temperature spike annealing produce profiles that vary from Gaussian ones. Nevertheless, if we consider that the membranes thicknesses that are used for pressure sensors fabrication are ranging from few to few tents of micrometers and, at the same time, classical thermal treatment allows us to produce junctions less then 0.5 μm thick in case of Boron and even 0.1 μm for BF_2 ions doping [63], we may conclude that the Gaussian description of the impurity profile remains a good choice. Namely, the function that describes such a profile is given by (2.60).

$$N(x) = N_0 \exp\left(- \frac{(x - Rp)^2}{X^2} \right) \qquad (2.60)$$

where N_0 corresponds to the maximal concentration value, *Rp* is a previously described implantation peak and *X* is a parameter that defines the distribution spread and is **proportional** to the junction depth.

If the intrinsic impurities concentration of the substrate N_i is known, the junction depth may be calculated by applying (2.61).

$$Xj = \left(X \sqrt{\ln\left(\frac{N_i}{N_0} \right)} \right) + Rp \qquad (2.61)$$

To prove that such an approximation may be successfully used, a doping profile that was obtained by Boron implant through 400 Å thick screening oxide layer, with an implantation energy of 25 keV and an implanted dose of $2.8 \cdot 10^{14}$ at/cm^3 which was then annealed at 1000 ºC for 30 minutes was fabricated. After that, the doping profile was extracted by using Secondary Ion Mass Spectroscopy (SIMS) [64]. We than compared the experimental profile with its Gaussian approximation what is presented in Fig. 2.28.

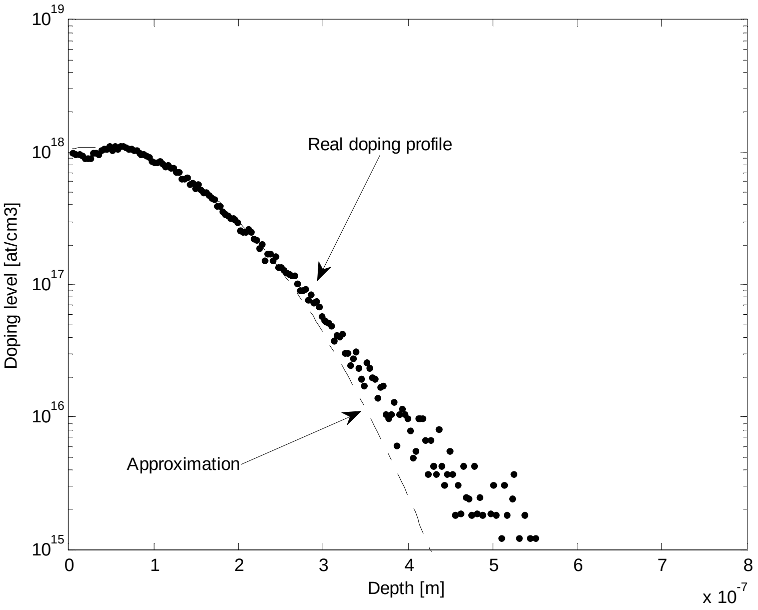

Fig. 2.28 Comparison of the real doping profile and its approximation using Gaussian distribution.

It clearly confirms that such an approximation may be successfully used for a such kind of thermal annealing process. In order to model such a diffused layer which has the nonuniform doping profile, all "macroscopic" or rather effective parameters of such a gauge like: resistance, piezoresistance coefficients and thermal coefficients of resistance have to be integrals over the junction depth. If we for instance want to calculate the resistance value of such a diffused layer, we have to use the resistance definition.

Remark:

In the case of the diffused layer when the doping profile plays an important role, the parameter that is usually given is the sheet resistance value not the resistance itself. The sheet resistance value does not depend on the lateral dimensions of the resistor but depends only on the junction depth. It is defined as resistance per square because the length and width of the resistor are considered to be equal.

The sheet resistance definition of the layer which has the thickness of *Xj* and in which we consider only holes transport (P type silicon) is given by (2.62).

$$R_{sheet} = \frac{1}{\int_0^{Xj} q\mu(x)N(x)dx} \tag{2.62}$$

Where $q = 1.602\cdot10^{-19}$ C is an elementary charge, $\mu(x)$ is the holes mobility and $N(x)$ is the dopants concentration, both are depth dependent.

Let us now calculate the gauge response for the applied pressure taking into account the impurity profile. In the beginning we have to consider that according to chapter 2.1, we are able to calculate the deformation of a membrane and thus, the corresponding stresses that appear into it. We may then calculate the average stress value in the resistor by integrating the stress function over the gauge area and then calculate its value at each depth by assuming that it changes linearly at is was shown (Fig. 2.11 c).

Let us then assume that our diffused layer consists of n parallel layers of small thickness Δx in which we can consider all parameters to be depth independent. As we know, in the parallel configuration, the global resistance value R is a sum of inverted resistance values of each i-th resistor R_i. If we apply the same law to our case, a global strain gauge resistance value that is changed $R+\Delta R$ due to the applied pressure (2.25) obeys the following relation (2.63).

$$\frac{1}{R+\Delta R} = \frac{1}{R_1+\Delta R_1} + \frac{1}{R_2+\Delta R_2} + \cdots + \frac{1}{R_n+\Delta R_n} = \sum_{i=1}^{n} \frac{1}{R_i+\Delta R_i} = \sum_{i=1}^{n} \frac{1}{R_i\cdot\left(1+\pi_{li}\sigma_{li}+\pi_{ti}\sigma_{ti}\right)} \tag{2.63}$$

If we then consider again (2.62) in a slightly changed form (2.64)

$$R_i = \frac{1}{q\cdot\mu\cdot(i\Delta x)\cdot N(i\Delta x)\cdot\Delta x} \tag{2.64}$$

we can then reformulate (2.63) into (2.65).

$$\frac{1}{R+\Delta R} = \sum_{i=1}^{n} \frac{q\cdot\mu(i\Delta x)\cdot N(i\Delta x)\cdot\Delta x}{\left[1+\left(\pi_l(i\Delta x)\cdot\sigma_l(i\Delta x)+\pi_t(i\Delta x)\cdot\sigma(i\Delta x)\right)\right]} \tag{2.65}$$

Assuming that Δx is infinitely small and relation (2.66) is true, we may than obtain the final form of (2.65) shown as (2.67).

$$n\cdot\Delta x = Xj \tag{2.66}$$

$$\frac{1}{R+\Delta R}=\int_{0}^{X_j}\frac{q\cdot\mu(x)\cdot N(x)dx}{\left[1+\left(\pi_l(x)\cdot\sigma_l(x)+\pi_t(x)\cdot\sigma_t(x)\right)\right]} \qquad (2.67)$$

Uniformity of the doping profile

As we can see, all presented calculations were used in order to model the piezoresistive pressure sensor which takes into account the real doping profile of the implanted strain gauge. The question that may appear at this moment is: do we really need to take into account the doping profile? The answer is positive. Very often for simplicity reasons, only the doping concentration at the surface is taken into account and all corresponding calculations are performed. Although, in case of the resistance calculation designers are conscious of such a problem, in case of piezoresistance coefficient and *TCR* it is not always obvious. In case of *TCR* there are some works [58, 59] that put some light on the problem of the profile nonuniformity influence on the *TCR* value. In case of piezoresistance effective coefficient Tufte and Stelzer [36] observed and concluded that the average coefficient of the diffused layer would be only **slightly** larger than in the uniform layer with the same surface concentration. Just after them, Kerr and Milnes [37] showed that **there is** a contribution of the profile type on the piezoresistive behavior but it is **independent** on the diffused layer depth. The thing is that they both assumed that the stress distribution over the layer depth is **constant** what was quite obvious those days when achievable membrane thicknesses were many times thicker that the junction depth but nowadays, when we reach the membrane thicknesses in order of a few micrometers it is definitely not the case. Let us to be quantitative and analyze three basic gauge parameters that are important in view of the overall pressure sensor performance: its resistance, thermal coefficient of resistance *TCR* and the effective piezoresistance coefficient.

For simpler analysis that takes into account only two doping parameters (easier visualization), we assumed that the *Rp* parameter is constant and equal to 0.05 µm what seems to be the reasonable value for standard, medium energy (15-70 keV) Boron implantation. Then, the gauge sheet resistance, *TCR* and piezoresistance coefficient values for both uniform and nonuniform doping profile (Fig. 2.28) were calculated for surface concentrations ranging from 10^{17} to 10^{20} at/cm^3. The whole procedure was repeated for four different junction depths that varied from 0.15 µm to 0.9 µm. The substrate impurities level was set to $2\cdot10^{15}$ at/cm^3 what corresponds to the typical average wafer resistivity of 1-6 Ω·cm. Finally, the ratio between two values for different profile types was calculated and traced.

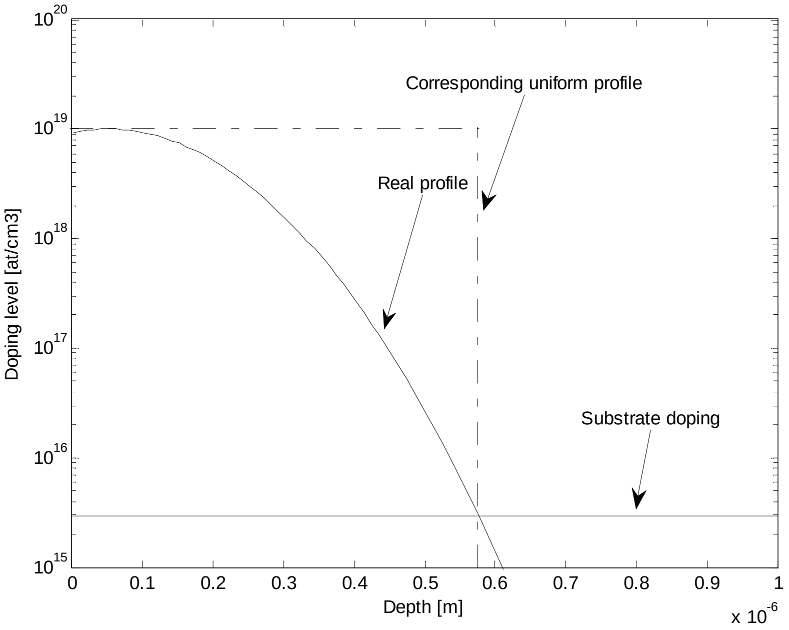

Fig. 2.28 The real Gaussian profile used for gauge parameters calculations and the corresponding uniform profile.

All ratios for three gauge parameters are traced below in order to easily visualize errors that may arise as a result of the improper model choice. The relative error between resistance values is shown at Fig. 2.29.

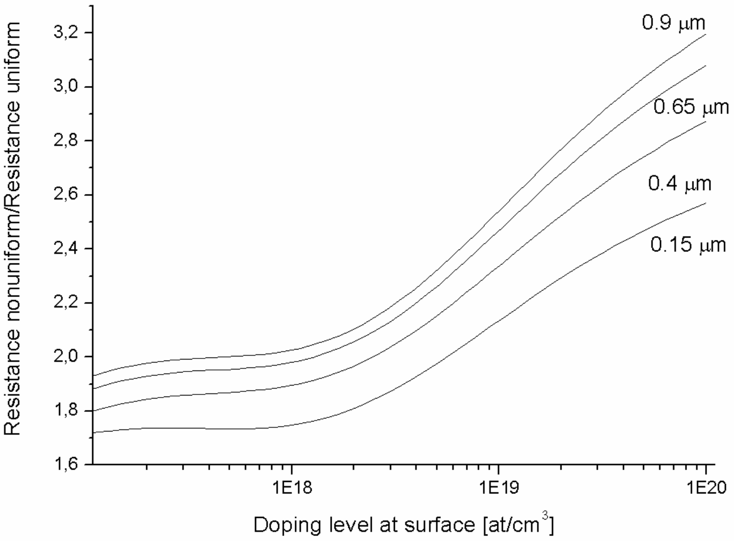

Fig. 2.29 Ratio of two resistance values obtained by using uniform and nonuniform doping profile with the same surface concentration for different junction depths.

We may clearly conclude that taking into account uniform doping level causes enormous overestimation of the resistance value and the minimal error for low surface concentrations reaches over **70%** and increase with the doping level. Moreover, as one can easily remark, the junction depth is also an important factor and it cannot be neglected in calculations.

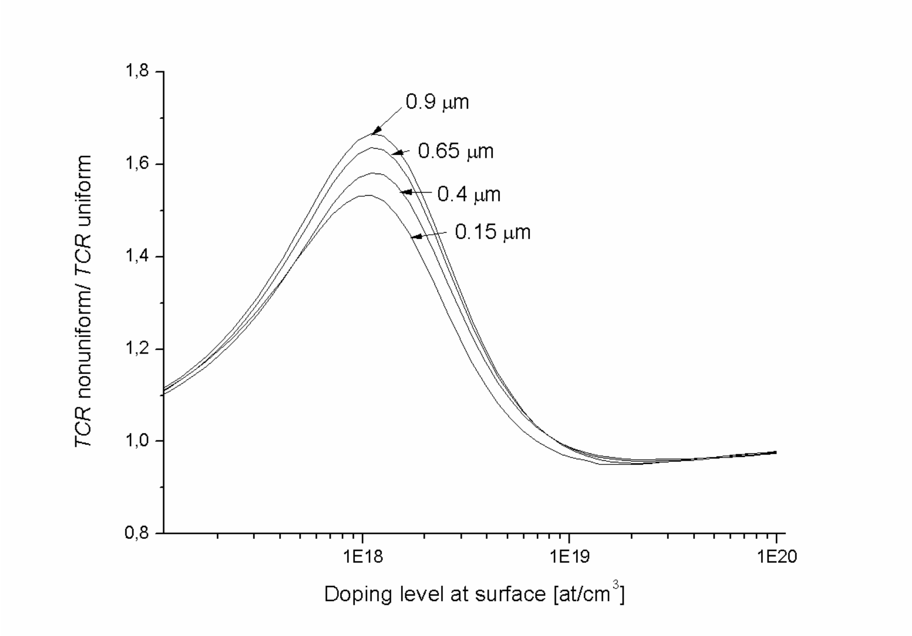

Fig. 2.30 Ratio of two *TCR* values obtained by using uniform and nonuniform doping profile with the same surface concentration for different junction depths.

Fig. 2.30 shows us the *TCR* ratios and the thing that may be remarked instantly is that the error depends on the surface doping concentration. If the impurity level is close or higher to 10^{19} at/cm^3 or lower than 10^{17} at/cm^3, one can say that there is no difference (smaller than 5%) between two approaches, but if we look at the region that is close to 10^{18} at/cm^3, the relative error may easily reach over **70%** what can not be definitely neglected. Moreover, the influence of the junction depth may be also observed for that region. The reason why there is the doping level range where the error is much higher than around it is that the *TCR* coefficient curve in function of the doping level varies significantly around the impurity level of 10^{18} at/cm^3 (Fig. 2.18). Thus, if we assume that the quite remarkable part of the current circulates in the region which is relatively close to the maximal doping concentration, if neighboring concentration has the *TCR* value that change rapidly, the whole region is then strongly affected. In regions where the function is quite slowly changing, the error may be neglected.

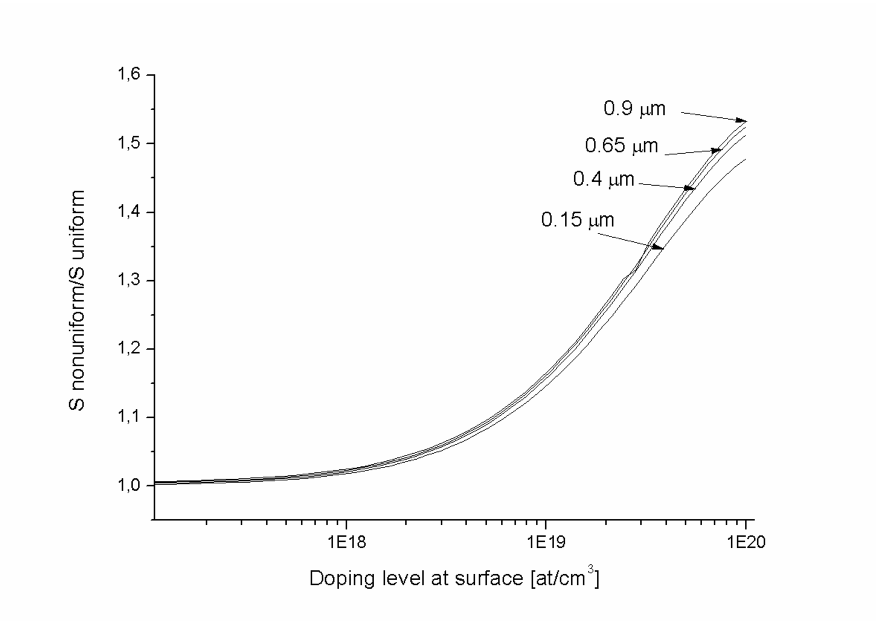

Fig. 2.31 Ratio of two effective piezoresistance coefficient values obtained by using uniform and nonuniform doping profile with the same surface concentration for different junction depths. Membrane thickness is equal to 50 µm.

The last value that is analyzed is the piezoresistance coefficient of the gauge (Fig. 2.31). As one can see the differences are definitely not enormous (less than 10%) if we consider the doping level that is lower than a few 10^{18} at/cm^3 (less than 5%) what seems to be quite intuitive if we look again at Fig. 2.16 and remark that the piezoresistance coefficient are almost constant up to this value. Above that doping level the difference increase dramatically as the drop of the piezocoefficients is quite steep (Fig. 2.16) and a doping profile plays a role. Nevertheless, the influence of the junction depth may be neglected. Such a conclusion strongly confirms result presented in literature but as we remarked earlier, results presented by Tufte and Stelzer as well as Kerr and Milnes were obtained with an assumption that the stress value is **constant** over the junction depth. The results presented above (Fig. 2.31) were calculated for the gauge that is positioned on the membrane with thickness of 50 µm and some load was applied in order to calculate the resistance change. Such a value may easily fulfill the condition about the constant stress value. Let us, however, repeat the same procedure but this time we take into consideration the membrane with thickness of 4 µm where the stress value changes significantly over the gauge depth. Fig. 2.32 shows us the result of such an analysis.

It may be easily remark that differences are much more visible, as well as the junction depth influence is. They are of course not as high as in the case of resistance or *TCR* value but they rather should be considered.

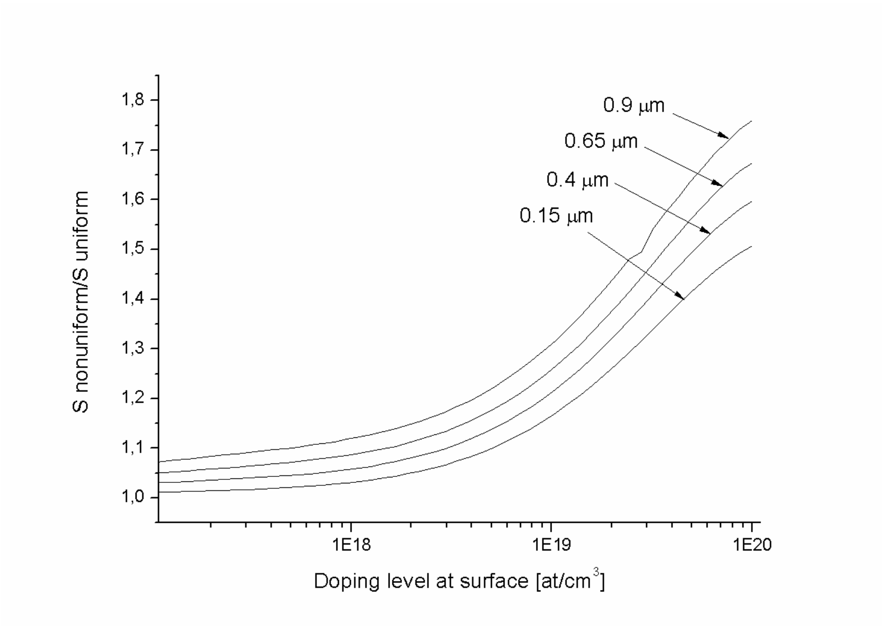

Fig. 2.32 Ratio of two effective piezoresistance coefficient values obtained by using uniform and nonuniform doping profile with the same surface concentration for different junction depths. Membrane thickness is equal to 3 μm.

The analysis presented above shows us, that in order to model properly the pressure sensor as a system, the more detailed than simple surface concentration value, strain gauge modeling fabricated by ion implantation process has to be performed **taking into account the nonuniformity of the doping profile**. Of course there are some cases, like the particular doping levels, where such a methodology does not increase the model accuracy but for most of the cases it is a highly recommended approach especially if we are talking about **resistance value** and ***TCR* coefficient**.

2.3.3 Noise sources and noise modeling

Another parameter that also affects significantly the piezoresistive sensor performance is the noise value. Basically, the noise limits the minimum detectable pressure value, so in other words, the high noise may cause that the low output signal value may be completely undistinguishable form it. It has to be remarked that, for simplicity reason, all noises which has its origin in interconnections are neglected, so only noises that appear in an implanted structure are taken into account. Such an approach may be successfully applied while it is commonly known that the higher resistance value generates higher noise so if we consider the Wheatstone bridge, only gauges may be treated as noise sources. According to the literature data [65, 65], there are two basic components of a noise: a thermal component often called the Johnson noise and 1/f noise.

Johnson noise

The first one, called also the thermal noise, has its origin in the scattering due to crystal lattice motion caused by the temperature. If we then consider a single resistor that has a resistance value of *R* and is operating at given absolute temperature of *T* in the range of frequencies between f_1 and f_2, the total RMS value of the noise voltage is given by (2.68).

$$V_{Johnson} = \sqrt{4k_bTR(f_2 - f_1)} \tag{2.68}$$

where k_b is the Boltzmann’s constant.

1/f noise

The second noise component is called 1/f noise and it appears at low frequencies when DC bias is applied (like in the case of the Wheatstone bridge). Its origin is found in random mobility fluctuations and random carriers trapping processes near the surface. If our resistor is considered to be operating under DC bias of *V*, a total RMS value of 1/f noise in it may be derived by using Hooge’ formula (2.69).

$$V_{1/f} = \sqrt{\frac{\alpha V^2}{N}\ln\left(\frac{f_2}{f_1}\right)} \tag{2.69}$$

The parameter α is called the Hooge coefficient. It depends on the quality of silicon and varies [66] from $5\cdot10^{-6}$ for the high quality substrate to $2\cdot10^{-3}$ for very poor, full of defects silicon. As it can be seen all noise components depend on total number of carriers (resistance value) so according to the previous chapter if the doping profile of strain gauge has to be taken into account in order to correctly calculate the corresponding noise components.

2.4 Analytical model vs. FEM approach

Until now, we have been talking about analytical models of all phenomena that are needed to explain and describe the complex behavior of the piezoresistive pressure sensor. However, as we mentioned earlier, the most common approach that is used in today’s designer’s world is a FEM analysis. There are some good works [67, 68] describing the modeling process of the piezoresistive pressure sensors and they all confirmed that such a method is reliable enough to be the tool that allows us to design predictable devices. In the next section we will try to present shortly, the principles of the pressure sensor modeling by using this technique. Then we will try to understand where lays the power and the weakness of the FEM analysis.

Consequently, we will compare the result to our analytical model based one and we will explain at which level the two techniques really differ. Furthermore, we will show that the analytical model may be enough accurate to replace FEM analysis at some stage of the design project. Finally, we will present the dedicated CAD simulation tool that was created in order to predict the behavior of the piezoresistive pressure sensor. All analysis concerning mechanical modeling were performed in commonly known ANSYS® environment whereas all fabrication related issues in SILVACO-ATHENA® package.

2.4.1 FEM model

Basic assumptions

According to the previous chapter, the full description of the piezoresistive pressure sensor is not a trivial task while a multi-physics analysis has to be envisaged. Basically, three main domains have to be taken into account: mechanical, electrical and the thermal one. Thus, all domains have to be coupled with each other in order to fully describe and simulate our system (Fig. 2.33).

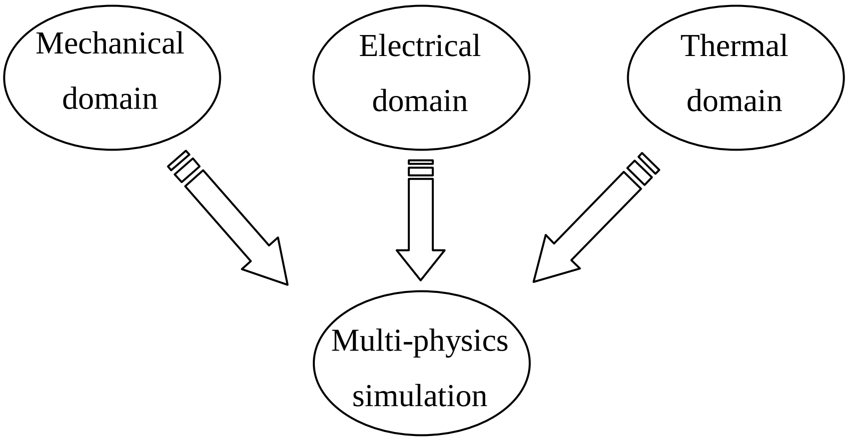

Fig. 2.33 Structural view of tasks needed for the pressure sensor modeling.

In the mechanical domain, FEM method allows us to model almost everything for solid materials. Every shape, every material properties may be modeled what offers the extreme level of flexibility. Let us look carefully at our case of the pressure sensor where the basic structure, without packaging, looks as follows (Fig. 2.34).

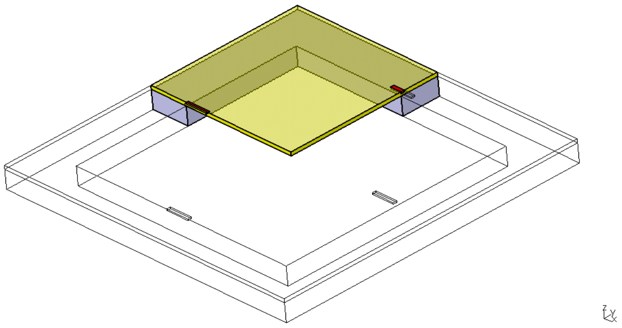

Fig. 2.34 The basic structure of the piezoresistive pressure sensor which is the base for 3D FEM model.

Every time when one wants to model something, in order to save the time, it is necessary to apply all simplifications that are possible without loosing accuracy. One of such a simplification is offered by the symmetry. As we can see at Fig. 2.34, the pressure sensor may be modeled just in one quarter (shaded area) because other three quarters are symmetrical. If we then construct the finite element model of such a structure it may look as it is shown in Fig. 2.35.

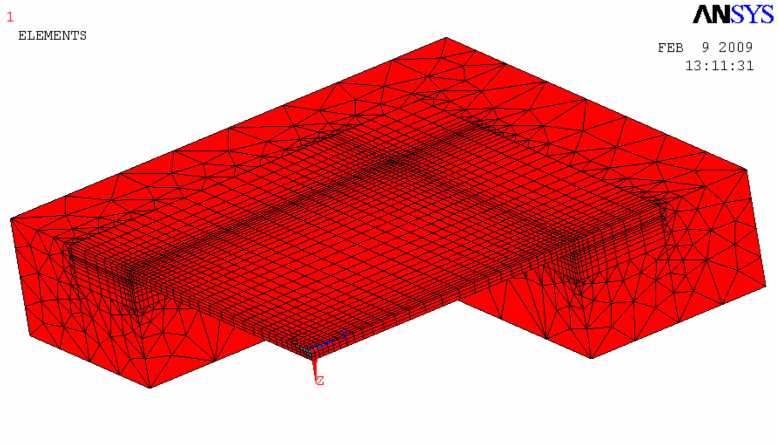

Fig. 2.35 The finite element model of one quarter of the pressure sensor.

As we can see, the zones where the highest accuracy is needed (clamping borders in case of the square membrane (see Fig. 2.23)) are meshed with much smaller elements in comparison to the others. Such an approach, as each additional node adds some number of equations, reduces significantly the number of equation that have to be solved and thus, the computing time.

The important question is then, how to model the boundary conditions so in other words where to “fix” the structure. The answer is not easy and there is a literature [69] dealing with such a problem and we will not analyze it but present only some basic issues. For example, we may block the “floor” so create an artificial plane (Fig. 2.36 left) that will simulate the virtual substrate on which we place the sensor and do not allow to move nodes that are adjacent to it. Such an approach seems to be close to the reality if extremely rigid package is applied. On the other hand if the packaging is not very rigid and the sensor is clamped, for example at its borders, the whole structure will bend due to the pressure applied. Such a case needs different clamping condition what is presented in Fig. 2.36 (right).

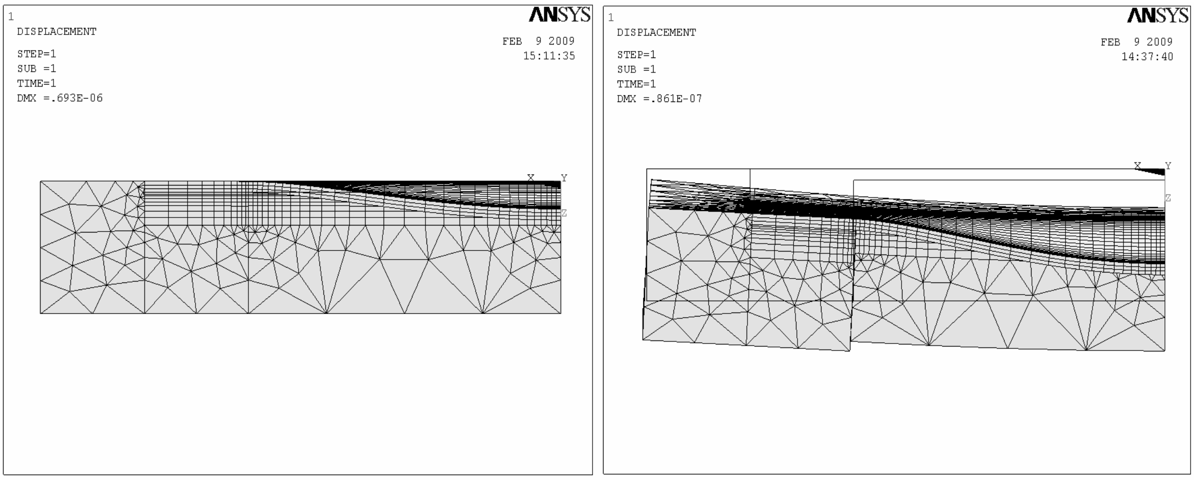

Fig. 2.36 The result of applied pressure on the modeled structure for two different clamping conditions: clamped “floor” (left) and clamped edge (right).

We have performed all analysis using the clamping condition as in the second case. For an analysis, the elements that support anisotropy (SOLID 186, SOLID 187, see [70]) were chosen. The stiffness matrix was then introduced and the coordination system was then oriented to the desired direction. As a result, the stress distribution was obtained as it is shown on a figure (Fig. 2.37 left). If we zoom on the section near the membranes border (Fig. 2.37 right) we can easily remark that the stress distribution over the membrane thickness, changes linearly as it was shown earlier.

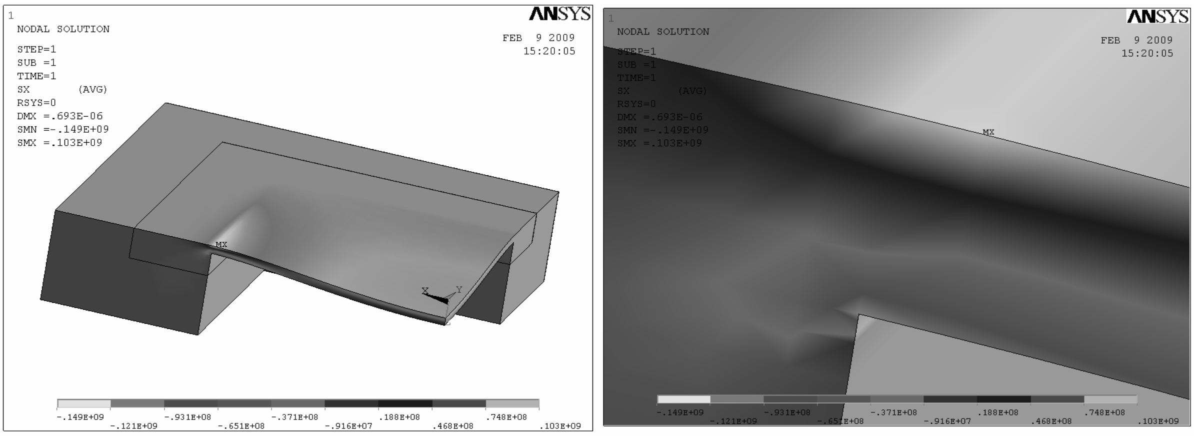

Fig. 2.37 Stress distribution in the modeled structure (left) and zoomed view at the clamping zone (right).

Coupled mechanical-electrical analysis

The second important part of our FEM simulation is the transduction of the mechanical stresses into gauge resistance change and this is the moment were the advantage of the analytical model appears. As we explained earlier, the gauge is the diffused layer that has a nonuniform doping profile that has to be taken into account. Firstly, in a FEM tool it is extremely difficult to apply to one material, any property that changes in one element. It implies that our diffused layer has to be modeled as a multilayer structure, where each layer has different values of doping level, as it is shown below (Fig. 2.38).

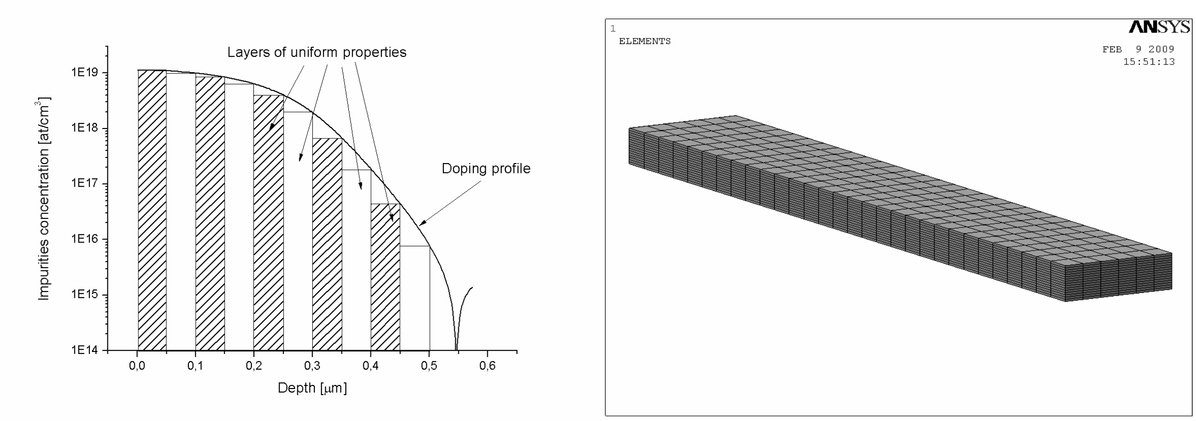

Fig. 2.38 The diffused layer profile and its approximation by the layer with uniform properties (left) with the corresponding FEM model (right).

Generally, the diffused layers are characterized by extremely high length-to-deep ratio when gauge which has few or even few tents of micrometers has a typical depth of about 0.5 μm. If we then take into account that each gauge has to be divided into several layers in order to model correctly all doping profile related effects, the length-to-deep ratio of each layer increases dramatically. For the numerical reasons and good convergence conditions of FEM analysis [71] it would be desired that each element is equilibrate in its three dimensions. Such a condition requires that in case of diffused layer modeling, each gauge has to be represented by an enormous number of finite elements, what increases drastically the model complexity and significantly affects the computing time.

Fortunately, if one wants to simulate the gauge behavior to the applied stress we do not need to create the whole model of a sensor with the strain gauges in it what would dramatically increase the number of elements and computing time. What we can do then, is to perform separately the mechanical analysis and then transfer the resulting stresses into gauge structure; such an operation is called the submodeling. As a result, we may obtain all interesting parameters like conduction current density, or potential distribution in gauge what leads us to the resistance change calculations. For example, the stress and electrical potential distribution in a strain gauge placed at the membrane border are shown below (Fig. 2.39).

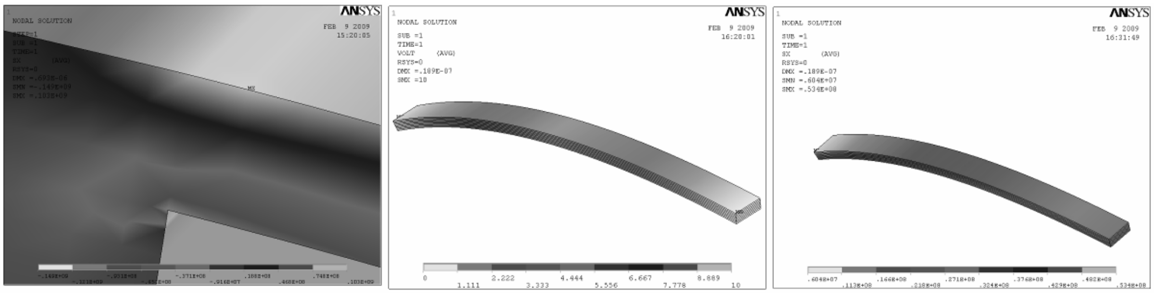

Fig. 2.39 Clamping zone of the membrane where the gauge is placed (left) the electrical potential distribution (centre) and the uniaxial stress value (right) in a gauge that was sub modeled.

In order to take into account the piezoresistivity effect, one has to use the proper element types that supports at the same time anisotropy and piezoresistive effect. In ANSYS® environment we have used SOLID 226 and SOLID 227 elements that perfectly combine these two features [70]. As a reference material property, the stiffness as well as piezoresistive coefficients matrices were introduced.

2.4.2 Analytical model advantages and drawbacks

The important thing that has to be emphasized here is that when introducing layer properties, we have to know exactly what doping profile is used. Then we have to use same models of piezoresistance and mobility that were used earlier in our analytical model. The obvious conclusion is that the difference between these two approaches may be **only visible** in a mechanical analysis while in analytical domain, perfectly clamped membrane with uniform thickness and basic shape may be easily modeled. Let us now to put some light on this problem.

Influence of clamping conditions

As we said earlier, the analytical model of the membrane assumes that the clamping is perfect, telling that there is no displacement at the membrane edges (2.10). Intuitively, such a condition should cause the wrong estimation of the stress value near that region. Let us take into account the plate, and defined *XYZ* Cartesian coordination system as it is shown in Fig. 2.40. For example, we may consider the square plate with the lateral dimension of 300 μm with the thickness of 5 μm. It will be loaded by uniform differential pressure of 13.33 kPa (100 mmHg). Now, we may trace the stress distribution along, for example, the *X* axis. For easier analysis, we trace the uniaxial stress value (σ_x) in a function of the distance from the membrane center (Fig. 2.41).

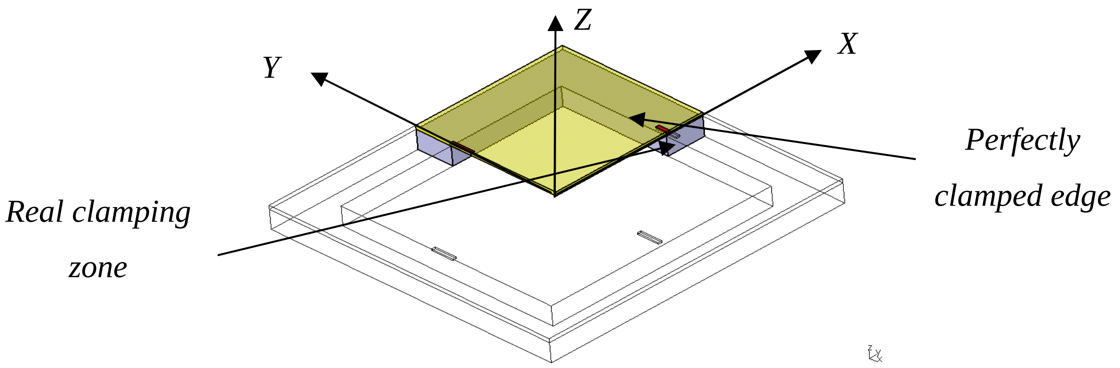

Fig. 2.40 The real clamped membrane model with marked perfectly clamped edge.

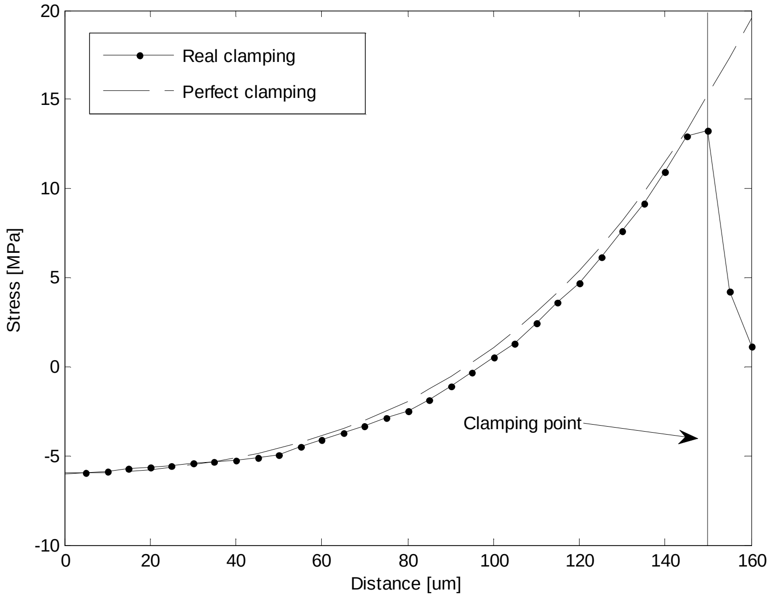

Fig. 2.41 Comparison of the stress distribution for the real and ideal clamping conditions.

One can remark, that the analytical model of the stress distribution fits well to results obtained by using the FEM methodology excluding the clamping zone. It implies that in case of the square membrane, using the analytical model may lead us to the overestimation of the sensibility at this region. On the other hand if we look again at Fig. 2.41, we may easily noticed that the error at clamping point reaches **15%,** what may be accepted in engineering calculations**.** For gauges that are placed partially at the substrate zone we considering the stress on the substrate zone is equal to zero. The useful feature is that in all square membranes, such an overestimation is systematic and may be taken into consideration by the designer. For the rectangular membrane, however, where gauges are placed in the middle, such an approach seems to be correct and provides is with much more accurate results.

Thermomechanical stresses

The second important problem that is not taken into account by the analytical model is the thermomechanical stress. Basically, we may define it as the unwanted stress that appears in the structure due to the mismatch between thermal coefficients of expansion between different materials that form the sensor structure. In other words, when the ambient temperature changes, the dilatation of two materials is different and thus, the stress distribution appears in the material what may cause the false strain gauge reaction to the applied pressure. Such a problem, however, as a crucial to the sensor performance was the subject that inspired a lot of R&D work in order to solve it. Generally, in case of silicon based pressure sensors, the membrane is in most of the cases made of silicon but the substrate that serves as a base of the sensor may be made of something different. It may be just silicon but in many applications the use of different kind of glass is envisaged. If we use silicon as the same material that the membrane is made of, the thermomechanical stresses do not plays the key role. However, in case of the most popular PYREX 7740® glass, the problem may become crucial. Fortunately, such a problem was overcome by changing the composition of the borosilicate glass. As a result, the SD-2 glass, which is characterized by almost identical thermal coefficient of expansion as silicon for a wide temperature range, appeared on the market (Fig. 2.42).

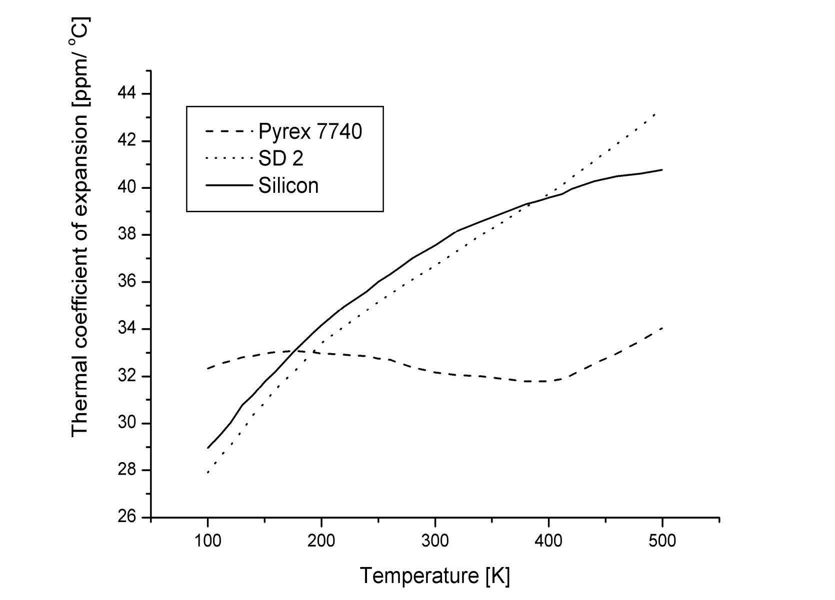

Fig. 2.42 Comparison of the thermal coefficient of expansion value for silicon, PYREX and SD-2 glass.

Thus, if one uses the modern material for the sensor fabrication, the thermomechanical stress exists but its influence may be significantly reduced.

Another problem may arise when we want to estimate the influence of the packaging on the sensor. Relatively rigid sensors are usually attached to the rigid packaging via soft elastic material like silicone or others. Such a composition adds another origin of thermomechnical stresses that are unwanted as the thermal coefficients of dilatation are often different. The influence of such a stress is extremely difficult to describe by analytical model as the soft elastic material are rather difficult to describe and in fact, the only way to estimate them precisely is a detailed and tedious FEM analysis. The solution that may be proposed to overcome such a problem could use results (stress distribution) of such a simulation that may be use as input data to our analytical model that may calculate other sensor parameters.

Conclusions

To summarize, two basic drawbacks of the analytical model were presented: perfect clamping conditions and neglect of the thermomechanical stress. Nevertheless, the real clamping condition affects the results only for the specific gauge configuration and the introduced overestimation is acceptable in engineering calculations. The influence of the second term, as we presented, may be decreased if someone use appropriate material for sensor fabrication. Of course in case of high mismatch between the two materials such a problem may affect the simulated results.

As we listed major drawbacks of analytical model, let us say something about the advantages of it. The first and the most impressive one is the computing time. We performed all calculations on a PC class computer with double core processor and 2 GB of RAM. One mechanical analysis of the structure presented at Fig. 2.35 without considering the FEM thermomechanical effects takes about 10 seconds. After that, the piezoresistive analysis is performed so the stress values are imported and the nonlinear-piezoresistive problem is solved. Such an analysis takes about 10 second depending on the gauge size (number of finite elements). It may look to be the very short time while the complete mechanical and piezoresistive analysis take about thirty seconds but the analytical model of the perfectly clamped membrane, performs mechanical, piezoresistive and thermal analysis (excluding thermomechanical effect) in just about 2 ms! (measured by the internal function of the programming environment). It may seem to be not an advantage if we want only to simulate the designed structure because twenty seconds is not a long time but, as we will present later, in order to optimize the design, a few thousands of model evaluations have to be performed. If we then multiply twenty seconds by, let us say, one thousand we obtain 334 minutes what gives us about 6 hours!!! It may be then desired to perform same task with similar results in about **4** seconds by using the analytical model.

2.4.3 Comparative analysis

As we mentioned, two approaches that may be used to model the piezoresistive pressure sensor, let us to quantitatively compare it in order to know how much they differ. In engineer's environment, the FEM simulation is established solution as a method that gives trustworthy results. In next section we will try to show that the analytical model may be also successfully used for that task. The FEM model used for that purpose was meshed few times in order to assure the convergence of the calculations and at the same time reduce its time.

We performed the simulation of the square membrane as it was used to calculate the stress distribution in the previous paragraph. All structure parameters that were used for simulation are listed below (Table 2.6).

Table 2.6 Structure parameters used for the FEM simulation

Parameter name	Value
Membrane length	300 µm
Membrane thickness	5 µm
N_0	$1.2 \cdot 10^{19}$ at/cm^3
Rp	0.05 µm
Xj	0.5 µm
Gauge length	30 µm
Gauge width	3 µm

As a result, the simulation provided us with the piezoresistor response to the applied differential pressure. Fig. 2.43 shows us the normalized sensitivity value (relative resistance change) in a function of the gauge length (1µm; 10µm; 20µm; 30µm) and a position on the membrane (the coordination system is the same as in Fig. 2.40). At the same graph, values obtained by using the analytical model are shown. As the membrane is square, the gauge orientation may be parallel or perpendicular to the membrane border. Values presented below are calculated for the perpendicular case.

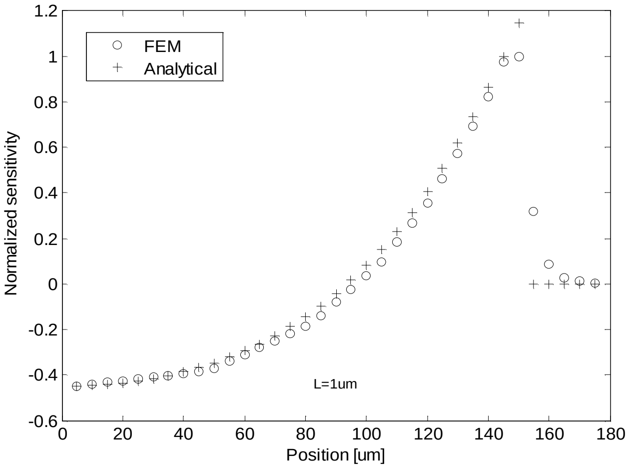

Fig. 2.43 a) Comparison of the normalized sensitivity value obtained by two different methodologies. Results are traced in the function of the gauge position on the membrane and the gauge length 1µm.

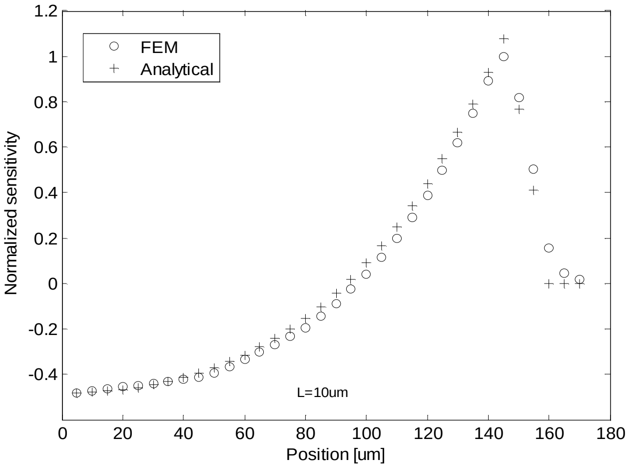

Fig. 2.43 b) Comparison of the normalized sensitivity value obtained by two different methodologies. Results are traced in the function of the gauge position on the membrane and the gauge length 10µm.

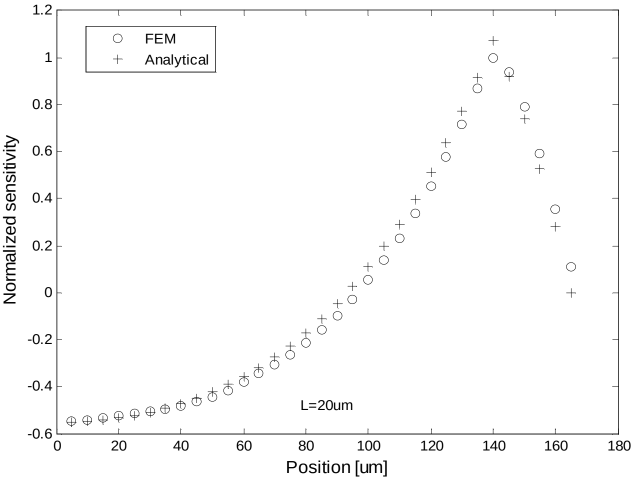

Fig. 2.43 c) Comparison of the normalized sensitivity value obtained by two different methodologies. Results are traced in the function of the gauge position on the membrane and the gauge length 20µm.

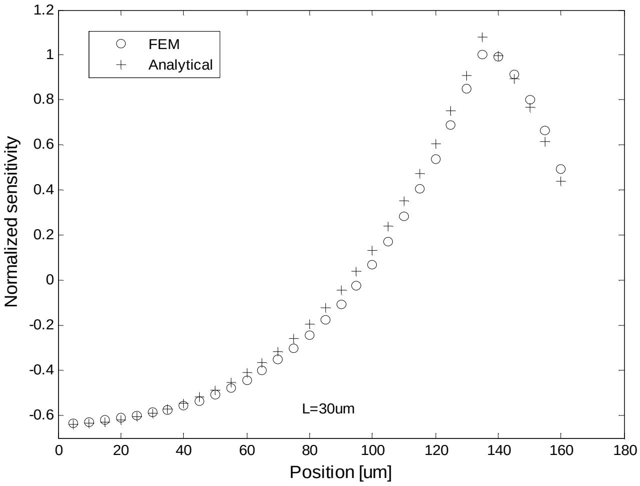

Fig. 2.43 d) Comparison of the normalized sensitivity value obtained by two different methodologies. Results are traced in the function of the gauge position on the membrane and the gauge length 30µm.

What can be easily remarked is, as we mentioned earlier, that the results obtained by using two different methodologies are in a very good agreement excluding the region of the clamping zone. Nevertheless, it has to be noticed that when we increase the gauge length, such a difference decreases what is a result of the averaging effect. If we consider the gauge length of 1 µm, it is affected by the local stress which changes rapidly as a function of position especially in the clamping region (Fig. 2.43). If we, however, use longer gauge, the effective stress will be an **average** over the gauge length. Thus, the high stress value near the membrane border is dominant over the smaller stress over the substrate and it cause that differences in perfectly and nonperfectly clamped model are less visible than in case of the very short gauge. If we, however, consider the gauge that is parallel to the membrane border we rather do not profit from the averaging effect as the width of the gauge is quite small (order of a few µm). Thus, the analytical model may provide us with the trustworthy results if the gauges are placed outside the clamping zone and if not, when the gauge length is high enough. As one can see at Fig. 2.43 c) if the gauge length is higher than about 8% (20 µm of 300 µm) of the membranes length the difference may be neglected. If gauge is placed close to the clamping zone, in the worst case where the gauge is parallel to the membrane border, the difference does not reach 20 % and is rather likely to be smaller (Fig. 2.43 a)).

2.4.4 Simulation tool

All above mentioned facts were used to construct the dedicated simulation tool. The idea was to create the computer program that may be used for piezoresistive pressure sensors simulation taking into account all specific phenomena that may be described by analytical models. It has to be emphasized that this tool was created to help in the design of the sensor which requirements were described at the beginning of this work. Thus, it is designed to cooperate with the simulation tool that is responsible for the electrostatic pressure generator and is a subject of the other work. Such a synergy f these two tools allows us to design correctly the self-testing pressure sensor taking into account all specific constraints for our project.

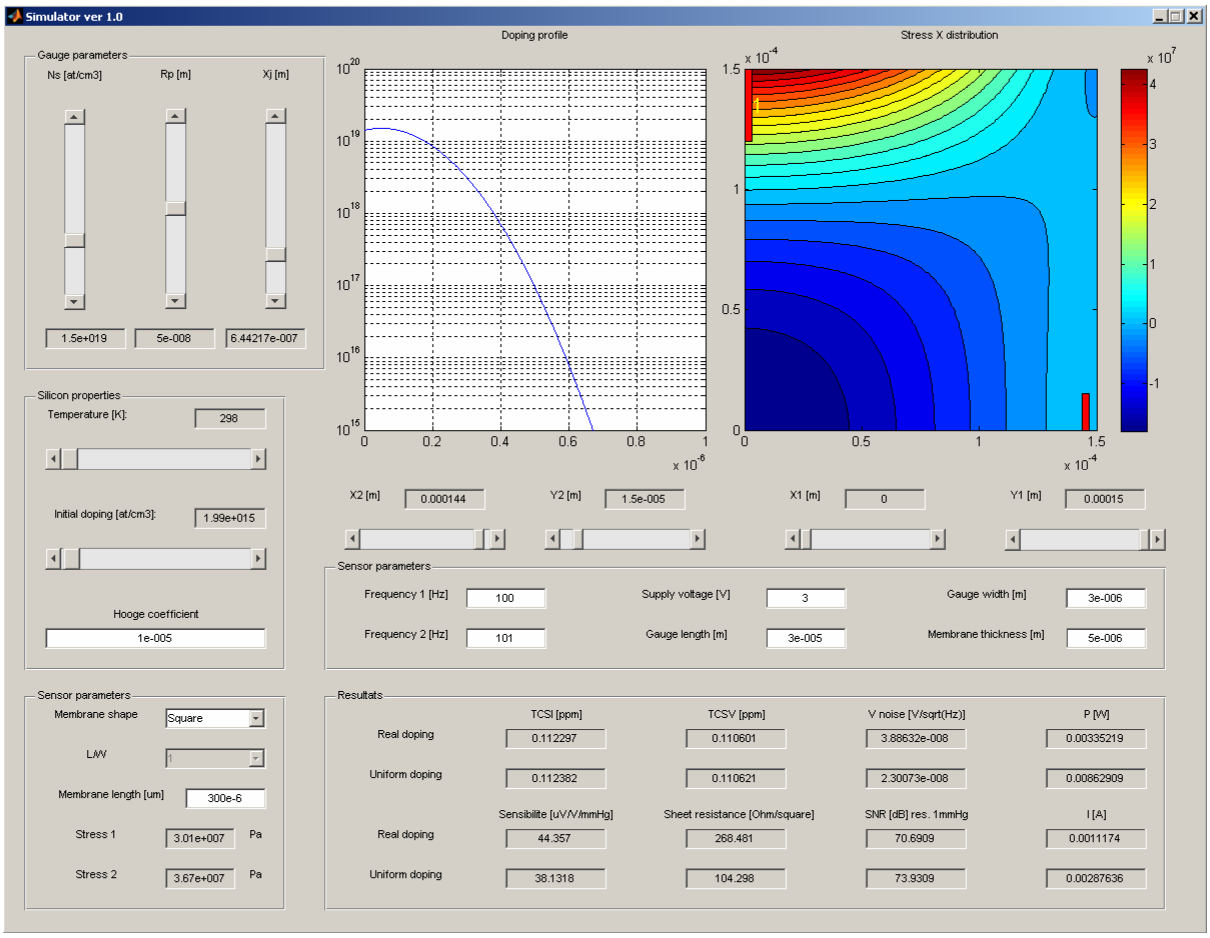

Gauge parameters

Ns [at/cm3]: 1.5e+019
Rp [m]: 5e-008
Xj [m]: 6.44217e-007

Silicon properties

Temperature [K]: 298
Initial doping [at/cm3]: 1.99e+015
Hooge coefficient: 1e-005

Sensor parameters

Membrane shape: Square
L/W: 1
Membrane length [um]: 300e-6
Stress 1: 3.01e+007 Pa
Stress 2: 3.67e+007 Pa

X2 [m]: 0.000144
Y2 [m]: 1.5e-005
X1 [m]: 0
Y1 [m]: 0.00015

Sensor parameters

Frequency 1 [Hz]: 100
Frequency 2 [Hz]: 101
Supply voltage [V]: 3
Gauge length [m]: 3e-005
Gauge width [m]: 3e-006
Membrane thickness [m]: 5e-006

Resultats

	TCSI [ppm]	TCSV [ppm]	V noise [V/sqrt(Hz)]	P [W]
Real doping	0.112297	0.110601	3.88632e-008	0.00335219
Uniform doping	0.112382	0.110621	2.30073e-008	0.00862909
	Sensibilite [uV/V/mmHg]	Sheet resistance [Ohm/square]	SNR [dB] res. 1mmHg	I [A]
Real doping	44.357	268.481	70.6909	0.0011174
Uniform doping	38.1318	104.298	73.9309	0.00287636

Fig. 2.44 The main window of the created simulation tool.

Main advantages of our tool were to be the speed of calculation and multi domain analysis. In order to create such a tool we used widely known MATLAB® GUI environment. The choice of such a tool instead of popular VISUAL C++ was driven by the capabilities and experience of the author in creating similar projects. Although, a similar approach has been already published [72], it does not treat the sensor in a such complex manner (gauge profile consideration, noise analysis etc.).

The main window of the tool is presented in Fig. 2.44 and shows the functionality of the tool.

As one can see, the tool is very simple and includes all parameters that the designer wants to know about the sensor.

The very left part of the window is dedicated to the sensor parameters that are introduced by the designer. In the top left corner, three parameters describing the gauge profile are introduced. Then, in the lower part, the parameters of silicon as its base doping and Hooge's coefficient as well as the external temperature may be set. Finally, the geometry of the sensor like its lateral dimensions, membrane shape and length to width ratio (rectangular membranes only) are fixed. The middle left part of the window is dedicated to definition of gauges lateral dimensions, supply voltage and operating frequency range (used for the noise calculation).

The upper part of the window is divided into two screens and is used only for visualization purposes. The center window presents current doping profile that is reconstructed basing on the three fully descriptive parameters whereas the top right window is used for a stress plot. For the simplicity reasons, the stress window plots uniaxial stress value and may be switched between longitudinal and transversal stress. Additionally, it covers only one quarter of the membrane because of symmetry reasons. Under the visualization windows, two sets of sliders are placed. They are responsible for the two gauges x and y position. Because as we said earlier gauges are placed in pairs, only two of them need to be simulated in order to simulate the whole sensors behavior.

The lower part is dedicated for the results. The tool provides us with the main sensor parameters such as:

- Sensitivity
- Gauge resistance
- Gauge RMS noise value
- SNR for minimum detectable pressure set to 1 mmHg
- Bridge power consumption
- TCS_i
- TCS_v

Presented tool is intended to be very simple and intuitive but at a time its capacities are relatively large as it takes into account all phenomena that were described in the analytical way and, at the same time, calculations are done almost in the real time mode (2 ms measured by the internal MATLAB® function).

2.5 Conclusions

As it was mentioned in the beginning of this chapter, on overview on the all physical phenomena that rule the piezoresistive sensor behavior were presented and described in an analytical way. The state of the art knowledge of the modeling was presented and the theory was explained. Next, the important issue considering the strain gauge modeling as the diffused layer was presented with emphasis on the doping profile modeling and the possible effects of wrong approach. In the third section, an overview on a FEM modeling was presented to be then compared to the analytical solution. The drawbacks and advantages of two approaches were presented quantitatively leading us to the conclusion that in many cases, the analytical model may be, if not the substitute, surely the solution that may provide us with trustworthy results. Moreover, we proved that in fact the FEM analysis of the pressure sensor is needed only in the mechanical domain because all piezoresistive or temperature effects on the electrical behavior of the strain gauge have to be introduced to the FEM simulator basing on the existing analytical models or existing experimental data. Finally, the dedicated design tool was presented and described. The next chapter will show us how to use the developed model in an efficient optimization procedure.

3 Design optimization and statistical analysis

The previous chapter was the base that allowed us to understand all issues that are related to the modeling of the piezoresistive pressure sensor. Nevertheless, it showed us how to simulate the behavior of our system that is **well defined**. In other words, all techniques that were presented may help us if we want to know what the **defined** system will be but they add absolutely no value if one wants to **design** the system having as input project requirements. From the engineering point of view, such a **design** is always the most important task. In this chapter, we will focus on this issue in details. We will present how to use the presented methods in order to perform the design process and its most important phase, the optimization stage that is crucial for every designer who wants to deliver the product that fulfills perfectly the project requirements within the shortest possible time. In the same section, the case study including complete design process will be presented. The second part, of this chapter will focus on the statistical analysis and the fabrication yield related issues that are very important from the industrial point of view when one wants to create reliable product at high yield.

3.1 Optimization

3.1.1 Ideal design and FTR methodology

Let us consider typical design path of a system as it is presented in a Fig. 3.1. As one can see, we always start with project requirements which are the base for the next steps and which have to be fulfilled. Then, the oldest engineering technique that we called the “hand-made calculations” is applied in order to estimate roughly by the means of very approximate solutions if the project is feasible. Of course, such a step depends mostly on the designer’s experience but in many cases there are many engineering approximations that allow us to perform such a step. The next stage is the heart of the design and we called it the optimization loop. It is composed of three basic substages: simulations, prototype construction and experimental verification.

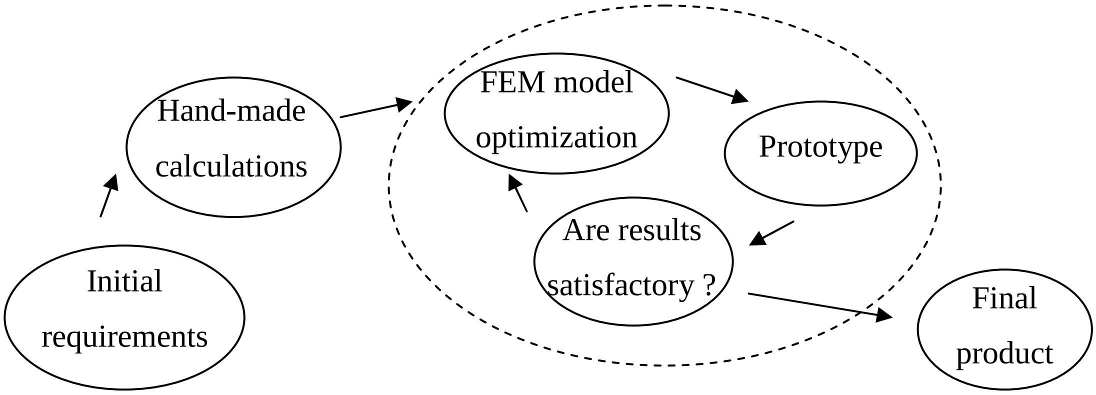

Fig. 3.1 Typical design and development process of any system.

Such a methodology was developed after introducing the CAD tools that allows us to limit the number of prototypes and avoid unjustified costs. In the reality, always after the simulation phase, a few test runs have to be performed because never, or rarely, the results obtained by simulation are accurate enough to design the correct structure at a first time. Nevertheless, the advance in simulation caused that today's models and tools are accurate at such level that in many cases the FTR idea raised. FTR – **F**irst **T**ime **R**ight methodology is a very catchy word on today's simulation market. It covers the simulations environments that allow the designer to perform all simulations in a virtual world and, as a result, design the product that will be perfect without any useless or imperfect prototype. The process, called virtual prototyping is a series of simulation that allows us to simulate the behavior of the **defined** system and then **optimize** it. In other words, not only we need the tool that will allow us to **simulate** the defined system, but also to optimize it to our needs.

If we look again at figure Fig. 3.1, we may easily remark that if one wants to decrease time-to-market, the duration of each step in the chart has to be decreased. It is quite obvious that the only step that we can really affect is the simulation process. Let us consider our particular case of the piezoresistive pressure sensor. As we mentioned, in order to design the whole system, a multidomain analysis has to be performed. The design path concerning the simulation stage should generally look as follows (Fig. 3.2).

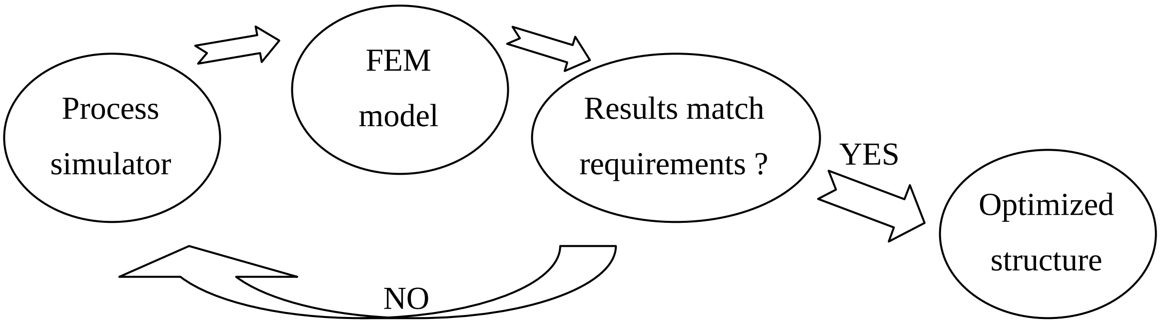

Fig. 3.2 Typical design approach of the piezoresistive sensor.

As one can see in the beginning, basing on a hand made calculations, we apply the process simulator in order to find out what doping profile we may obtain. Such a step requires the experience form the designer who, basing on the implantation tables [73] or easy approximate calculators [74], will choose which dose, energy and annealing time has to be applied in order to obtain desired profile parameters. The problem is that at such a moment we do not know how the gauge with obtained profile will work as a whole system before performing coupled multidomain FEM analysis. If we then applied the coupled analysis, at the output, we obtain the results concerning the sensor performance. At this moment one has to answer the question if the results are satisfactory and such a design is ready for fabrication or maybe it should be changed. If should, the whole procedure should be repeated so each step of the optimization includes the complicated and time consuming FEM analysis. Moreover, the optimization procedure very often requires thousands of model evaluations so even relatively short FEM simulation may lasts very long time in order to provide us with desired results. Let us then rearrange Fig. 3.2 a little bit as it is shown below (Fig. 3.3).

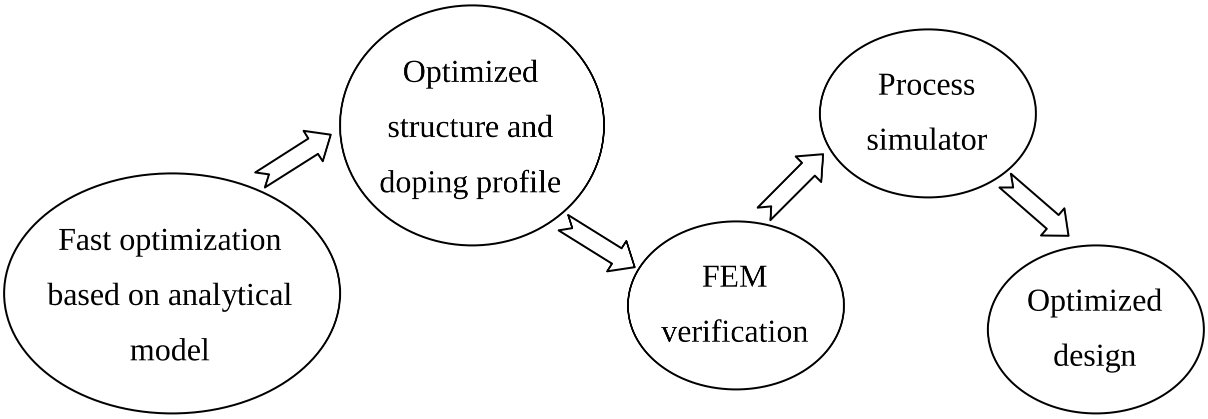

Fig. 3.3 Rearranged design path without FEM analysis in the optimization loop.

If we use our analytical model in optimization loop, at the output we obtain the sensors performances taking into account all physical phenomena that were described in the previous chapter including the influence of the doping profile. So after such a stage, we will be provided by the complete and optimized design including sensor geometry and gauge parameters that fulfills our requirements. After that, we perform only **one** FEM analysis which has to verify the design taking into account the problems that the analytical model can not deal with such as nonperfectly clamping conditions and thermomechanical stresses. The next and the last stage of the design is the analysis performed by the process simulator in order to find the desired profile what is done only **once.** As one can easily remark, such an approach may dramatically reduce the design time and thus reduce costs of the development.

Until now, we have talked about the optimization phase as a part of the process so let us now put some light on this issue.

3.1.2 Basics of the optimization

Optimization - the procedure or procedures used to make a system or design as effective or functional as possible, especially the mathematical techniques involved.

Such a definition tells us that there exist some mathematical tools that allow us perform the procedure that, at its output, provides us with the solution that fulfils our requirements. In other words, if we are capable to define our system by the mathematical function, we are able to define project constraints and then, apply the mathematical apparatus that is able to propose us the best solution to our problem.

Principles

Basically, in a mathematical sense, optimization is the operation of searching the value of an argument x for which the function $f(x)$ reaches its minimal or maximal **value** (generally algorithms search for the minimum value). The first who developed the mathematical method of optimization was Gauss with his “steepest descent” algorithm. After him, over the years a lot of mathematicians working on such a problem including: Richard Bellman, Leonid Khachian or even John von Neumann to name but a few. The basic example of the optimization is presented on Fig. 3.4, where function $f(x)$ is a quadratic function which arguments are from the set of real values. For such a case the point that we are looking for is $x=0$.

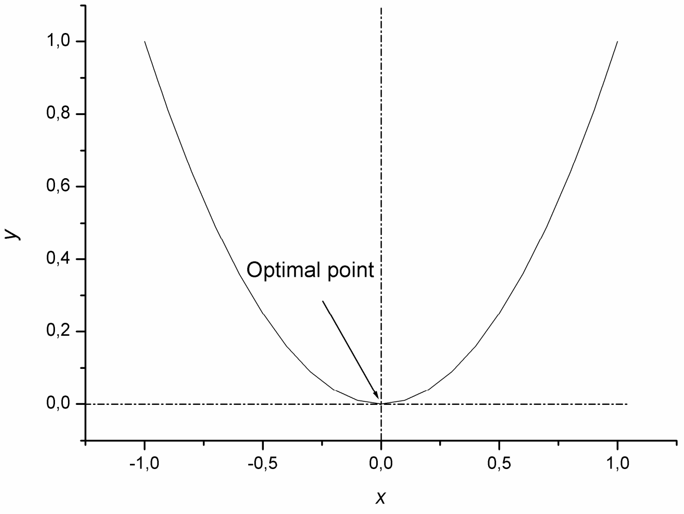

Fig. 3.4 Simple example of optimization.

Such a method where we are dealing with a function that has one output variable is called the **single-objective** optimization. Additionally, if we define a set of arguments in which we are looking for the optimal one to be, for example, the real set, our problem is called **unconstrained** because we may use every value of this set. In many engineering applications it is obviously not the case because the engineer has always to deal with the project constraints and thus, a set of function arguments has to be narrower so lower and upper borders have to be defined. For example, if we consider again the function shown at Fig. 3.4, and if we define our set of arguments to be defined as follows (3.1)

$$x \in \langle 0.5,1 \rangle \tag{3.1}$$

the solution for our optimization problem will be the argument $x=0.5$. The kind of problem that we presented is called one dimensional because f is a function of only one variable x. In the real world, we have to deal with many design variables as in the case of piezoresistive pressure system so in real applications the constrained, multidimensional optimization is the case. Moreover, in our case as we could remark in chapter 2, the function that describes the behavior of the pressure sensor is highly nonlinear. It forces us to use an optimization algorithm that deals with such a problem.

There is a lot of works presenting the optimization problems and algorithms [75, 76, 77] and we will not explain them as it is not the topic of this work. For our purposes, the most suitable and, at a time, simple algorithm called the sequential quadratic programming which was described in details in [78] is used.

In case of a nonlinear problem, the sequential (iterative) algorithm is used in order to solve quadratic subproblem [79] in each step. During each step an optimization procedure that is based on Hessian matrix, which allows us to compute the search direction is used. The problem may be easily solved in MATLAB® environment where the built-in function **fmincon** [80] is responsible to deal with such task.

3.1.3 Two-phase optimization algorithm

If we look back at our sensor model, we can consider it to be a compact model with the design parameters at its inputs and its performance at the output what may be presented as follows (Fig. 3.5).

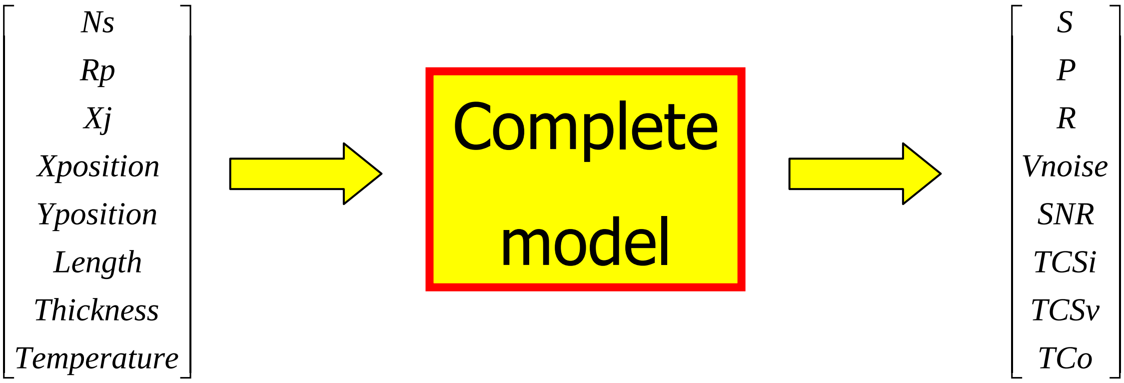

Fig. 3.5 The compact model of the piezoresistive pressure sensor.

In other words, the mathematical function that describes our sensor has 8 independent parameters including sensor geometry and gauge profile description and generates eight output values such as sensitivity, resistance and noise values with corresponding thermal drifts. Such a problem is called **multiobjective** problem and it is well known in the literature [81]. Its mutliobjectivity is the reason that there is no clear one value that has to be minimized or maximized but a set of output values that very often are **concurrent**. Such a problem has to be treated in a special way and one who presented it first was Francis Edgeworth [82] but the problem was later generalized by Vilfredo Pareto [83], so let us look closer at such a problem.

How to solve multi-objective problem

The simple multiobjective problem which deals with the maximization of only two objectives is schematically presented at Fig. 3.6.

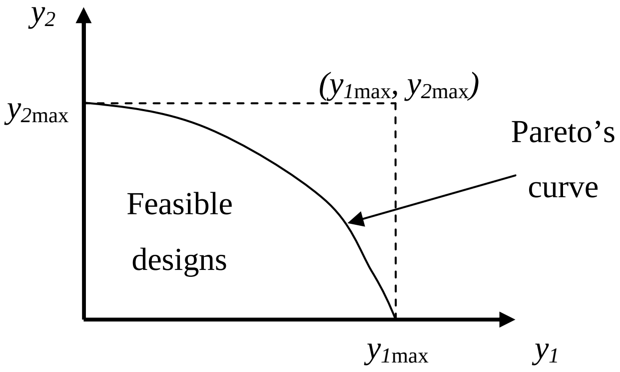

Fig. 3.6 Simple two objective function.

y_1 and y_2 are the output values of a function $f(\mathbf{v})$ where $\mathbf{v}$ is a vector of input variables and is not limited in its dimension ($\mathbf{v} = (x_1, x_2, \ldots, x_n)$). As one can see, there is a specific point at the graph $(y_{1\max}, y_{2\max})$ at which both variables have their maximal possible values $y_{1\max}$ and $y_{2\max}$ at the same time. However, very often in the real life such a solution is not possible because output variables are **concurrent**. It means that if one of them increases the second has to decrease. It creates a surface of the feasible designs (Fig. 3.6) that may be produced without broadening of project constraints. The frontier between the surfaces that covers feasible and unfeasible design is called the Pareto's curve or Pareto's surface (for three or more objective problems) and it represents best possible designs. The plural word "**designs"** is important because there is no one best design that may be proposed in such a situation and, as a result, a trade-off between the two values that has to be adjusted regarding the project requirements.

This is the moment when engineering experience often helps because one has to decide about "how much" we can decrease one output value in order to gain on the second one. Thus, it would be desired to have a tool that helps the designer to perform such a step.

Considering again the example shown at Fig. 3.6 let us imagine which design is the best one if we do not want to think about trade-offs and just find the best solution laying on the Pareto's surface. Intuitively, the design that is best compromise between the two values is the one which is the closest to the ideal design ($(y_{1\max}, y_{2\max})$ point). In other words, the multiobjective optimization of two output variables may be reduced to the single objective problem which deals with the minimization of the Euclidian distance between optimal design (y_{1opti}, y_{2opti}) and ideal design $(y_{1\max}, y_{2\max})$ (Fig. 3.7).

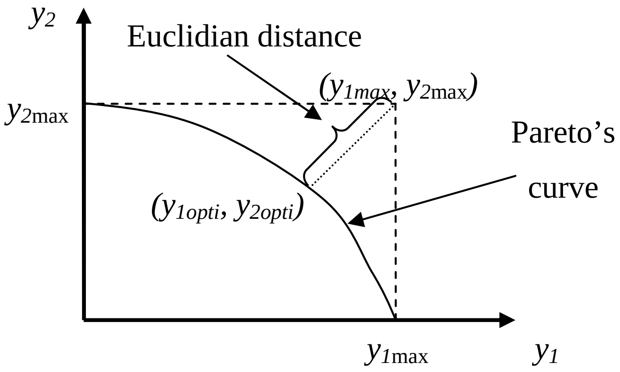

Fig. 3.7 The principle of converting multi into single objective problem.

Thus, we want to propose a two-phase optimization algorithm which reduces the multiobjective problem into the singleobjective one. The algorithm uses for both phases the sequential quadratic programming minimization algorithm.

Let us consider our pressure sensor where the function which describes the system has both eight inputs and outputs. In the first phase, for given project requirements like maximal and minimal membrane dimension as well as gauge parameters, a set of eight single objective minimizations is performed in order to find the ideal design (y_{1max}, y_{2max},… y_{8max}) that can not be built.

The second phase, as it was mentioned earlier, minimize the goal function (3.2) in order to find the optimal final design.

$$f(x_1, x_2, \dots x_8) = \sqrt{(y_{1\,max} - y_{1opti})^2 + (y_{2\,max} - y_{2opti})^2 + \dots + (y_{8\,max} - y_{8opti})^2} \tag{3.2}$$

Such an approach allows the designer to obtain the optimal set of the design variables that allows to fabricate the sensor which is optimal in the mathematical sense (best compromise between all output values).

One important remark that has to be placed here is that before any optimization, the model of our sensor has to be modified in order to have at its input and generate at its output only **normalized** values. Such an assumption is extremely important form the mathematical point of view and it has a dramatic impact on results if not properly applied. The easy example that we can imagine is again two objective optimization. If we, for an example, calculate the resistance value that usually is given in thousands of ohms (let us say 5000 Ω) and if the second variable will be the thermal coefficient of resistance which is usually given in ppm (let us say 500 ppm) the ideal design will be described by the coordinates of (5000,0.0005). It is almost obvious that our algorithm will propose us the design with the extremely high resistance value with almost random thermal coefficient of resistance because even if *TCR* will be few times greater than its optimal value it will have almost any impact on a relatively huge resistance value and thus, on the Euclidian distance when the minimization would be performed. As there are different existing methods of normalization, in our case all output and input variables are normalized using the simplest linear normalization method to the range of <0,1>.

Design tuning by introduction of weight coefficients

As we mentioned earlier, the design that is proposed by our two-phase algorithm is an optimized design but only in the mathematical sense. In real application very often the output parameters may be divided into crucial or no crucial ones form the project requirements point of view. For instance we can easily imagine the pressure sensor that has to be extremely sensible but the resistance may take any value. In other words, there are some parameters that do not have to be optimal or even are unimportant for the final product overall performance depending on an application. In such a case, the optimizer may have much more freedom during the optimization and provide us with much better values for crucial parameters (Fig. 3.8).

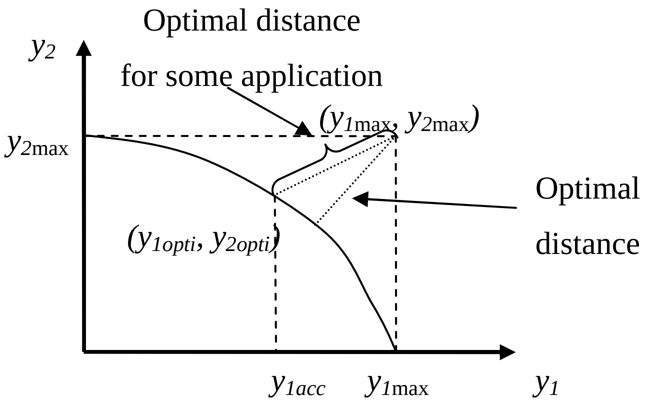

Fig. 3.8 Application driven optimization where y_1 value may be lowered to its acceptable value y_{1acc}.

Such an approach may be called the application driven optimization. It has to be said how we can “tell” that optimizer may sacrifice some parameter and how much. The answer is that the goal function (3.2) by adding so-called weight coefficients $w_1, w_2, \ldots, w_8$ that will be responsible for it. The modified goal function may then look as follows (3.3).

$$f(x_1, x_2, \ldots x_8) = \sqrt{(w_1 y_{1\,max} - y_{1opti})^2 + (w_2 y_{2\,max} - y_{2opti})^2 + \ldots + (w_8 y_{8\,max} - y_{8opti})^2} \quad (3.3)$$

Such introduced weights may tell the optimizer how important corresponding parameters are for the designer and thus give it more freedom when search for an optimal solution.

3.1.4 Optimization tool

Basing on all previous facts, we decided to extend our simulation tool by the module that will be able to handle the optimization task. The main idea was that our tool as its input should have the project constraints that are listed below (table 3.1).

Table 3.1 Design variables used in the optimizer.

Input (design) variable	Unit
Membrane length (L_m)	µm
Membrane width (w_m)	µm
Membrane thickness (t_m)	µm
Gauge length (L_g)	µm
Gauge width (L_g)	µm
Max. concentration (N_s)	at/cm^3
Implantation peak (Rp)	µm
Gauge thickness (Xj)	µm

What the designer has to do is to introduce the lower and upper bounds of each design variable in order to formulate constrained optimization problem. Then, the optimizer runs the first phase of our procedure and shows us sets of design parameters that have to be applied in order to obtain designs that are optimized for only one output value such as sensitivity or resistance value. Next, the global optimization is performed that provides us with the solution which is the trade-of between all output values. In the last part, weight coefficients may be adjusted by the designer and the global optimization phase may be performed again in order to satisfy the designer needs. The main window of our tool is presented on Fig. 3.9.

As it was in case of the simulation tool, the main screen is divided into sections. In the top left corner, project constraints for all design variables are introduced whereas in the top right corner the results section is placed. In this section, a few sets of output parameters are shown. The first five are the sets of sensor performance for single objective optimizations whereas the sixth set is the global optimal design so it is the result of the second phase. The bottom left corner is dedicated for the weight coefficients and for our purposes only four of them are possible to apply (it may be extended to all eight coefficients).

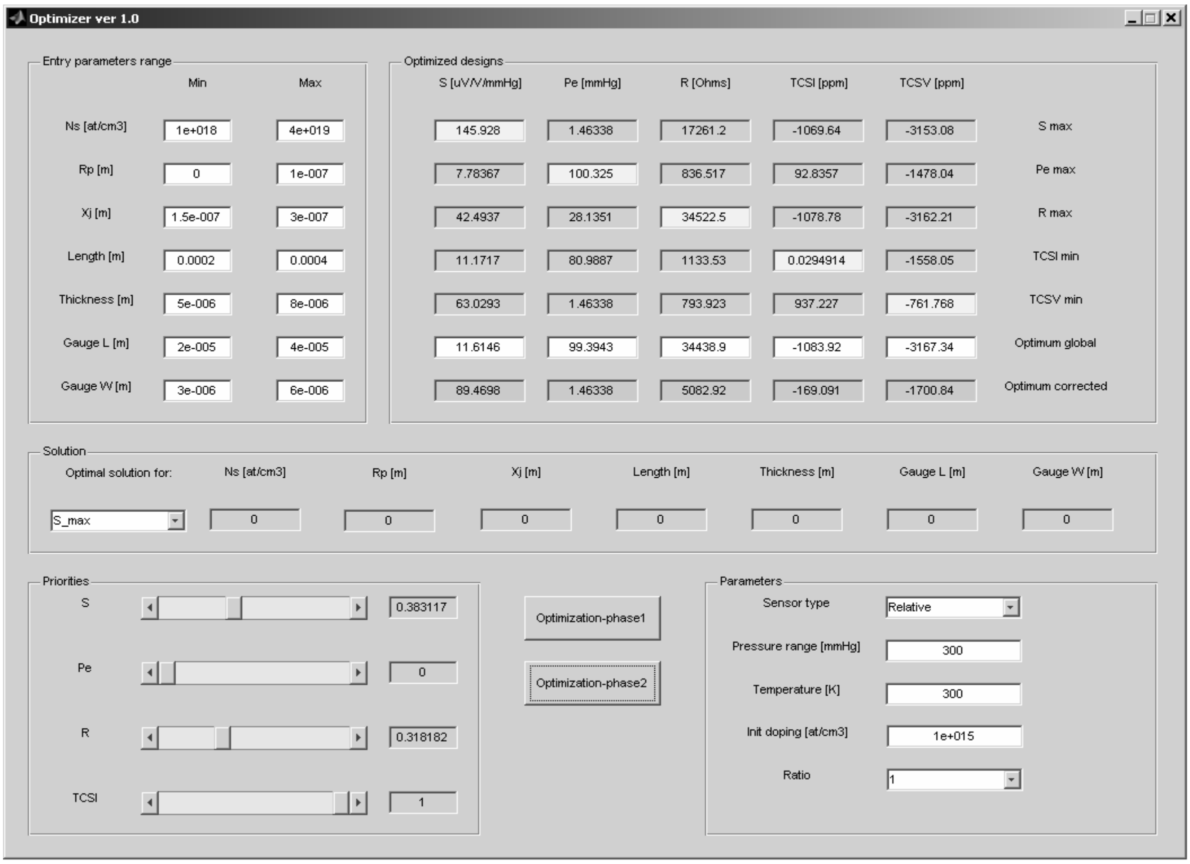

Entry parameters range

	Min	Max
Ns [at/cm3]	1e+018	4e+019
Rp [m]	0	1e-007
Xj [m]	1.5e-007	3e-007
Length [m]	0.0002	0.0004
Thickness [m]	5e-006	8e-006
Gauge L [m]	2e-005	4e-005
Gauge W [m]	3e-006	6e-006

Optimized designs

S [uV/V/mmHg]	Pe [mmHg]	R [Ohms]	TCSI [ppm]	TCSV [ppm]	
145.928	1.46338	17261.2	-1069.64	-3153.08	S max
7.78367	100.325	836.517	92.8357	-1478.04	Pe max
42.4937	28.1351	34522.5	-1078.78	-3162.21	R max
11.1717	80.9887	1133.53	0.0294914	-1558.05	TCSI min
63.0293	1.46338	793.923	937.227	-761.768	TCSV min
11.6146	99.3943	34438.9	-1083.92	-3167.34	Optimum global
89.4698	1.46338	5082.92	-169.091	-1700.84	Optimum corrected

Solution

Optimal solution for:	Ns [at/cm3]	Rp [m]	Xj [m]	Length [m]	Thickness [m]	Gauge L [m]	Gauge W [m]
S_max	0	0	0	0	0	0	0

Priorities

S	0.383117
Pe	0
R	0.318182
TCSI	1

Parameters

Sensor type	Relative
Pressure range [mmHg]	300
Temperature [K]	300
Init doping [at/cm3]	1e+015
Ratio	1

Fig. 3.9 The main window of the optimizer tool.

In the middle, the solution appears which is nothing else than a set of the design variables that has to be used in order to obtain the desired performance. In other words if the designer performs the optimization stage and adjust the design to its needs, the optimizer will "tell" him how to do that.

Let us talk about the performances of such an approach. As we mentioned earlier one simulation of the whole sensor last about 2 ms (measured by the internal MATLAB® function). For example, one single objective optimization needs about few hundreds of model evaluations (an average value tested by author for about 10 different starting points and project constraints). It means that the first phase of our algorithm may easily reach thousand or more of function evaluations. It means that the whole optimization procedure may last about 4 seconds. If we then apply the second phase of the optimization, we have to say that the whole optimization procedure lasts rather no longer than few seconds. Recall that one complete analysis in ANSYS® environment lasts about 20 seconds. If we then multiply it by one thousand it gives us two thousands minutes what is equal to **6 hours!** For only first phase of the algorithm and these are just the rough calculations. If we then estimate that each phase of adjusted optimization of the second phase needs about 100 evaluations it will add us **1** additional hour each. It is then clear that the analytical solution is much more convenient if one want to design the optimized product. Of course, as we said, at the end of our design process the detailed FEM analysis is necessary to check the influence of all phenomena that are not taken into account by the analytical model but the design time should decrease dramatically, making the piezoresistive pressure sensor design to be the quite simple procedure.

3.1.5 Case study – optimization example

Let us consider an example that allows us to follow the whole optimization procedure. We can easily imagine that our pressure sensor may be placed in many environments. For instance, we may fix the project requirements to be specified as it is shown in the table below. (Table 3.2).

Table 3.2 Exemplary project requirements.

Input (design) variable	Technological constraint
Membrane length (L_m)	< 400 µm
Membrane width (w_m)	< 400 µm
Membrane thickness (t_m)	> 5 µm
Gauge length (L_g)	< 40 µm
Gauge width (L_g)	> 3 µm
Max. concentration (N_s)	$(10^{18} \div 4{\cdot}10^{19})$ at/cm^3
Implantation peak (Rp)	< 0.1 µm
Gauge thickness (Xj)	> 0.3 µm

If we imagine that the interesting output values are the sensitivity, resistance value and thermal coefficient of sensitivity, then after performing the first step of our optimization procedure, the best possible value will be given by Table 3.3.

Table 3.3 Results of the first phase of the optimization procedure.

Output value	Best possible value
Sensitivity [µV/V/mmHg]	152
Gauge resistance [Ω]	34520
TCI_I [ppm/°C]	0.4

Then, the mathematical optimum is calculated and the following values are proposed (Table 3.4).

Table 3.4 Optimum values calculated after the second optimization phase without introducing weights.

Output value	Best possible value
Sensitivity [µV/V/mmHg]	139
Gauge resistance [Ω]	34000
TCI_I [ppm/°C]	-1012

As one can see proposed solution gives us very good value of the sensitivity and gauge resistance while the TCS_I stays at quite high level. The proposed set of design variables that is proposed is then shown in Table 3.5.

Table 3.5 Proposed set of the design variables calculated after second optimization phase.

Input (design) variable	Proposed value
Membrane length (L_m)	400 µm
Membrane width (w_m)	400 µm
Membrane thickness (t_m)	5 µm
Gauge length (L_g)	40 µm
Gauge width (L_g)	3 µm
Max. concentration (N_s)	10^{18} at/cm^3
Implantation peak (Rp)	0µm
Gauge thickness (Xj)	0.39 µm

As one may easily remarked the membrane is proposed to be as wide as possible and, at a time, as thin as possible what is quite obvious if we recall the membrane mechanics form chapter 2. The gauge was set to be as long as possible and as narrow as possible what increase the number of "squares" and thus, increases the gauge resistance. The gauge doping level is set to be minimal as it gives us the highest possible coefficient of piezoresistance and increase the resistivty. Let us then modify a little the weight coefficients by decreasing the resistance and sensitivity value which are quite high. The result of such a modification and a corresponding design variables are given in Table 3.6 and Table 3.7 respectively.

Table 3.6 Optimum values calculated after the second optimization phase after introducing weights.

Output value	Best possible value
Sensitivity [µV/V/mmHg]	99
Gauge resistance [Ω]	7534
TCI_I [ppm/°C]	-256

Table 3.7 Proposed set of the design variables calculated after second optimization phase and introduction of priority coefficients.

Input (design) variable	Proposed value
Membrane length (L_m)	400 µm
Membrane width (w_m)	400 µm
Membrane thickness (t_m)	5 µm
Gauge length (L_g)	40 µm
Gauge width (L_g)	3 µm
Max. concentration (N_s)	$1.33\cdot10^{19}$ at/cm^3
Implantation peak (Rp)	0µm
Gauge thickness (Xj)	0.46 µm

As one can see the geometry of the sensor stays at the same level while it not influences the thermal coefficient of sensitivity. The only parameters that were changed are gauge parameter as doping concentration and junction depth. Such a modification was necessary in order to be close to the optimal point from Fig. 2.21 what, as a result, lead to decrease in the sensitivity and the resistance value.

3.2 Statistical analysis

If we know how to use our developed analytical model for simulation and design of the piezoresistive pressure sensor, let us try to better match the real world. It seems to be a well known problem when the design that is perfect in virtual world does not perfectly match the real conditions. There is a lot of reasons of such a behavior starting with model imperfection that always are more or less the approximation of the real world. The other problem remains the fabrication imperfection. We can easily imagine that in order to obtain the sensor that we need, the optimizer may provide us with the membrane thickness equal to 3.456 µm but are we really able to fabricate it? The answer is no and as far as the precision of the electronic equipment increases the results are better but at the same time new techniques appears that encourage us to make smaller things so the precision is still not enough.

Considering all above mentioned fact, the real design should not only show the solution that is ideal but also should take into account the incertitude. In fact all predicted parameters of our sensor should not only be given as a value but all possible sources of errors should be taken into account and the range of output parameter should be defined. In this sub chapter we will try to show how to use the analytical model in order to perform such an analysis.

3.2.1 Why the statistical analysis?

There are different methods of calculating the influence of parameters incertitude on output function describe in literature. The most simple and the most popular is an analytical method based on the derivative calculation. If we consider the function $f(x_1,x_2,\ldots,x_n)$ where each parameter is estimated with known maximal error of Δx_1, $\Delta x_2,\ldots$, Δx_n, we may estimate the error of function f basing on the incertitude of its arguments using (3.4).

$$\Delta f\left(x_1,x_2,\ldots,x_n\right)=\frac{\partial f\left(x_1,x_2,\ldots,x_n\right)}{\partial x_1}\Delta x_1+\frac{\partial f\left(x_1,x_2,\ldots,x_n\right)}{\partial x_2}\Delta x_2+\ldots+\frac{\partial f\left(x_1,x_2,\ldots,x_n\right)}{\partial x_n}\Delta x_n \quad (3.4)$$

Such a method may provide us with the sensitivity of the output value for each parameter and also with the worst case calculations if we know what the maximum incertitude for each parameter is. Unfortunately, even in case of analytical models the derivative may be quite complex. Moreover, the second problem is that if we base of such an approach, we do know nothing about **the distribution** of the output value. In other words, we can easily imagine that the designed value is equal to 1 and if we calculate it using (3.4), we may obtain values in range of <0.5;1.5> but what about distribution? Maybe 99% of our values will be in the range of <0.99;1.01> what is great and maybe contrarily only 1% of values is in the range of <0.6;1.4> what may be catastrophic. In such a case it would be desirable to know the exact distribution of our values.

If one wants to know what the distribution of output values is, it is necessary to know the distribution of the input parameters. The distribution, in a simple definition, is a set of probabilities of occurring of certain value in the specified range. The exemplary distributions are shown in Fig. 3.10.

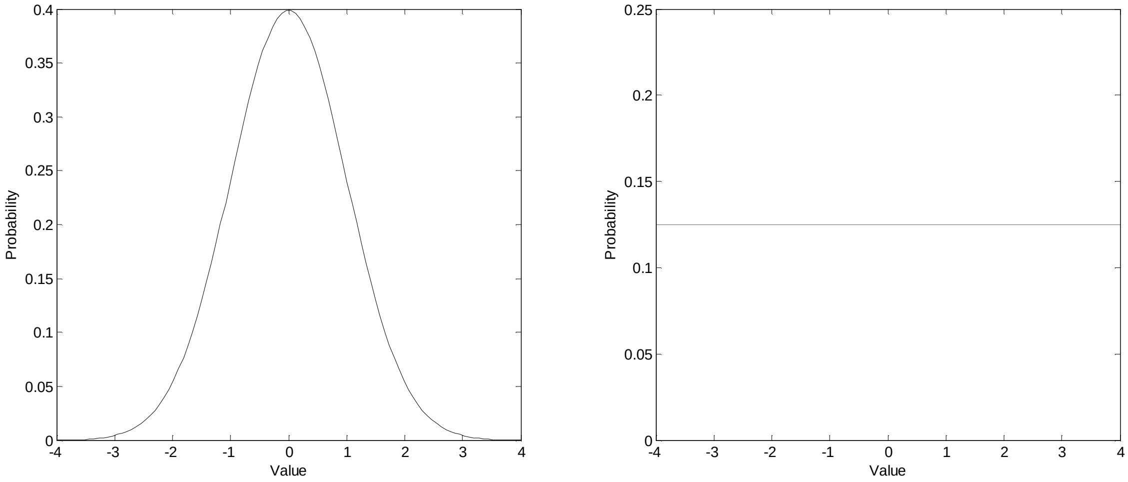

Fig. 3.10 Sample probability distributions: the Gaussian (normal - left) and uniform (right).

The Gaussian (normal) distribution is one of the oldest one and it is given by the Gauss function in the following form (3.5).

$$f(x) = \frac{1}{\sigma\sqrt{2\pi}} \exp\left(\frac{-(x-M)^2}{2\sigma^2} \right) \tag{3.5}$$

Where *M* is the mean or the expected value and *σ* is a standard deviation value that tells us about the spread. The problem is that if we even know the distribution of the input variables it is quite tedious to use (3.4) in order to find the distribution of our output function *f*. And this is the moment when statistics comes.

Having developed the analytical model of our sensor which is very rapid, we may easily imagine that we can perform many simulations in a very short time. Such a feature enables us to perform the statistical analysis. Basically, for a given set of entry variables generated by the optimizer for our design, we generate multiple input sets. In each set the design variable value is generated according to the probability distribution that is set by taking into account different incertitude sources. Then, for each generated vector an output value is derived so as a result, after such an analysis, **distributions** of sensor performances are given.

Of course, the main problem is how many analyses we should perform. Is one thousand trials enough or maybe it is far too much? In order to answer that question we propose to use some criteria that tell to the program when to stop. In fact our method is an example of the **adaptive** approach where the algorithm checks the conditions and stops when they are fulfilled. In our approach we monitor one parameter that describes the spread of values – the standard deviation. We then set criteria that if such a value converges (for an example next calculated value is not higher or lower than 10% of the mean value) the algorithm is stopped. On an example, the **normalized** standard deviation value graph in the function of number of trials is shown (Fig. 3.11).

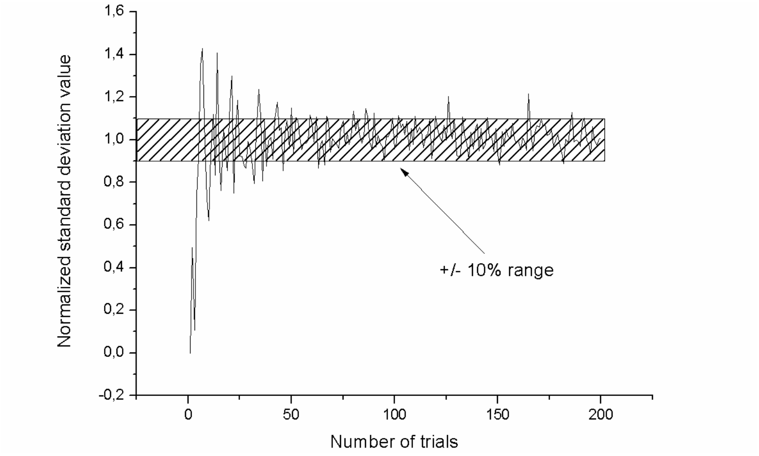

Fig. 3.11 The standard deviation value in function of the number of trials.

We may observe that in such a particular case the number of iterations that are used is limited to about 180. Such an approach may reduce the computation time dramatically and assures us that the results are valid. Of course we may tighten the convergence range to, for example, 1% what will result in increase of the computation time but it has to be emphasized that even for five hundreds trials the total computation time will not be longer than a few seconds.

3.2.2 Process characterization

As we said earlier, in order to perform the statistical analysis, the distributions of input values have to be known. The sources of incertitude may be different but generally they have two origins: equipment imperfection and human errors. In the next two short subsections we will try to give some overview of the problem.

Equipment incertitude

It has to be emphasized that all facts presented here are **indicative** and should be adjusted for particular process and fabrication equipment. Each technological step may be performed in many ways using different machines, so everybody planning to use presented statistical analysis are obliged to characterize it in order to draw the correct conclusions.

Let us start with the material that should be processed. If we are talking about the pressure sensor, the most important part of the system is the micromachined membrane. There are many techniques that allow fabricating such a structure starting with etching techniques like KOH etching or dry DRIE etch. In our approach we use the SOI wafers with predefined device layer thickness and after that we use the box oxide layer as the etch stopper.

Nevertheless the products that exist on the market are also imperfect. If we use for example a 5 µm thick SOI layer its thickness will be given by the wafer vendor with some incertitude (for example ±0.5 µm what is a standard value. It would be then desired to know the distribution of the thickness. For that case we performed the statistical analysis of the ten SOI wafer with such a specification basing on a seven-point standard measurement technique. The histogram of the wafer thickness is given in Fig. 3.12. The mean thickness is estimated to be about 5.1 µm with standard deviation of 0.18 µm. Talking about geometry, it is important to know what the precision of processes that are performed in the particular cleanroom equipment is. Some data may be gathered form the equipment datasheet like the photolithography incertitude but the other have to be characterized in the field by the machine operator as it was mentioned earlier.

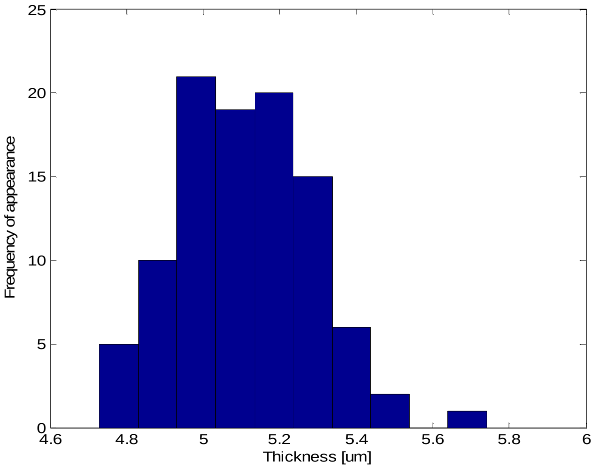

Fig. 3.12 The thickness distribution of SOI wafer with nominal thickness of 5 µm.

Human errors

In fact, the process that has very high impact on the final product is the photolithography as it is responsible for the creation of any shape. The problem is that each machine has its particular mechanism of the alignment and thus a specified error. There is, however another important aspect – the human error. We can easily imagine the simple alignment marks that are used during alignment stage as it is shown below (Fig. 3.13).

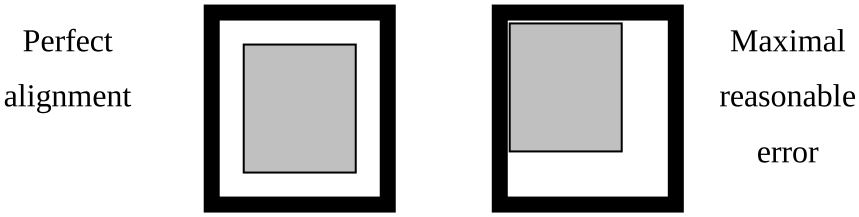

Fig. 3.13 Sample alignment marks.

On the left handed side we can see example of the perfect alignment which is rarely obtained. Very often some shift form the final position occurs but nevertheless, the maximal reasonable error that may be done by the user is shown on the right handed side of an image. Taking into account the fact that we will always try to achieve the perfect results, we may conclude that the distribution of the alignment errors may be described by the normal distribution where almost all values will be within the range shown on the right. If we look at the Gaussian distribution we can easily remark that almost all (99.9%) of values are grouped in range of $EX \pm 3\sigma$ where EX is an expected value and σ is the standard deviation.

Similar procedure may be performed for photoresist development phase or etching process and for all input values the incertitude has to be defined. For our case (basing on the experience of the operators, the following values were used (Table 2.1).

Table 3.8 The incertitude value for each of the designed variable.

Input (design) variable	Maximal error
Membrane length (L_m)	± 2 μm
Membrane width (w_m)	± 2 μm
Membrane thickness (t_m)	± 0.5 μm
Gauge length (L_g)	± 0.5 μm
Gauge width (L_g)	± 0.5 μm
Max. concentration (N_s)	± 2 %
Implantation peak (Rp)	± 5%
Gauge thickness (Xj)	± 5%

The difference in the incertitude of the membrane lateral and the gauge dimensions is that gauges are fabricated by the ion implantation through the screening oxide layer and their dimensions are defined by the holes in the photoresist. The membrane formation process, however, includes the etching stage that introduces overetching effects. Implantation errors are totally based on the data gathered at our laboratory and will vary in other labs. In our tool, the distribution of the input variable may be easily introduced as the analytical equation and changed quickly to any distribution that is possible to describe analytically. Taking into account that we are dealing with the real, physical processes where incertitude maybe introduced by many factors described earlier, for test analyses we choose that all input variables have the Gaussian distribution.

3.2.3 Data analysis

Having defined distributions of all input parameters we may perform the analysis. The main point is that we can perform it but the more important thing is to how interpret the data.

3.2.3.1 How to interpret data?

Let us imagine that we performed the analysis with 200 trials which at the end provided us with the sensitivity histogram as it is shown in Fig. 3.14. The mean value is estimated to be about 55.5 µV/V/mmHg with standard deviation of 0.97.

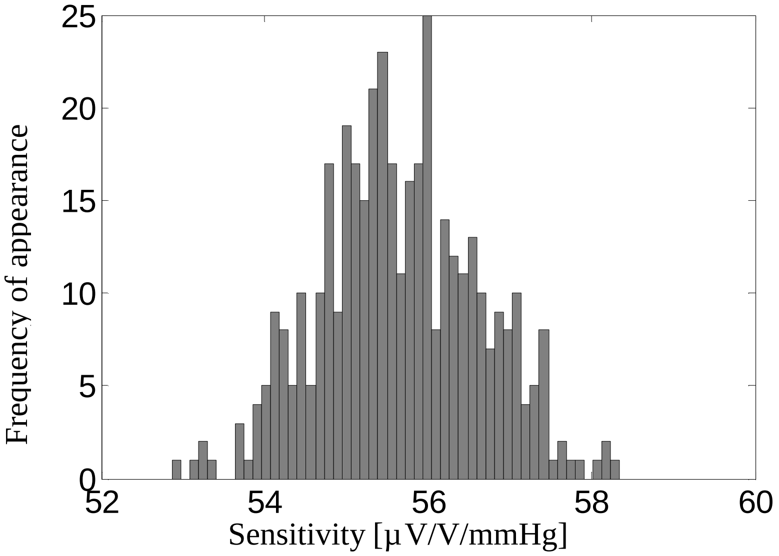

Fig. 3.14 The sample histogram of the sensitivity value.

What can be concluded from such a histogram? Firstly, we are able to calculate the expected value that will be the most likely value to appear. Then, the most important, the probability of fabricating the sensor that will be characterized with the sensitivity value from defined range may be calculated. The last information is crucial form the industrial point of view because if we imagine that project requirements of our sensor define the minimum sensitivity value to, for example, 54, we may then say approximately how many sensors that have better or equal parameters will be fabricated.

In other words we may try to estimate the production yield of our sensor. In fact there are some advanced approaches used for the yield prediction [84] which gives a good results basing on data provided by IC fabricants. They are optimized for integrated circuits and deal with specific problems which are not the case in a relatively simple process as we are using. Therefore our approach is designed to be simple and easy to use, but as we said, it has to be based on particular cleanroom equipment data.

Going further, by changing only one entry parameter incertitude while keeping other ones at unchanged level, we are able to compute which design variable has the highest impact on our design. In other words, after the design and optimization stage we may try to identify the parameter of “high risk” and try to focus on technological process steps that are the most critical one or modify our design. Moreover, such an analysis may provide us not only with the influence on the output value but may also tell us about the distribution of an output value. The exemplary result of such an analysis is presented below (Fig. 3.15).

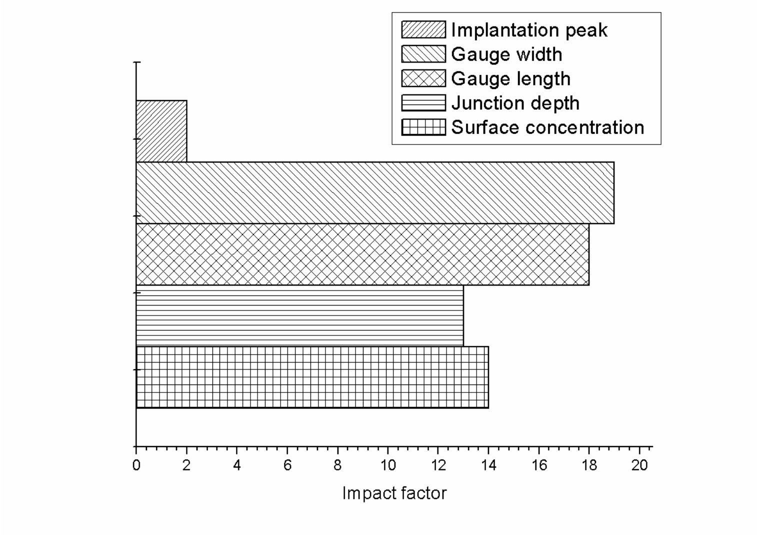

Fig. 3.15 Exemplary result of the sensitivity analysis.

One may easily remarked that the parameters that have the highest impact on the resistivity value are the gauge lateral dimensions and implantation parameters excluding the implantation range that may be neglected.

3.2.4 Offset prediction

If we look again at the equation that describes the change of the output voltage (2.24), we may notice that in case when there is no pressure applied (so no resistance change ΔR_i occurs), the output voltage of the bridge should be equal to zero.

Nevertheless, due to the process incertitude, such a case occurs only if all four resistors that form the Wheatstone bridge are identical and all interconnections are also. If they are not, some voltage signal appears at the output of the sensor under zero differential pressure applied; such a voltage is called the offset value. Let us present what is the graphical representation of the offset (Fig. 3.16) considering that the sensor response is linear.

Such a voltage is highly unwanted as it can drastically influence the dynamic range of the sensor. Thus, it would be desired to know it and here we may use our approach which may take into account all parameters that may cause the difference between each resistor. The problem simplifies as we treat that the distance between structures is small so we may considered that, for example, the annealing time and temperature as well as local variation of the screening oxide thickness are the same for each gauge.

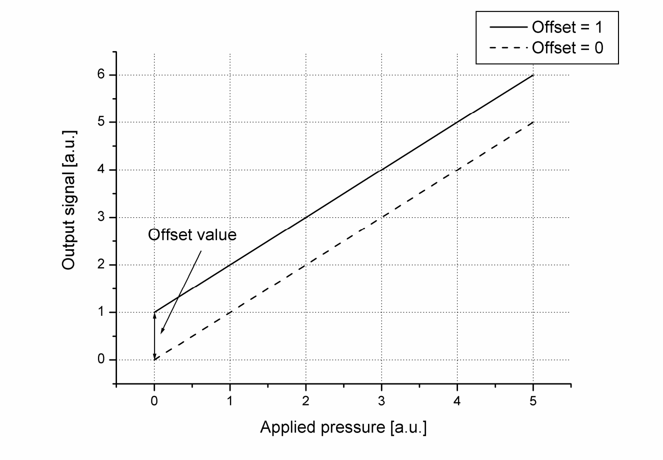

Fig. 3.16 Graphical representation of the offset voltage.

It may lead us to the conclusion that only the geometry related issues may affect the resistance values and thus, if we provide the data about the incertitude of geometry reproduction we may try to predict the offset value.

3.2.5 Statistical design tool

Consequently we decided to create the computer program that will allow the designer to perform the full statistical analysis. The main window of our tool is presented below (Fig. 3.17).

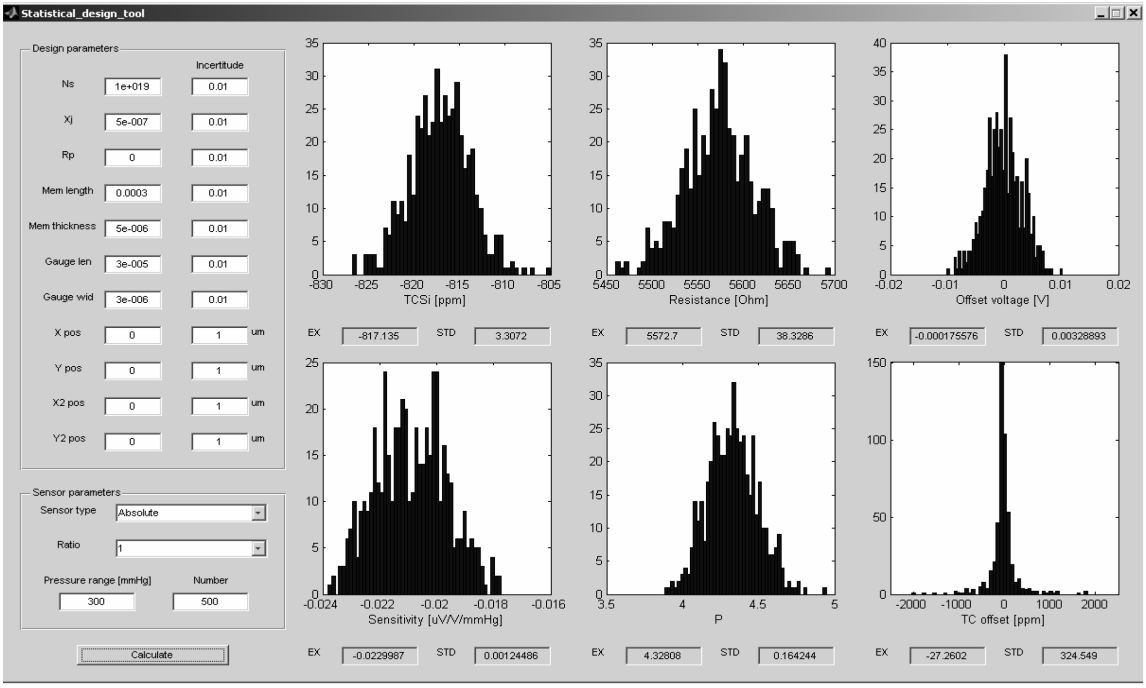
Statistical_design_tool

Design parameters

		Incertitude	
Ns	1e+019	0.01	
Xj	5e-007	0.01	
Rp	0	0.01	
Mem length	0.0003	0.01	
Mem thickness	5e-006	0.01	
Gauge len	3e-005	0.01	
Gauge wid	3e-006	0.01	
X pos	0	1	um
Y pos	0	1	um
X2 pos	0	1	um
Y2 pos	0	1	um

Sensor parameters

Sensor type: Absolute

Ratio: 1

Pressure range [mmHg]: 300

Number: 500

	EX	STD
TCSi [ppm]	-817.135	3.3072
Resistance [Ohm]	5572.7	38.3286
Offset voltage [V]	-0.000175576	0.00328893
Sensitivity [uV/V/mmHg]	-0.0229987	0.00124486
P	4.32808	0.164244
TC offset [ppm]	-27.2602	324.549

Fig. 3.17 The main window of the statistical tool.

As one can see the left section is dedicated to introduce the design that we want to analyze and define the incertitude for each parameter. The right section contains six windows that provide us with the histograms of the desired output parameters. Each histogram is characterized by the two fundamental values: expected value EX and standard deviation STD. If one wants to approximate the probability P of the occurrence of the value form the specific range, it is necessary to calculate it by using the simple formula (3.6).

$$P = \frac{N_r}{N_t} \tag{3.6}$$

Where N_r is the number of values that are in the specific range while N_t is the total number of trials. If someone, however, wants to roughly estimate the probability P basing only on the expected value EX and standard deviation σ, it is possible to use the Chebyshev's inequality [85] (3.7) where the k parameter is a natural number bigger than one.

$$\underset{k>1}{\forall}, P\left(x \in \left(EX - k\sigma; EX + k\sigma\right)\right) > 1 - \frac{1}{k^2} \tag{3.7}$$

To summarize, such an approach may be applied if one wants to have an overview on the potential sensor characteristics before the fabrication step but the price that have to be paid is the equipment characterization that has to be made a priori.

3.3 Conclusions

In this chapter, the previously developed analytical model was used to create two design tools. The first one, needless to say the most important one, is the optimizer. It uses an approach based on a two phase single objective optimization approach in order to solve multiobjective problem. It uses the standard sequential quadratic programming algorithm implemented in MATLAB ® environment. As a results, the design that meets the project requirements may be found efficiently in a very short time.

In the second part, we showed the possible approach that uses the statistical method based on the experimental data in order to predict how the characteristics of the real sample will differ form the designed one.

It has to be emphasized that all above mentioned procedures are feasible in a traditional way of iterative FEM analysis but applying of our approach may reduce the design time by using extremely fast analytical methods. Therefore, a modified design path was proposed that uses only occasional FEM analysis.

Now, the results of simulations and calculation have to be faced with the real world so in the next chapter will focus of samples fabrication and characterization.

4 Sensor fabrication and measurements

The final part of this work will present the experimental work that has been done in order to verify all facts presented in the two first chapter because, as it was mentioned earlier, the weak point of each modeling technique are models which not always match the reality. In this chapter we will present the technological process that was used in order to fabricate the piezoresistive pressure sensor. Then, the measurement setup that was used to characterize the sensor will be presented what, as a result, will lead us to experimental results. Consequently, we will compare the results with the simulation and discuss possible sources of mismatch between them. As a supplement, we will describe the procedure and test structures that were fabricated as the result of the proper investigation of the author in order to measure experimentally the thermal coefficient of resistance in P-type silicon for different doping levels.

4.1 Technological process

The whole process was conducted at the LAAS laboratory by using own equipment for all necessary steps. The fabrication facility of the laboratory contains two basic blocs, the main cleanroom used for semiconductor processing and the packaging facility. The cleanroom has about 1500 m^2 of the surface and is divided in two zones. First one with the purity class 10000 dedicated for general processing and the second one with class 100 for the complete photolithography process (photoresist deposition, insulating and photoresist development).

4.1.1 Fabrication steps

Basically, two types of sensors were fabricated: the differential and the absolute one. Recall the second chapter and especially Fig. 2.3 we need to perform two different processes in order to do that. Generally, the absolute sensor differs from the relative in one way-the space under the membrane is closed (called the cavity) and there is a vacuum inside. Therefore in fact the process for both cases is similar excluding one important stage that will be explained. As we said earlier the core of our sensor is the membrane and as it was shown later the thickness of it is crucial if one want to fabricate the sensor with the desired (designed) parameters. In the next subsection we will focus on the membrane fabricating issue.

4.1.1.1 Membrane fabrication using SOI wafers

Over the years, many techniques were developed in order to form the silicon membrane layer. The crucial case for the membrane formation process is the control of the thickness and its uniformity. One of the simplest and oldest, but giving good results, method is the silicon wet etching with the KOH solution. Basically, because of the cubic, diamond like crystal shape of the silicon lattice, the anisotropy occurs also during the wet etching process. As the mechanical properties of the silicon differs with the orientation, also the bonds strength does. It enables us to etch silicon along some crystallographic planes more easier than along others. Thus, we can easily imagine that we may choose the wafer orientation in such a way that the result of etching will always produce the plane that is parallel to the wafer surface what may create the membrane. In practical applications we use the wafers cut in (100) plane. In such a case, the etching of masked silicon will be look as follows (Fig. 4.1).

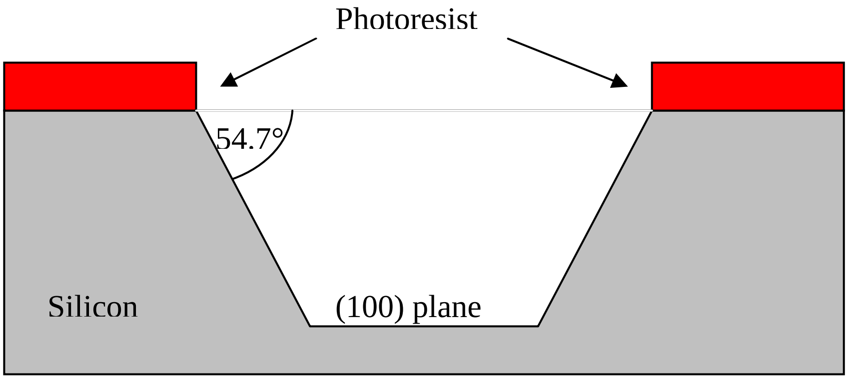

Fig. 4.1 Anisotropic KOH etch of silicon in (100) plane.

As one can remark, it enables us to create the membrane with easiness but one has to take into account the 54.7° angle during the mask design stage. Even much more complicated structures may be obtained by using this technique including multilevel structures fabricated with only one single mask [86]. The process control is quite good so we are able to etch silicon with the precisions of about 1 μm. The etch rate depends strongly on both temperature, etch rate increases with it, and on the percentage of pure KOH in the solution and the higher it is the slower etching occurs (Fig. 4.2). Moreover, the uniformity of the membrane has to be assured as we do not want to introduce any roughness throughout the etching process. According to the literature [74], if one wants to assure the flat surface after etching the solution must contains at least 30% of pure KOH and the initial roughness must be as minimum as possible.

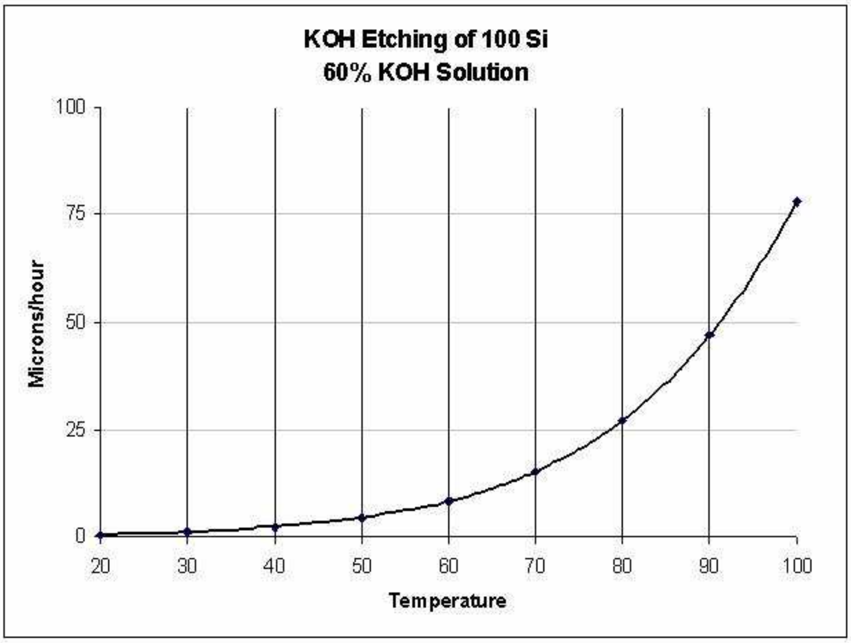

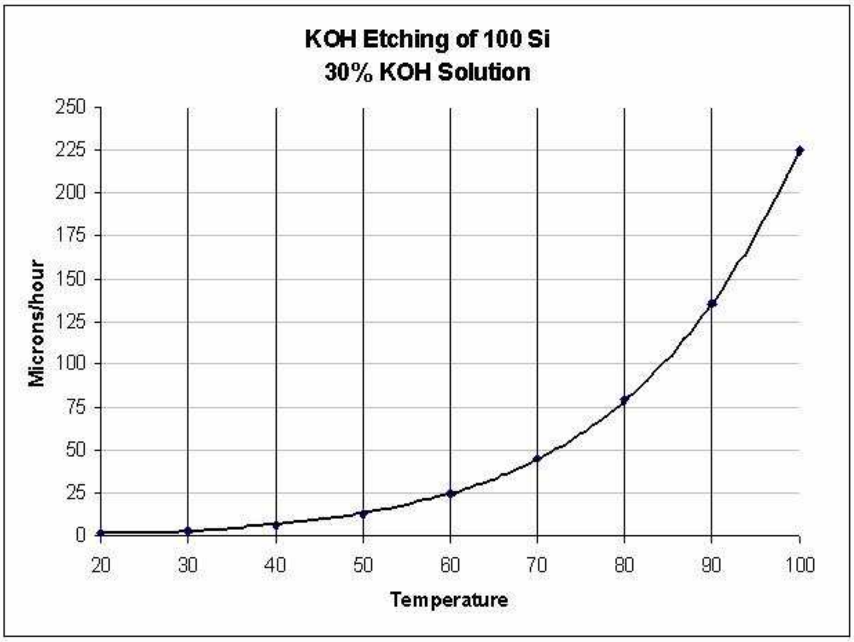

Fig. 4.2 Etching rate dependence in a function of temperature and the percentage of pure KOH in the solution [74].

The KOH method, while it is a wet etching technique it is the one of the favorite industrial method because it is possible to etch multiple wafers at a time. Moreover, it provides us with the great uniformity over the wafer area if the uniform temperature distribution is assured.
The second possible technique is the deep reactive ion etching (DRIE) of silicon. Such a technique is an example of the dry etching technique. Among different techniques one of the most known is the Bosch process [87]. The special gases (SF_6) are introduced and then the ion bombardment of the unmasked areas occurs what leads to the reaction of silicon with ions and, as a result to **isotropic** etching. After that, the passivation layer (C_4F_8) is introduced to stop the etching. Then, same procedure is repeated in a loop what, as a result, gives us the highly **anisotropic** etching profile due to the ion bombardment which occurs only at the bottom and not at the sidewalls. It is usually presented that the angle of anisotropy is in order of 88° to 92° and is better controlled when the dimension of the etched structure are smaller (in order of tents of micrometers). The DRIE despite its advantages, has also some drawbacks. Firstly, the equipment is extremely expensive in relation to the KOH etching and we may process only one wafer at a time what leads us to the obvious conclusion that the cost of manufacturing increases dramatically. Moreover, if the relatively deep and large areas has to be etched the nonuniformity problem appears over the whole wafer area.

As one can remark, both presented process may be used during the membrane formation stage but they have to be controlled in extremely precise manner in order to obtain the desired membranes thickness. As the membranes used for pressure sensors fabrication ten or more years ago reached easily 20 or 30 µm that was not a crucial problem. If we, however, want to shrink our sensors to the size of few hundreds of microns, the thinner membrane have to be fabricated with good thickness control. A milestone in that field was the introduction of the SOI wafers. Such a structure consists of a thick substrate silicon layer, a thin oxide layer and a thin silicon layer with the controlled thickness (Fig. 4.3 a)). As both KOH and DRIE process are highly selective between oxide and silicon rates etch (about 100), the thin silicon layer may be easily use as a stop etch layer for both processes (Fig. 4.3 b) d)). Once the etching arrives at the oxide interface we may stop the process and then etch the silicon dioxide by selective HF solution (Fig. 4.3 c) e)). Nevertheless we have to keep in mind that in our application we are strongly limited for the overall dimensions of the sensors. As it was shown earlier the wide of 700 µm is a limit. If we then take into account that the membrane was designed to be 300 µm wide, for our purpose we have chosen the RIE technique as it does need additional space at the backside of the wafer (Fig. 4.1).

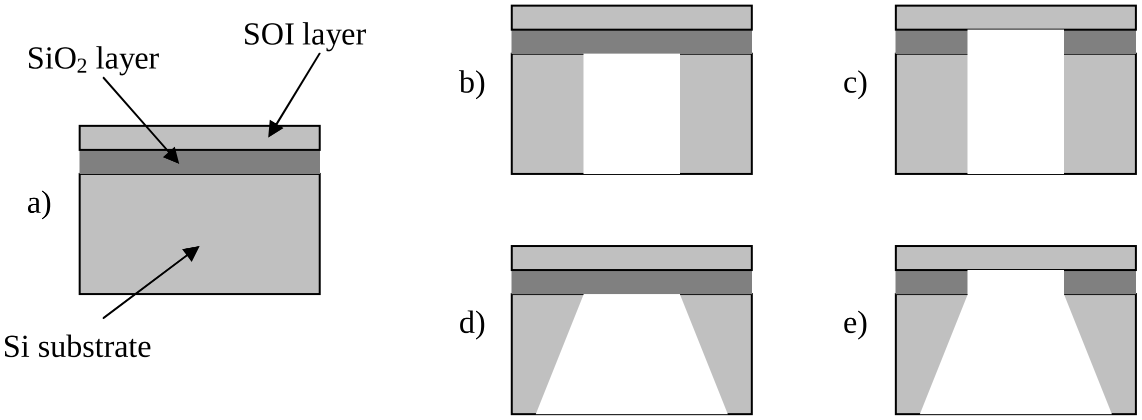

Fig. 4.3 An example of using SOI wafer a) for the membrane fabrication by DRIE etching b),c) and KOH etching d),e).

Such a technique allows us to buy the wafer with the thickness that we want and then use the standard etching process without extremely careful control as it is necessary in case of standard silicon wafers. As always, such a solution has to have some drawbacks and in this case it is the price of SOI wafers which is about 10 times higher in comparison to the standard Si wafer.

4.1.1.2 Classical MEMS process

The process that was developed in order to fabricate our sensors is a quite standard (in terms of used techniques) approach used in the MEMS fabrication. It contains eleven mask levels in order to fabricate the desired structure. Two basic cells were designed in order to test two types of the membranes – the square and the rectangular one. The set of two masks used for the fabrication are presented below (Fig. 4.4).

The membrane size is 300 µm x 300 µm for the square membrane and 300 µm x 900 µm for the rectangular one. The interconnections that are on the membrane are made of heavily doped P++ regions what reduced the thermomechanical stresses that appears when the metal is placed on the membrane (high mismatch between thermal coefficients of expansion). The overall chip size for two cases is 720 µm x 2000 µm (the maximal cell size according to the project specification).

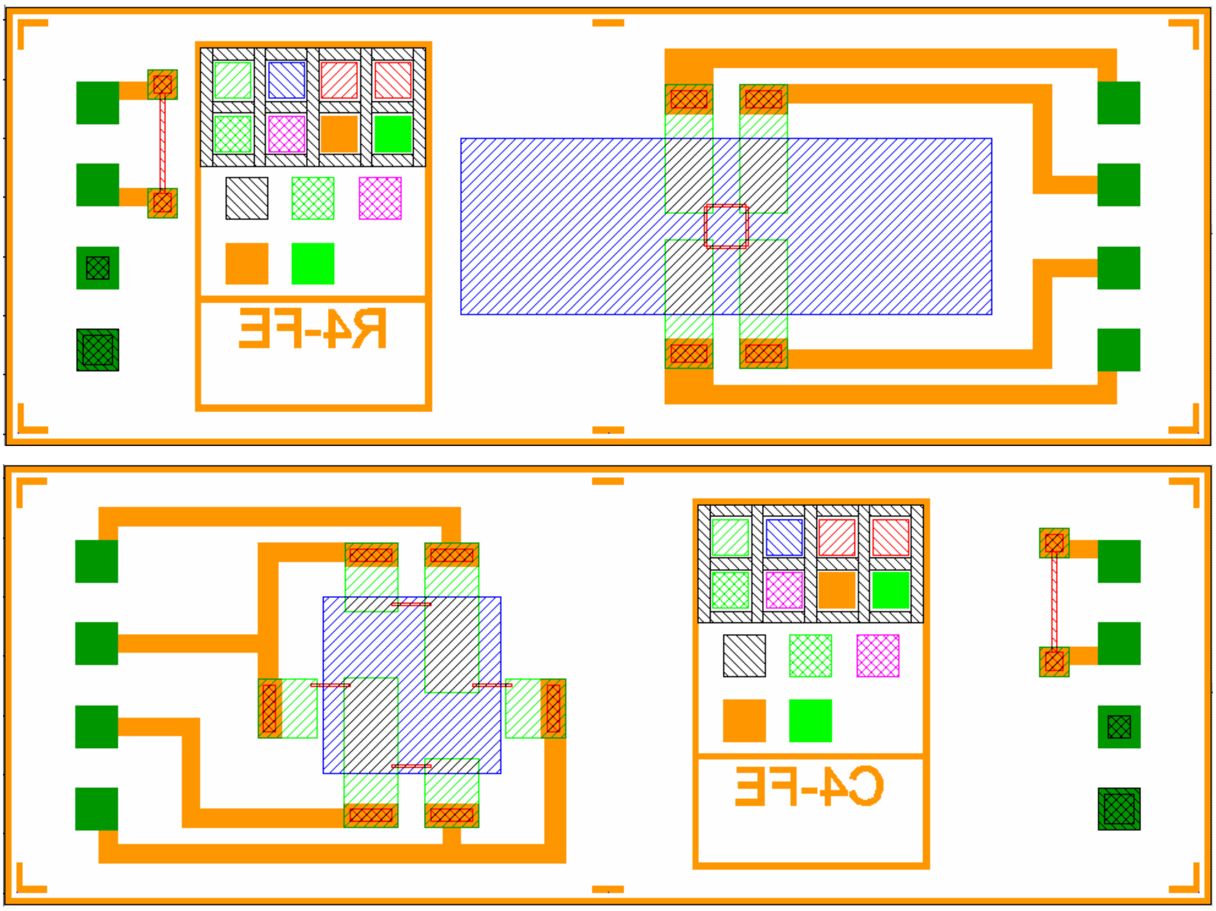

Fig. 4.4 Masks of two types of the sensor: with square (up) and rectangular (bottom) membrane.

As we said earlier, there is only one difference between relative and absolute pressure sensor but it is a fundamental one. Basically, in case of the relative pressure sensor, the "electronic part" of a system that contains all implanted structures and metallic interconnections is fabricated on a SOI wafer. Then at the end, as the last step, the membrane is created by using the DRIE process as it was shown in Fig. 4.3. If we want, however, fabricate the absolute pressure sensor, the sealed cavity has to be made. There are different techniques of sealed cavity formation but they used in common the process that, when presented, enabled us to push the limit of the MEMS devices – the wafer bonding process.

Wafer bonding – the process of connecting two wafers of the same or different material in a permanent way.

Since it was introduced twenty years ago it opened the possibilities that were not achievable. By using it, a new type of the absolute pressure sensors [88], accelerometers [89] as well as new packaging techniques emerged. There is a lot of good works in the field of wafer bonding that have been done [90] including anoding, eutectic, intermediate layer and direct wafer bonding dealing with drawbacks, advantages and features that they offered. In this work we will focus on the direct wafer bonding that was used in our process.

As we remember from chapter two, the thermomechanical stresses may easily affects the sensor performance. Thus, in our work we decided to bond two silicon wafers in order to have same thermal coefficient of expansion and thus, reduce the thermomechanical stresses. Nevertheless, we wanted to use the electrical advantage of the SOI wafer like small parasitic capacities so we decided to keep the oxide layer between the membrane and the SOI layer. Thus, the wafer bonding between Si and SiO_2 layers had to be performed. Such a bonding technique is studied in details by many authors [91]. Basically, we start with two silicon wafers where one of them is oxidized. In order to obtain good both strength the wafers should be as flat as possible and some reports [92] recommend that the total bow on four inches wafer should be less than 5 μm. Then, a special cleaning procedure is applied in order to create both surfaces hydrophilic. Such a step is necessary as it is well established that in the first phase of bonding the bonds between free Si–OH (silanol) groups occurs and such a group is responsible for the hydrophilicity of the surface. The standard solution that is used for such a purpose is a warm SC-1 (1:1:5 NH_3:H_2O_2:H_2O). Just after the cleaning procedure the wafer are put into bonding machine (in our case it was AML-AWB) and then put into intimate contact. During that process, the water molecules that are trapped between the surfaces start to create very weak bonds with the silanol groups (Fig. 4.5 a)). As we want to obtain the absolute pressure sensor, the whole process was performed at the near vacuum conditions. The force that was applied on the wafer was about 2000 N during the thirty minutes. Such a procedure generally produces relatively stronger bonds as the van der Waals forces creates bonds directly between silanol groups (Fig. 4.5 b)).

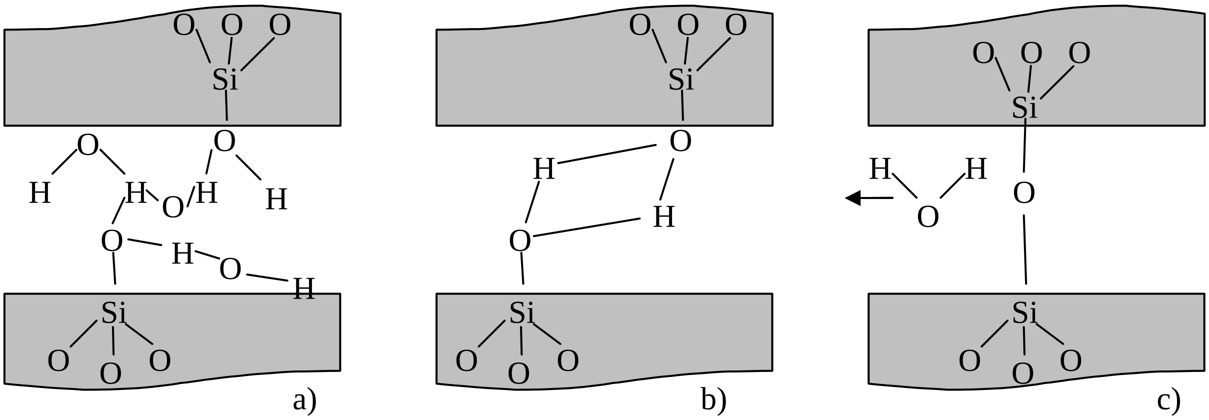

Fig. 4.5 The three basic steps of bonding: weak bonds by trapped water molecules a) stronger bond between silanol groups by van der Waals forces b) Strong bonding after high temperature annealing.

In order to obtain permanent strong bonding another process is then required - annealing stage. The high temperature annealing applied at 1100° C for 2 hours was reported [93] to be enough to obtain permanent bonds according to the reaction (4.1).

$$Si - OH + Si - OH \rightarrow Si - O - Si + H_2O \tag{4.1}$$

As a product of such a reaction not only the bond is achieved but the free water molecules appear. These molecules will then diffuse into silicon dioxide until the moment when they reach the silicon-silicon oxide interface when they react with the silicon according to (4.2).

$$Si + 2H_2O \rightarrow SiO_2 + 2H_2 \tag{4.2}$$

The problem is that the remaining hydrogen is still somewhere between and it has to dissolve into something. Fortunately it dissolves easily into SiO_2 layer and thus, such a layer has to be thick enough in order to absorb all hydrogen. If it is not, it may have some consequences as a hydrogen traps between the surfaces that will cause the so-called voids. Below (Fig. 4.6), two infrared images of bonded pairs are presented. The left one contains many voids due to the trapped particles and hydrogen between the surfaces whereas the second one may be considered as the voids free.

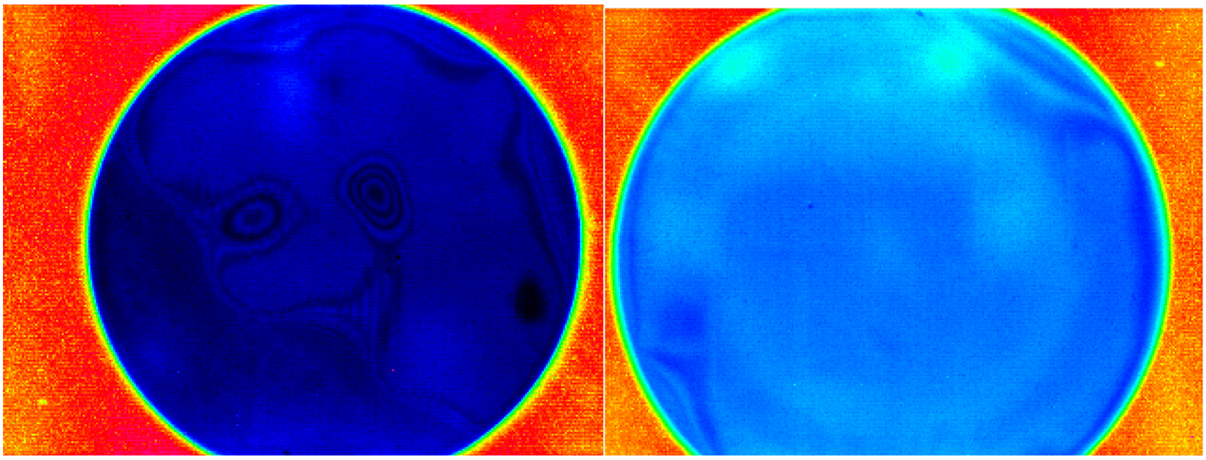

Fig. 4.6 Example of the bonded wafers pair with many (left) and almost no (right) voids.

Knowing the bonding process, we may then easily present the complete sensors fabrication process for absolute and relative pressure sensor. As most of steps are common we will present at the beginning how the process for the absolute pressure sensor arrives at the moment when it is then almost identical to the one that is used for the relative pressure sensor fabrication. The partial diagram of the process is depicted below (Fig. 4.7).

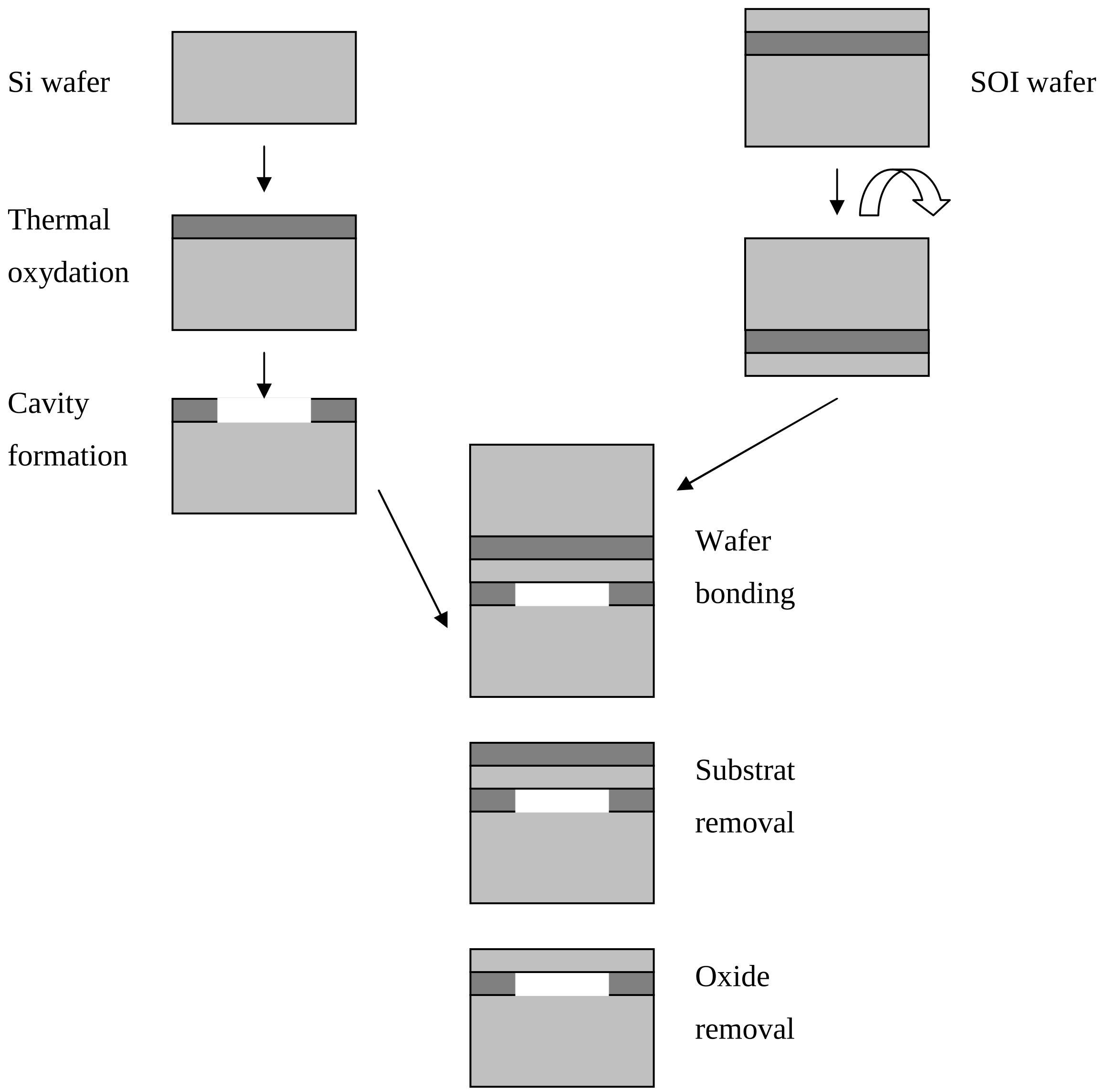

Fig. 4.7 The formation of micro cavities for the absolute pressure sensor.

The cavity formation is done by the RIE process which allows us to control the lateral membrane dimensions in comparison to wet oxide etching by HF solution which is isotropic and may easily overetch the cavity borders what results in increased membranes length and width. The substrate removal is made in the beginning by mechanical grinding to be finished by wet KOH silicon etching. It has to be finished by wet etching while the membranes with thicknesses smaller than 50-80 µm are to fragile to the mechanical grinding. Form this moment the rest of the process is identical for both type of sensors excluding the last step what will be shown at the end. The simplified process then looks as follows (Fig. 4.8).

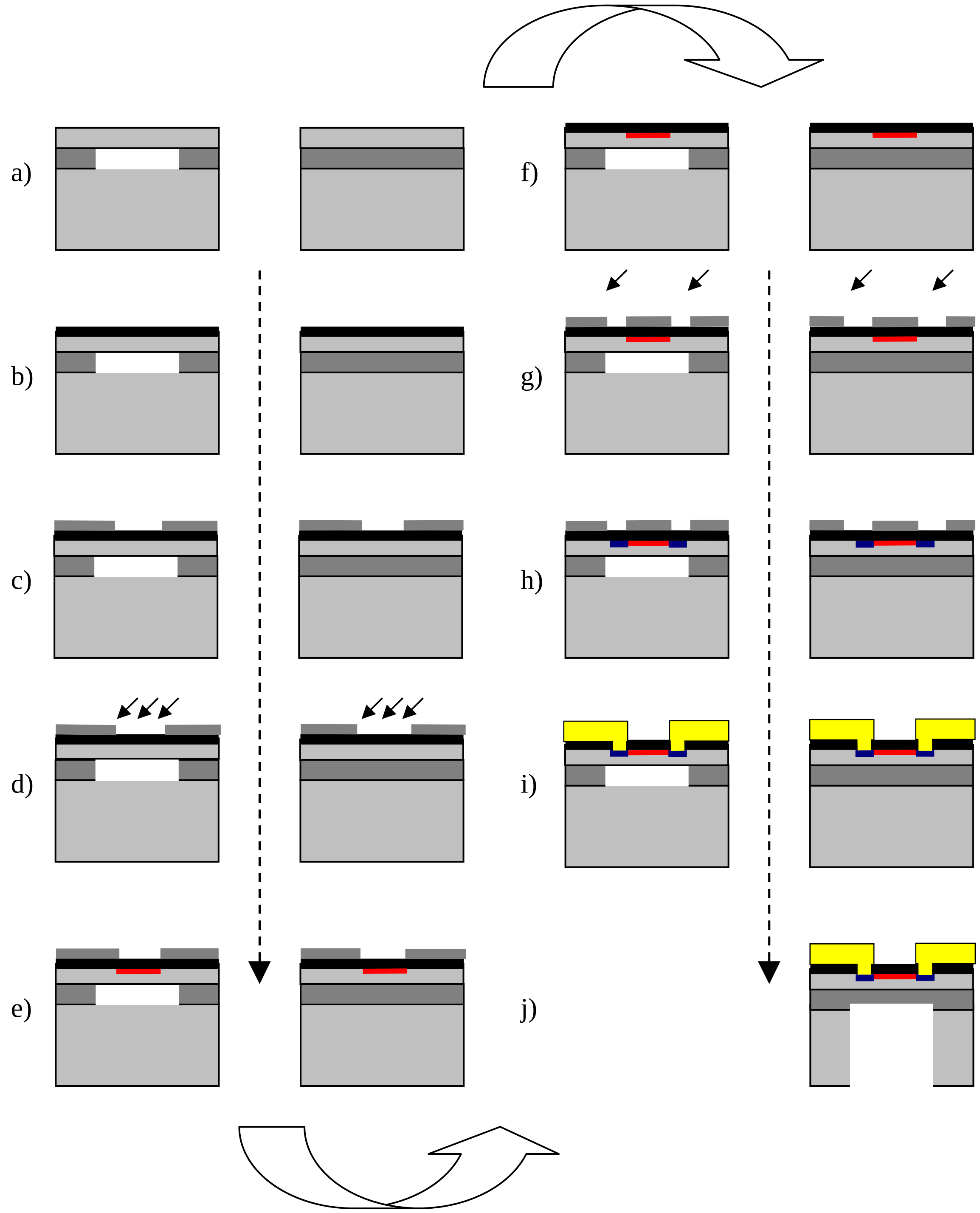

Fig. 4.8 The simplified fabrication process diagram for a differential and an absolute sensor pressure.

In the beginning, on the wafer (Fig. 4.8 a)) the thermally grown layer (400Å) of screening oxide is made (Fig. 4.8 b)). After that, the photolithography process (Fig. 4.8 c)) is used in order to prepare the wafer for first ion implantation (Fig. 4.8 d)) that will form strain gauges (Fig. 4.8 e)). Then, the photoresist is removed (Fig. 4.8 f)) and another photolitography and ion implantation process is performed (Fig. 4.8 g)) in order to fabricated heavily doped interconnections regions (Fig. 4.8 h)). The next photolithography process is finally used in order to fabricate the metallic interconnections (Fig. 4.8 i)) by the lift-off process. At this stage, the absolute pressure sensor is finished whereas the relative one does not have the membrane. Therefore, the SOI wafer is etched from the backside by the DRIE process which was described earlier.

4.2 Measurement setup

After the fabrication stage, sensors have to be characterized in order to measure precisely their performances. In fact, in case of pressure sensors such a characterization stage is not trivial because of the need of controlling the environment of the sensor and more precisely the pressure and the temperature values. Nevertheless our sensor is some kind of the electronic circuit so some tests may be done using the standard characterization tools designed for this purpose. Generally, we may divide the characterization stage into two phases: the on-wafer testing when we try to characterize all electrical sensor parameters such as the resistance value, offset value and their corresponding thermal coefficients. Secondly, we have to measure sensor response to the applied pressure and for this purpose the wafer has to be cut into single dies that are then packaged in a dedicated testing package that was designed for them. Both processes will be now shortly presented.

4.2.1 On-wafer testing

After the fabrication stage, the standard 4 inches wafer contains about 2000 test cells. Half of them are the rectangular one while rest are square. As the measurement setup, two probe stations were used. First one is a semiautomatic SUSS MICROTEC® PA200 station with tester HP4120. Such a station allows us for measurement of DC voltage and current in semiautomatic mode. It means, that the cartography of cells may be programmed and then the automatic measure may be performed without intervention of anybody. Moreover, such a station is equipped with the thermal chuck which allows us to control its temperature and thus perform the measurements of the thermal drifts of the offset or resistances.

The second station was CASCADE microtech® with the tester Keithley 4200 which is the cutting edge in electrical measurements at high precision. The second station was equipped in closed chamber where we can control the temperature. The chamber protects also the wafer form the external light and the electromagnetic field.

In order to get the sensor response to the applied pressure, the new equipment developed last year by SUSS microtech was used. It is called the PPM module [94] and in fact, it is an extremely precise generator of the air flow. The principle of the measurement is that if the outlet of the moving gas (the nozzle) is close enough to the surface, we may consider the pressure applied to the surface to be quasi constant. In fact the module calibrates itself by using the chuck built-in pressure sensor each time in order to know what is the outlet pressure drop in a function of the distance between the nozzle and the surface. Schematic view of such a system is presented below (Fig. 4.9).

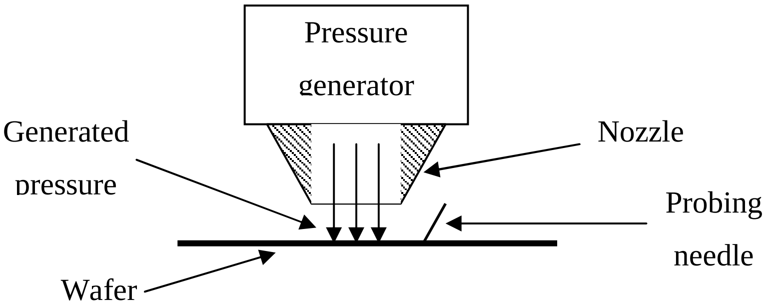

Fig. 4.9 Schematic view of the PPM module.

Such a system is of course an approximation of the real pressure generator and due to the effects of the flow at the side walls of the nozzle its precision is limited and according to datasheet is estimated to be about ± 85 mbar.

The described measurement setup allowed us to perform the electrical, temperature as well as some pressures response preliminary tests whereas the full precision was achieved with the packaged sensor which was tested in a fully controlled atmosphere.

4.2.2 Packaged sensor

4.2.2.1 Temporary packaging

The temporary packaging of the sensor consists of a small PCB board on which it was mounted by using the silicone. After that, using the micro bonding technique, the contact plots were bonded to the PCB gold layer in order to be connected with the RS-232 port which allows us to connect the electrical measurement unit. The schema of such a temporary packaging is presented on a Fig. 4.10. Such a packaging has also some drawbacks. One of them is the thermomechanical stress that comes from the silicone that joints the PCB and the silicon sensor cell. Thus, all sensitivity tests were performed in a controlled atmosphere with the temperature precision of about 0.05 °C.

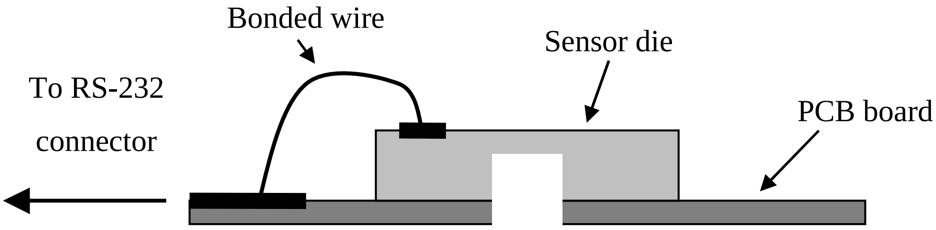

Fig. 4.10 PCB board used for the temporary packaging.

4.2.2.2 Test setup

The PCB is then mounted into a chamber made from stainless steel in order to make the atmosphere around the sensor isolated and controllable. The chamber consists of two parts which are joined together by the screws. Between them, the PCB board is mounted and to rubber joints are placed on each side of the board to achieve hermetic packaging (Fig. 4.11).

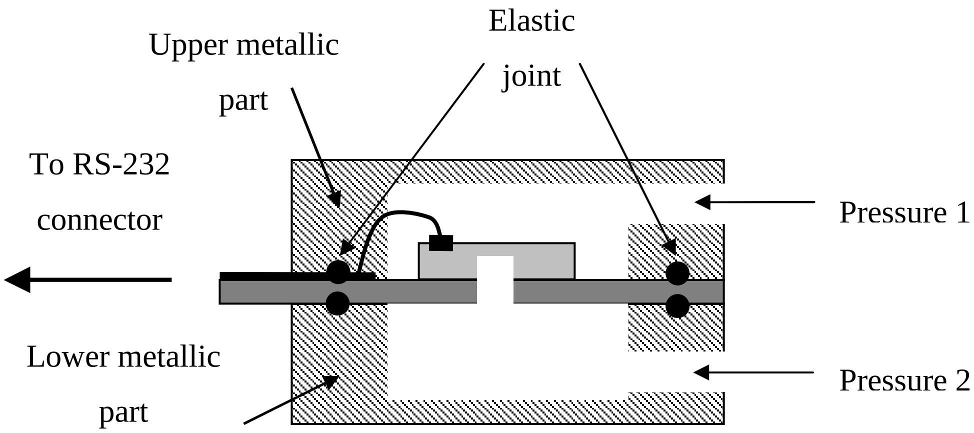

Fig. 4.11 Test setup used for the sensor characterization.

Such a solution enables us to obtain the desired pressure form both side of the membrane (important in case of the differential pressure sensor) Moreover, it gives us the possibility to put whole setup to the chamber with precisely controlled temperature and it protects the sensor from the external light and pollution. The fabricated setup is shown in Fig. 4.12.

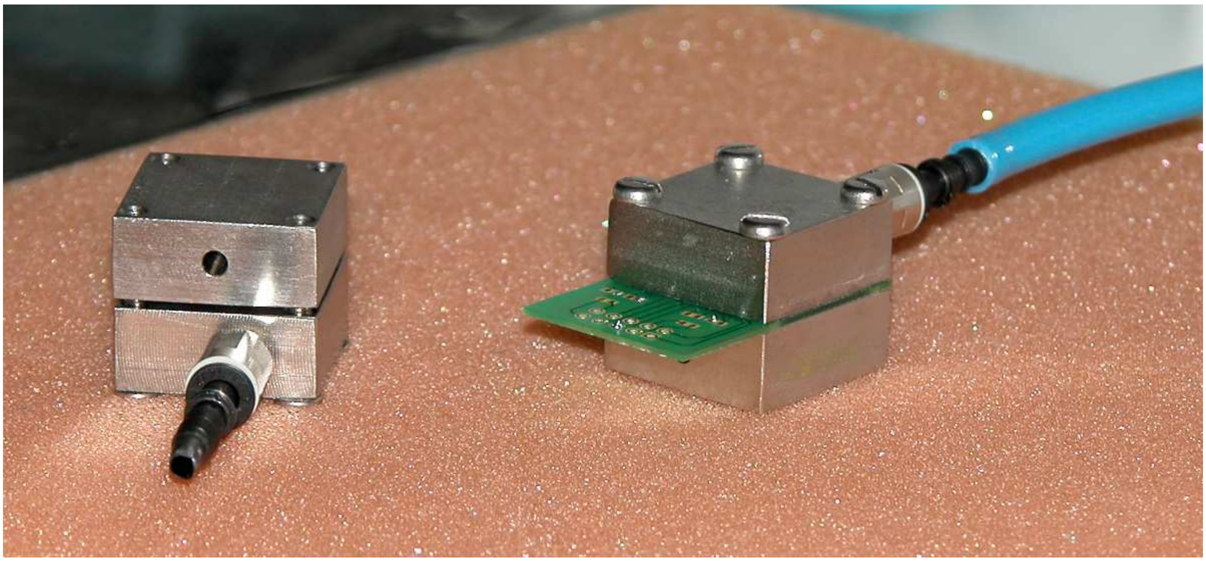

Fig. 4.12 The real view of the experimental setup.

Such tools allowed us to perform a set of tests on our samples and estimate the performance of our sensor so let us present he results of measurements in more details.

4.3 Sensor performance

As it was mentioned earlier the most important parameters that characterize the pressure sensor are its sensitivity, offset value and its thermal drifts. We have to keep in mind that according to our application, the pressure range that we would like to measure is about 0÷300 mmHg and the temperature operating range is set to 20÷40°C. The example photography of the single sensor cell with the rectangular membrane is presented below (Fig. 4.13).

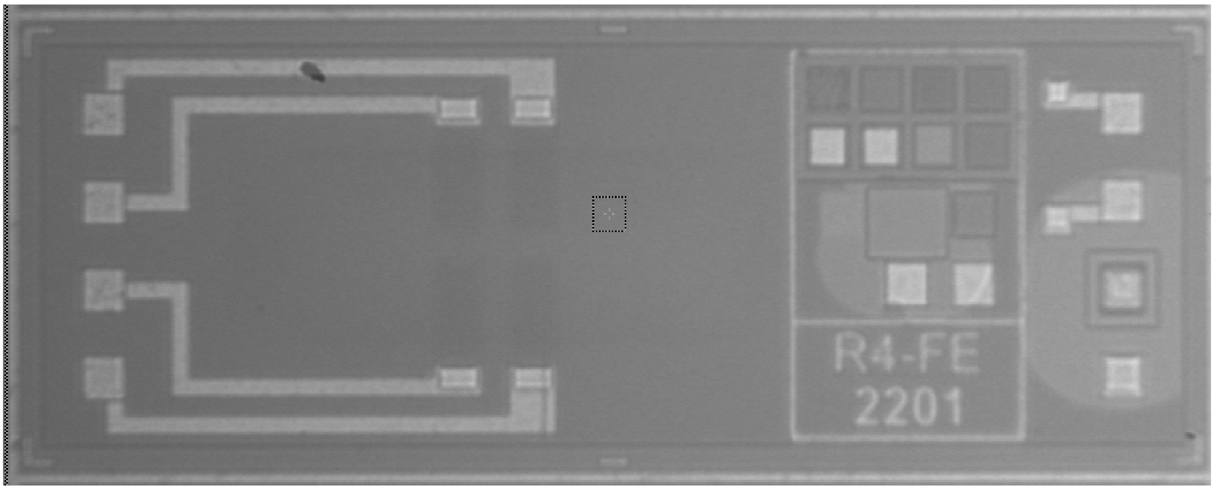

Fig. 4.13 The photography of the fabricated sensor.

4.3.1 Electrical characteristics

4.3.1.1 Sensor response to the pressure load

The differential pressure sensor was tested using the measurement chamber that was presented at Fig. 4.12. Both, square and rectangular membranes were tested by applying the differential pressure ranging from 0 to about 200 mmHg. For both sensors the sensitivity was estimated by the preliminary measurements in order to set the gain of the signal conditioner circuit that is set to give at its output the signal varying form 0 to 3V for the full scale. In order to predict the sensitivity by our model, we have to know what is the doping profile of the fabricated gauges. Therefore, the SIMS analysis, which gives us the boron concentration in the function of depth, was performed. It has to be remarked that for an absolute and differential pressure sensor two different doping profiles were used. We used two in order to test two different thermal coefficients of sensitivity as they are inversely proportional to the doping level (Fig. 2.16).

The result of SIMS analysis for the differential sensor is presented in Fig. 4.14 where dots represents the measurement while the approximation of such a profile is given by the dashed line.

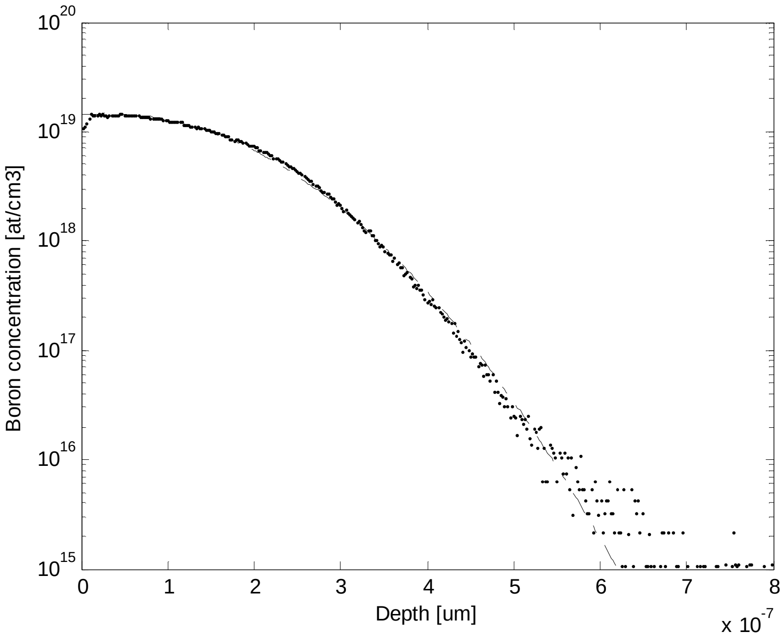

Fig. 4.14 The SIMS profile of the strain gauge used in differential pressure sensor.

For the absolute pressure sensor, the profile looks differently like it is depicted below (Fig. 4.15).

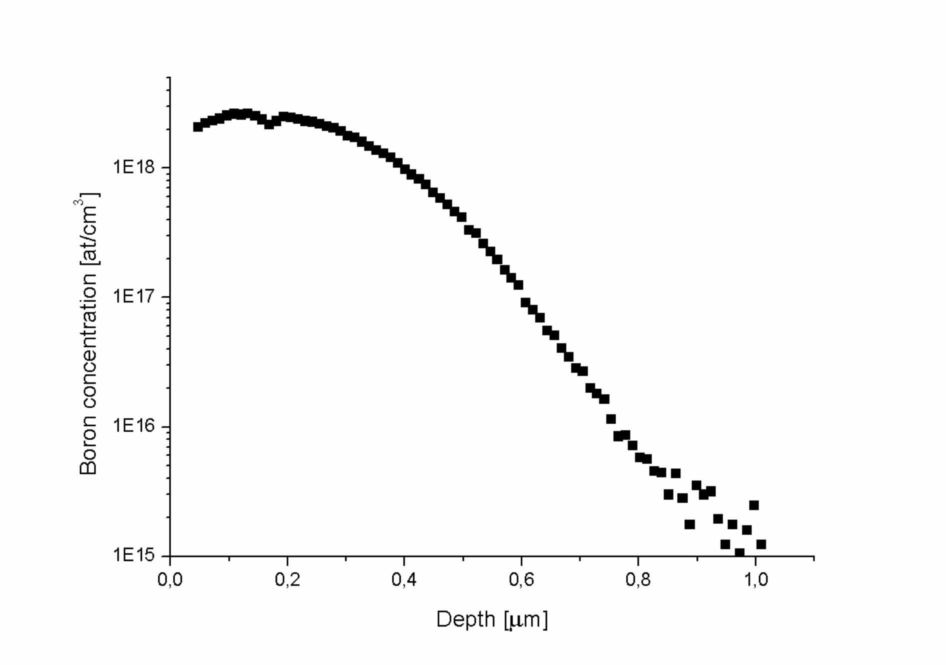

Fig. 4.15 The SIMS profile of the strain gauge used in absolute pressure sensor.

The expected sensor performance: gauge resistance and sensor response are presented in a table below (Table 4.1).

Table 4.1 The expected sensor parameters predicated by the analytical model.

Parameter	differential		absolute
	square	rectangular	square
Sheet Resistance [Ω/square]	347	347	572
Sensitivity [µV/V/mmHg]	42.4	50	52.3

All data were computed considering that the membrane thickness is **exactly equal to 5µm** and the Kanda's model was used in order to calculate the gauge sensitivity as it was explained in chapter 2.

We then measured the sensitivity of the relative sensor by using the setup presented earlier (Fig. 4.11). For a square membrane, the plot of the output voltage after the amplification is shown in Fig. 4.16 whereas for the rectangular membrane the same result is presented in Fig. 4.17.

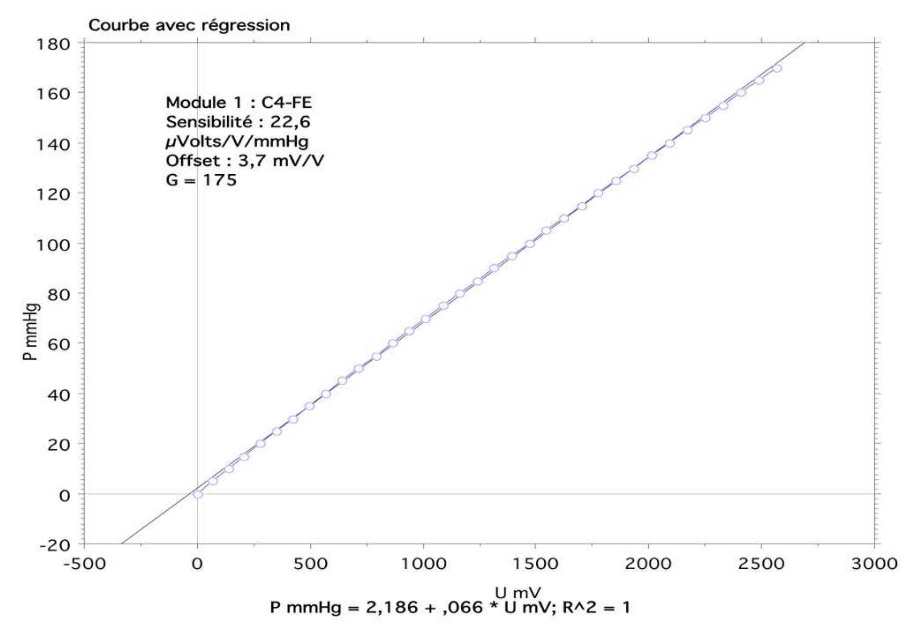

Fig. 4.16 The output voltage-applied pressure curve for the sensor with square membrane.

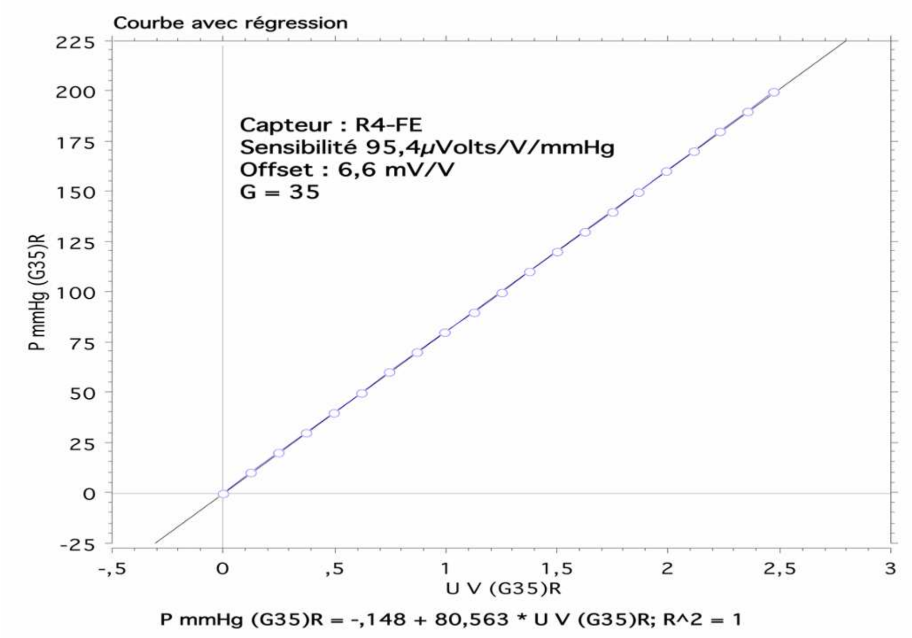

Fig. 4.17 The output voltage-applied pressure curve for the sensor with rectangular membrane.

For the absolute pressure sensor, we used the PPM module that was presented in Fig. 4.9 and tested the sensors on wafer without any amplification or conditioning circuit. The exemplary sensor response to the pressure load for the square membrane is presented in Fig. 4.18. We do not measured rectangular membranes as due to the technological difficulties all of them were not properly bonded to the substrate.

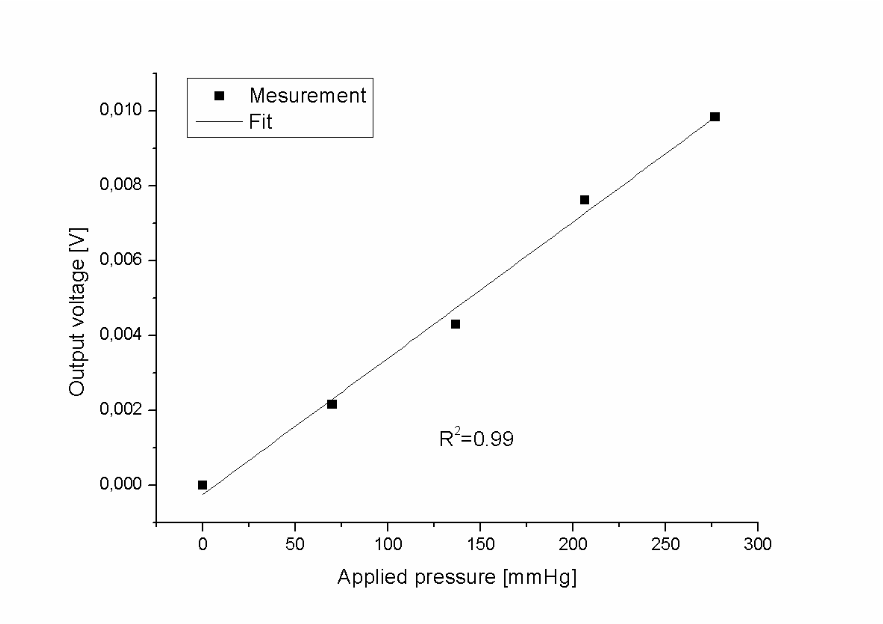

Fig. 4.18 Response of the absolute pressure obtained by using the PPM module.

As one can clearly see, responses of the sensor to the applied pressure measured by the use of controlled pressure chamber are much more linear than the one obtained by the PPM module. Such a difference may be explained by the much smaller precision of the PPM module (± 85 mbar) than the one that is offered by the pressure chamber (± 0.1 mbar). Nevertheless, for both cases the linearity is high enough to estimate the sensitivity for both cases by applying the linear theory of he piezoresistivity. The calculated sensitivity and the resistance value are presented in the Table 4.2 as well as the deviation from calculated values.

Table 4.2 Measured sensors performances and their comparison to the calculated ones.

Parameter	differential		absolute
	square	rectangular	square
Sheet Resistance [Ω/square]	360 (+3.7%)	360 (+3.7%)	584 (+2.1%)
Sensitivity [µV/V/mmHg]	22.2 (-52.1%)	95.4 (+90%)	36.1 (-19%)

If we then compare experimental results to the expected ones we may easily remark that there is an enormous mismatch between them in terms of the sensitivity value whereas for the resistance value results are correct. Thus, we decided to perform more tests in order to find out where is the reason of such a mismatch.

One of the potential reason of such a problem was the difference between the designed and the real dimension of the membrane. Therefore, we tried to estimate what is the real size of the membrane we fabricated. In case of the membrane thickness measurement, we used special test structures that were designed inside the sensor cells (Fig. 4.4) where the SOI device layer was etched until the box oxide. Then, the optical profilometer was used in order to measure the height of the etched hole and thus, the membrane thickness. Of course we consider that the SOI device layer thickness is uniform over the whole sensor area what seems to be reasonable as we consider small size of the cell. Exemplary result of such a measure is presented in Fig. 4.19. The optical profilometry may be applied because on the SOI device layer there is still the screening oxide layer which assures that the reflection coefficients inside the hole and at the surface layer are identical. Of course if one want to estimate the membrane thickness the screening oxide layer thickness of about 400Å has to be considered.

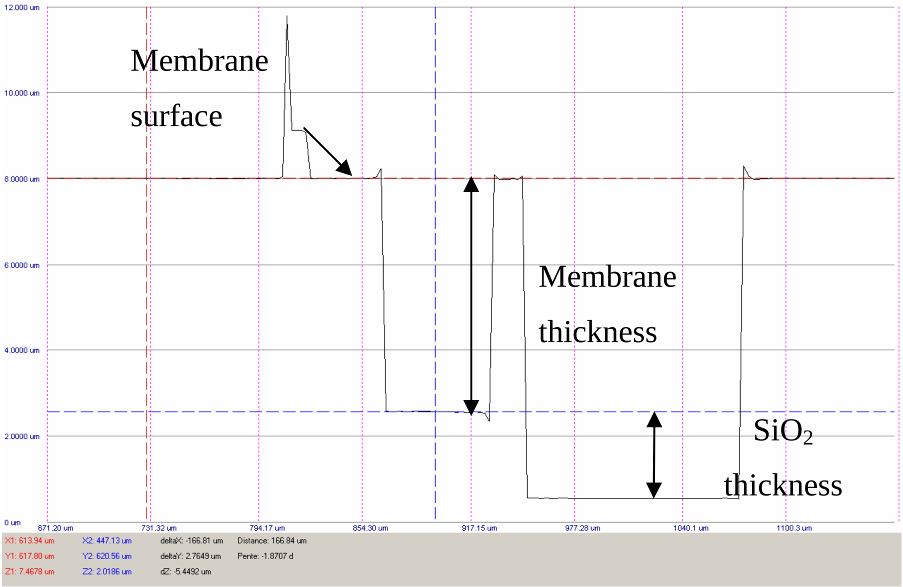

Fig. 4.19 The profile of the test structure used for the membrane thickness estimation obtained by the optical profilometer.

In order to estimate the lateral membrane dimensions we also used the optical profilemetry but we observed the deflected membranes. In case of the absolute pressure sensor it was quite simple while due to the vacuum inside the cavity the membrane was deflected at the atmospheric pressure. Moreover, for the absolute pressure sensor the membrane size was defined by the oxide etch during the cavity formation before the bonding stage (see Fig. 4.7) and the measurement taken before bonding shown that the lateral membrane dimensions were correct.

In case of the differential sensor, membranes were created by using the DRIE technique and according to some works [95], there is always some problem with keeping the etched hole vertical during the etching process, especially when dealing with relatively large structures.

We had to apply the differential pressure to our sensors and perform the measurement of the deflected membrane profile. In order to do that, we constructed a simple metallic support with a small hole with diameter of 300 µm and used the vacuum supplied to the chuck of the optical profilometer. Then, we put the sample on the support which was mounted on the profilometer chuck and applied the vacuum which caused the deflection of the membrane as it is shown on the schema (Fig. 4.20).

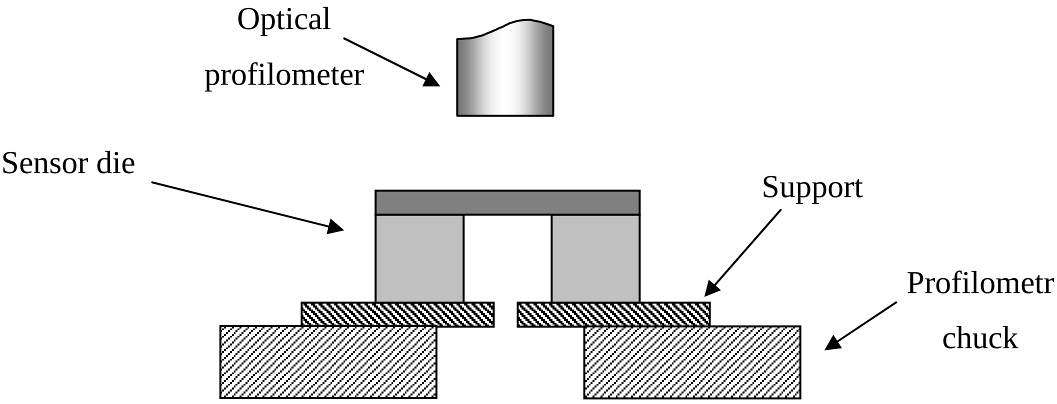

Fig. 4.20 The simplified setup that allowed us to measure the membrane deformation and thus, its lateral dimensions.

The results of such a test for both, square and rectangular membrane are shown in Fig. 4.21 and Fig. 4.22.

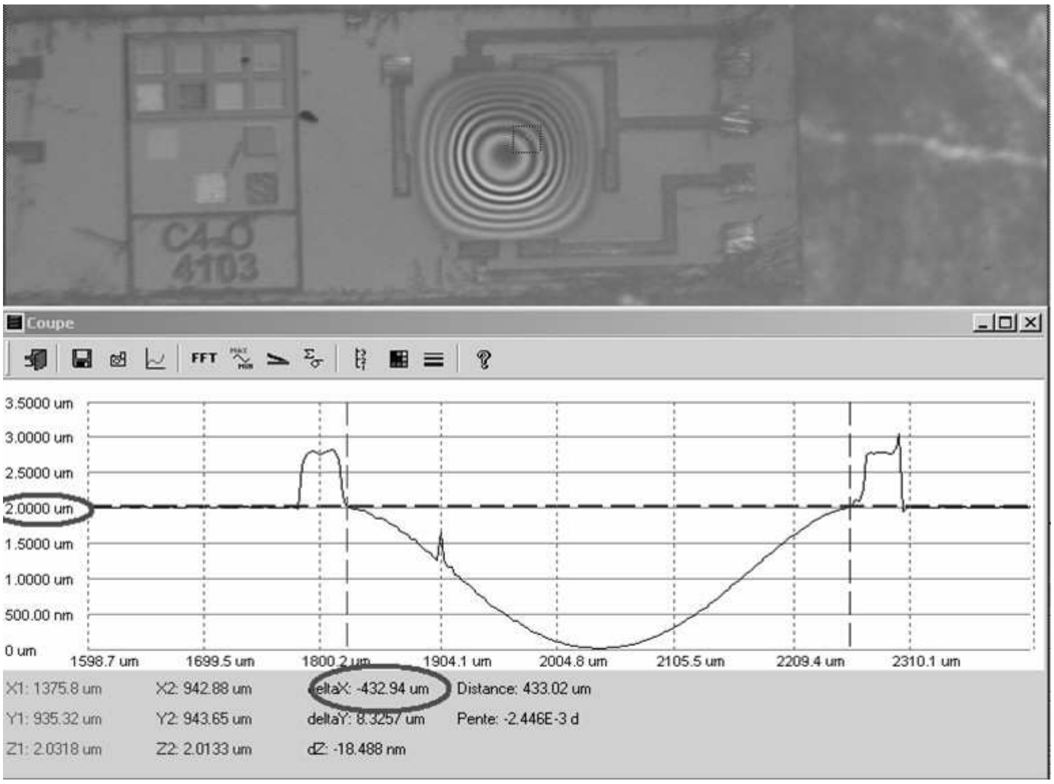

```
X1: 1375.8 um     X2: 942.88 um     eltaX: -432.94 um    Distance: 433.02 um
Y1: 935.32 um     Y2: 943.65 um     deltaY: 8.3257 um    Pente: -2.446E-3 d
Z1: 2.0318 um     Z2: 2.0133 um     dZ: -18.488 nm
```

Fig. 4.21 The optical profilmeter measurement of the deflected square membrane.

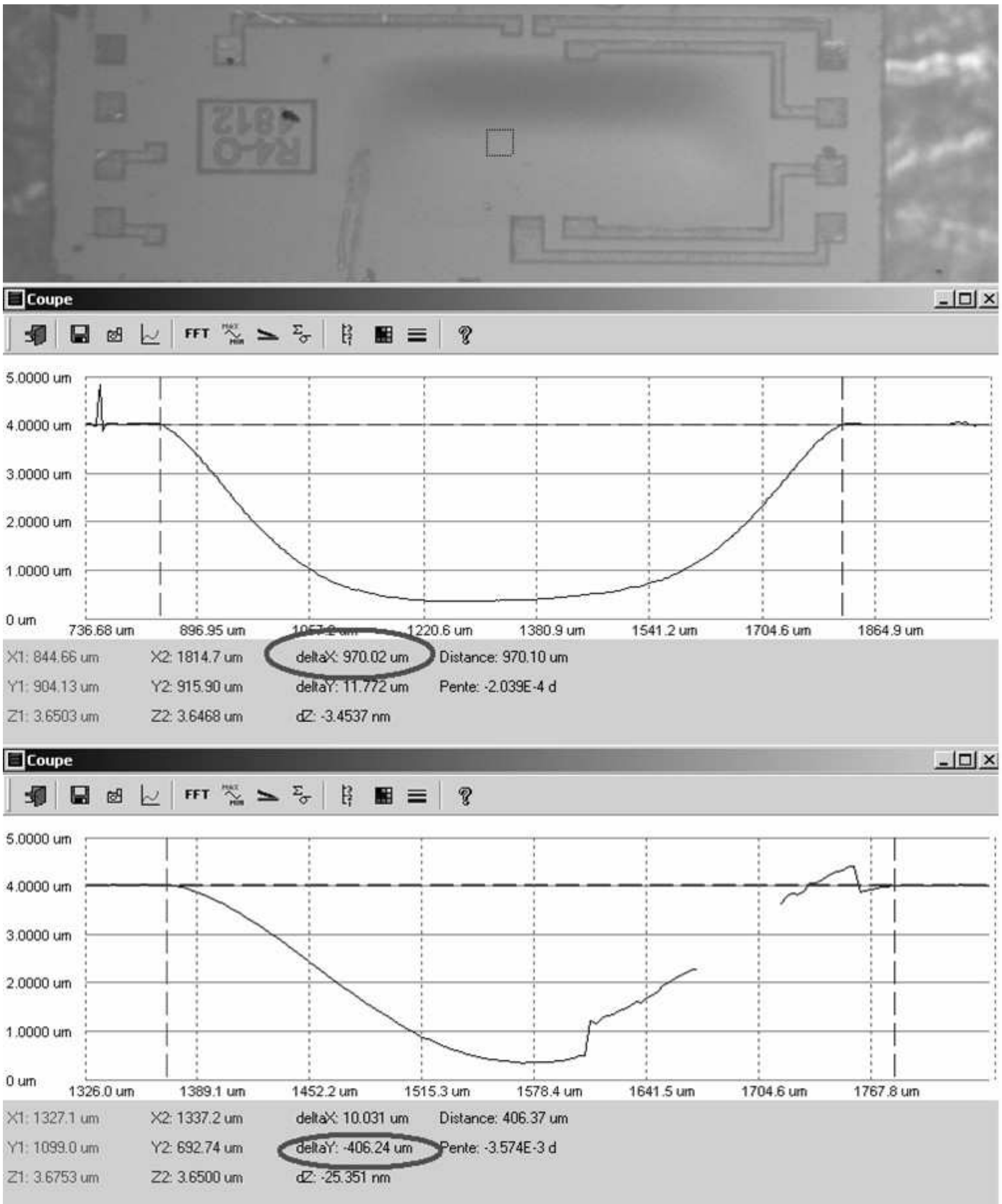

X1: 844.66 um X2: 1814.7 um deltaX: 970.02 um Distance: 970.10 um
Y1: 904.13 um Y2: 915.90 um deltaY: 11.772 um Pente: -2.039E-4 d
Z1: 3.6503 um Z2: 3.6468 um dZ: -3.4537 nm

X1: 1327.1 um X2: 1337.2 um deltaX: 10.031 um Distance: 406.37 um
Y1: 1099.0 um Y2: 692.74 um deltaY: -406.24 um Pente: -3.574E-3 d
Z1: 3.6753 um Z2: 3.6500 um dZ: -25.351 nm

Fig. 4.22 The optical profilometer measurement of the deflected rectangular membrane.

As one can clearly remark, measurements show that the lateral dimensions of the membranes differs significantly from the ones that were predicted (Table 4.3). The problem of discontinuous line at the lower profile of the rectangular membrane (Fig. 4.22) may be explained by the different coefficient of reflection of heavily doped P++ interconnection zone and it does not influence the lateral dimension measurements.

Table 4.3 Measured and predicted lateral membrane dimensions.

	Square	Rectangular
Predicted	300 µm x 300 µm	900 µm x 300 µm
Measured	433 µm x 433 µm	970 µm x 406 µm

In order to verify how the dimensions of the membrane became bigger, we decided to get a photo of the sensor cell cut along the membrane border using the scanning electron microscope (Fig. 4.23).

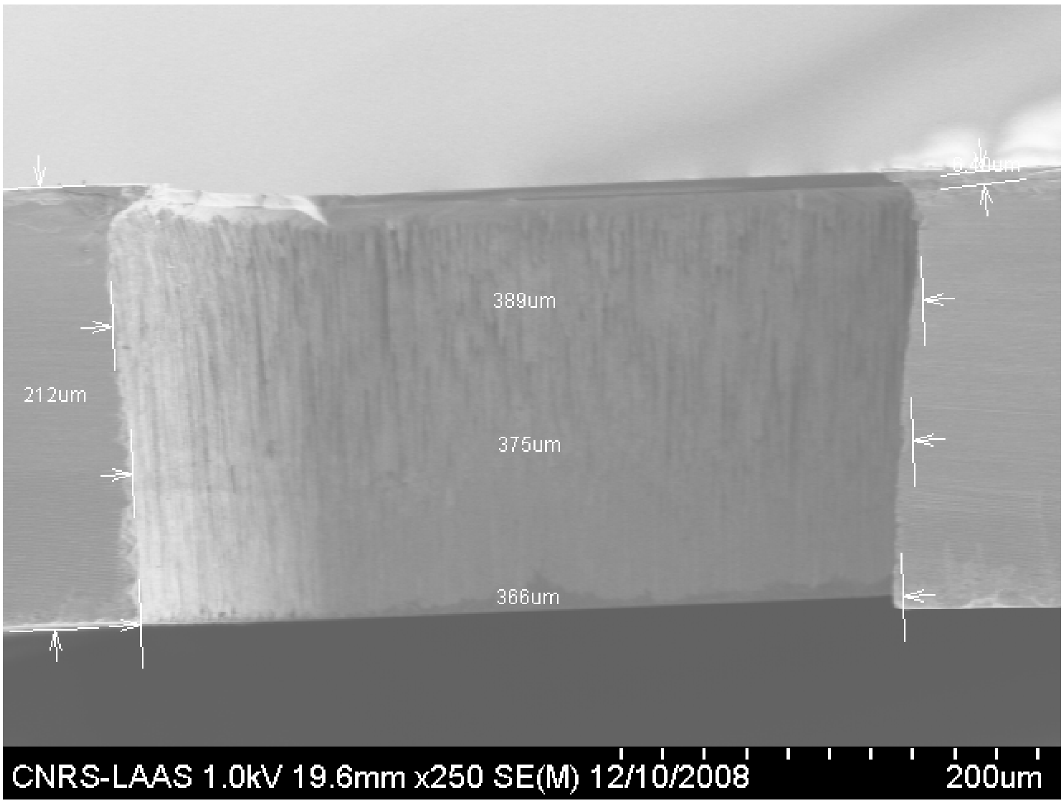

Fig. 4.23 The photo of the cut of the pressure sensor along the membrane border.

Observing the picture, one may easily remark that the DRIE process did not work correctly and the width of the etched hole increase with the depth (it become wider when closer to the membrane). It has to be emphasized that the dimensions marked in Fig. 4.23 are rather indicative while the sample was no perfectly aligned with respect to the camera.

Taking into consideration all above mentioned facts (real membrane lateral dimensions for differential sensors and thicknesses for all types of sensors), we recalculated the sensitivity value for all three samples and compare it to the measured value. Table 4.2 may be then rewritten as follows.

Table 4.4 Comparison of corrected predicted values and measured ones.

Parameter	differential		absolute
	square	rectangular	square
Sheet Resistance [Ω/square]	360 (+3.7%)	360 (+3.7%)	584 (+2.1%)
Calculated sensitivity [μV/V/mmHg]	21.3	96.3	44.8
Measured sensitivity [μV/V/mmHg]	22.2 (+4.2%)	95.4 (-1%)	36.1 (-19%)

Now one can clearly see that there is a very good match between the experimental and calculated results especially for the differential pressure sensor. The reason why for the absolute pressure sensor the difference is remarkable (-20%) is that in case of the square membrane gauges are placed in the regions were stress value is overestimated by the analytical model and the overestimation was shown to reach about 20% (see chapter 2). In case of the differential sensor, membrane lateral dimensions were greater so gauges were not at the membranes border but about 50 µm from them what proves that the used analytical model may be successfully used excluding the small zone at the membranes border where the overestimation should not be greater than 20%.

4.3.2 Offset measurements

As it was mentioned in the previous chapter, one of the important parameters of the sensor is the offset value. In the ideal case, this parameter should be as small as possible but also a stable as possible. The first condition is required as the highest offset value may decrease the dynamic of the sensor after the signal conditioning. As an example we can imagine easily that our sensor produces the sinusoidal output signal within the range -1V to 1V. If we want to use the amplifier that is supplied by the symmetrical voltage of -5V, 5V, we may easily set gain of our amplifier and use all dynamic range as it is shown in Fig. 4.24.

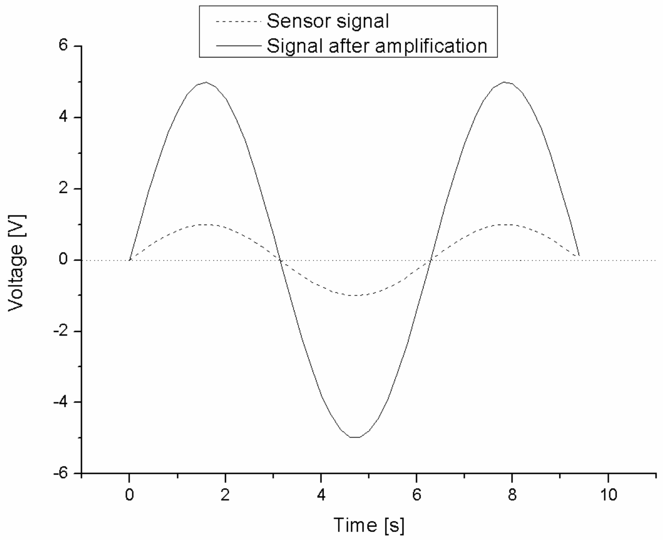

Fig. 4.24 Ideal case of the signal amplification (gain equal to 5) if there is no offset at the sensor output.

However if our sensor has an offset value of 0.5V, we have to decrease the gain of our amplifier as the offset will limit our dynamic range as it is shown in Fig. 4.25.

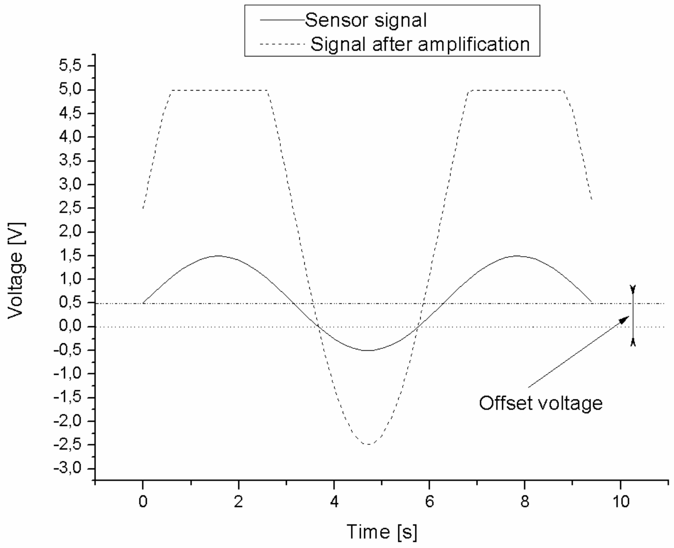

Fig. 4.25 The effect of the offset voltage on the dynamic range.

Nevertheless, the offset signal can be easily compensated as the output signal may be easily shifted by the simple electronic circuit. The problem arises when the offset voltage drifts due to different phenomena like temperature. Thus, we characterized our sensors in order to verify offset value and its temperature drift.

The results of measurements (offset voltage value normalized to the supply voltage value) we performed for both square and rectangular differential sensors (31 samples for each) using the on-wafer testing on a SUSS probe station are shown in Fig. 4.26.

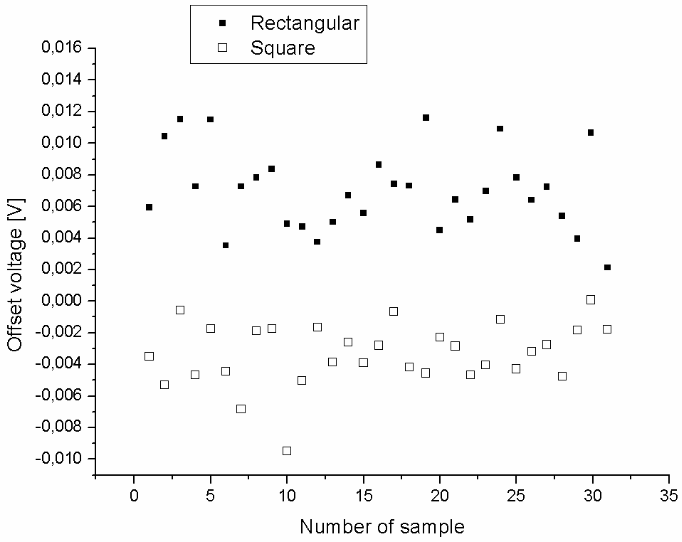

Fig. 4.26 The offset values for both rectangular and square sensors measured on wafer.

For square sensors the average value was calculated to be about -3.3mV with the standard deviation value of 1.9mV whereas for the rectangular ones the offset was much higher reaching 7.1mV with the corresponding standard deviation value of 3mV.

We then asked the question, what may be the origin of such an offset value. For square sensor, if we analyze the mask, we may easily notice that there is some asymmetry concerning the heavily doped interconnection layers (Fig. 4.27).

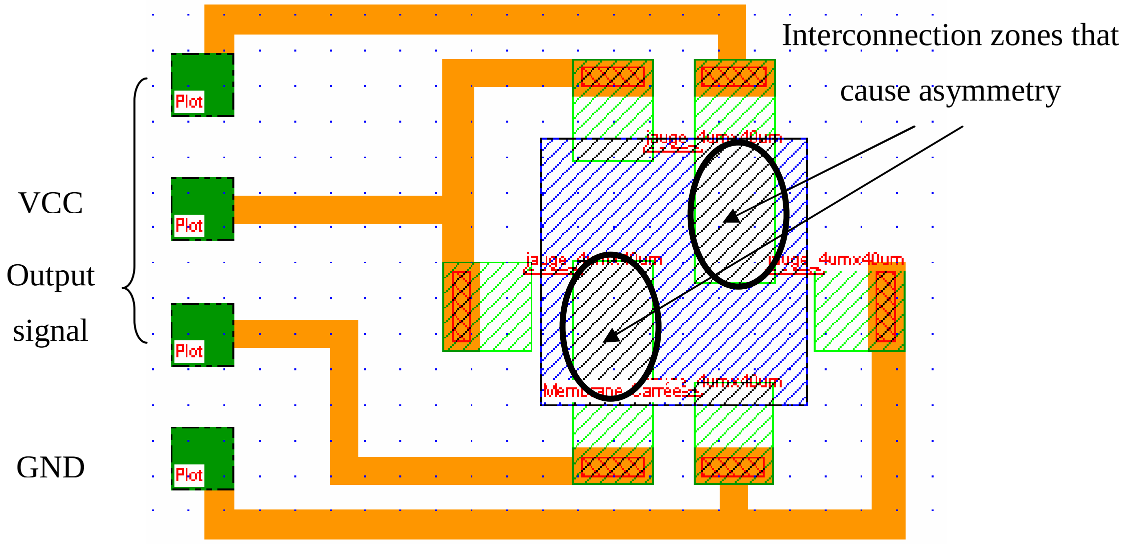

Fig. 4.27 The asymmetric heavily doped interconnection zones.

The sheet resistance value for the interconnection zones was then measured and calculated. Calculations were based on the real doping profile that was obtained using the SIMS technique. The sheet resistance values are shown in a Table 4.5.

Table 4.5 Measured and calculated sheet resistance values foe heavily doped zones.

Calculated sheet resistance [Ohms/square]	18.1
Measured sheet resistance [Ohms/square]	18.3

The marked asymmetrical regions (Fig. 4.27) are measured to be about 1.5 square each. It gives us the resistance value of about 27 Ω per each regions. If we take into account that there are two regions we have the asymmetry of the resistance ΔR value between the two Wheatstone bridge branches which may be estimated to be about 54 Ω. Having in mind that the average resistance value R_0 for each gauge was estimated to about 3660 Ω, we may easily use the equation 2.45 and calculate the possible offset value dV (4.3).

$$\frac{dV}{V}=\frac{\Delta R}{4R_0}=\frac{54\Omega}{4\cdot 3660\Omega}\approx 3.68mV \tag{4.3}$$

Such a value, corresponds to the measured one (3.3 mV) what means that in future mask we may eliminate such an offset by different mask design.

Nevertheless, in case of rectangular sensor the measured offset value is much higher (7.1 mV), even if the mask is perfectly symmetrical (Fig. 4.4 lower part). Applying our statistical design tool, we check what factors are the crucial ones and influences the most the gauge resistance and thus, the difference between different gauges that causes the offset value. We found that there are two factors with the highest impact: gauge width and the implanted dose. We also remarked that the only difference between square and rectangular sensors is that the orientation of the gauges is different. In case of square sensor all four gauges are positioned in the same direction while in case of rectangular one, pairs of gauges are parallel to each other (see Fig. 4.4 lower part). We then concluded that the possible source of the offset voltage is different lateral dimension in horizontally and vertically placed gauges or the implanted dose loss caused by the shadowing effect.

As we analyzed in details the parameters of the mask fabrication equipment DWL 200 Heidelberg, we found that the minimal precision in the X axis is set to 200nm whereas for Y axis it is set to be 400nm what can be the source of the different gauge width and thus the measured offset values.

The second possible reason of the difference in the gauges resistance may be the shadowing effect. Such an effect appears when we implant the dopants with a small tilt angle (typically about 7°) in order to avoid the channeling effect (Fig. 4.28 left). As at our laboratory the ionic implanter does not support the wafer rotation feature, the tilted ion bunch is always oriented in the same configuration with respect to the wafer primary flat. It causes that there is always one pair of gauges that is affected by the shadowing effect that limits the effective implantation area (Fig. 4.28 right).

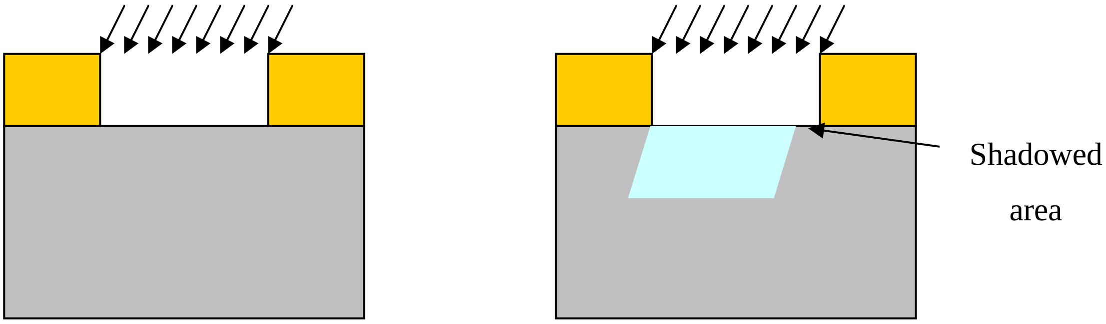

Fig. 4.28 The example of the shadowing effect cause by the implantation performed at small tilt angle.

4.3.3 Temperature characteristics

4.3.3.1 Measurement setup

As we measured the sensitivity at room temperature, we decided to measure the *TCR* values for two doping profiles that were used. In order to measure it we used the semiautomatic probestation SUSS microtec® AP200 that was described earlier. Such on-wafer measurement allowed us to eliminate all thermomechanical stresses that may appear due to the packaging. We then measured the resistance for four different temperatures: 25°C, 40°C, 55°C and 70°C in order to evaluate both quadratic and linear terms of *TCR*. The temperature of the chuck was set with a precision of 0.1°C and each time it was changed, the vacuum that holds the wafer in the aligned position was cut off and applied again after 20 minutes. Such a procedure was necessary in order to allow the wafer to expand due to the thermal coefficient of expansion and thus, it eliminated additional thermomechanical stresses that might have been induced and cause some additional errors.

Recall that the resistance value $R(T)$ in a function of the temperature ΔT may be expressed as follows (4.4), we may easily estimate both linear α and quadratic β terms of *TCR* if we are provided with the quadratic function that was fitted to the measurement data.

$$R(T) = R_0\left(1 + \alpha(\Delta T - T_0) + \beta(\Delta T - T_0)^2\right) \tag{4.4}$$

It has to be remarked that the R_0 value is the reference resistance value at reference temperature T_0 = 25°C. According to such assumptions the calculation procedure consists of fitting the second order polynomial to the measurement results and then extracting searched *TCR* terms. All fitting and calculations were performed in MATLAB® environment.

4.3.3.2 TCR measurements

Using the previously described procedure, we then measured the *TCR* value for our two strain gauges with different doping level as it was shown in Fig. 4.14 and Fig. 4.15. The measurements were taken for nine different gauges at different positions on the wafer. After the fitting of quadratic polynomial values of linear and quadratic *TCR* coefficients are shown below (Fig. 4.29).

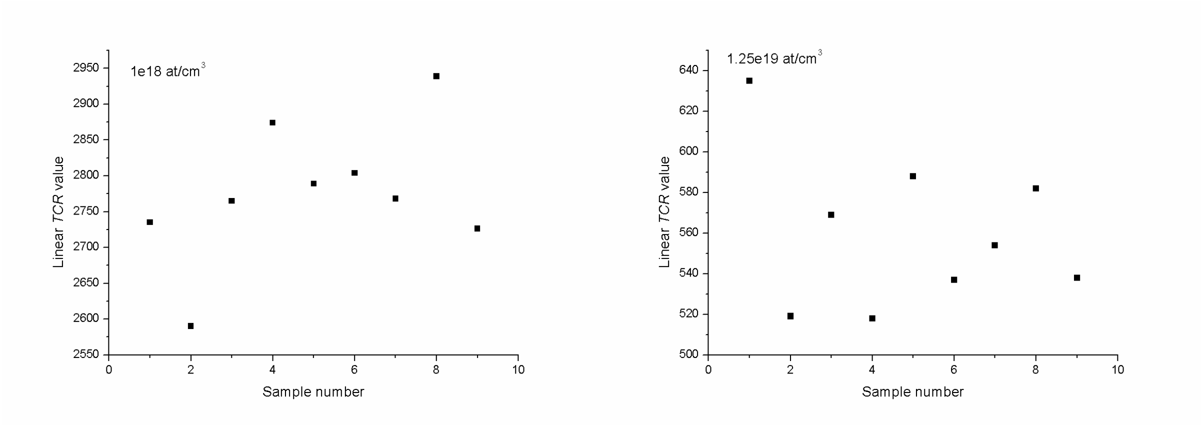

Fig. 4.29 Measured linear *TCR* values for two different doping profiles with the surface concentration of about 10^{18} at/cm^3 (left) and $1.25 \cdot 10^{19}$ at/cm^3 (right).

We also calculated the linear and quadratic TCR coefficients value using the Arora’s model taking into account doping profiles. The comparison between them is shown in a Table 4.6.

Table 4.6 The comparison between experimental results and calculated values of linear *TCR* coefficient.

Maximal doping concentration	10^{18} at/cm^3	$1.25 \cdot 10^{19}$ at/cm^3
Predicted linear *TCR* [ppm]	1859	1477
Measured linear *TCR* [ppm]	2699 (+45%), $\sigma = 68$	561 (-63%), $\sigma = 45$
Predicted quadratic *TCR* [ppm]	3.5	-0.2
Measured quadratic *TCR* [ppm]	6.18, $\sigma = 0.76$	3.7, $\sigma = 0.99$

Such a high mismatch between experiment and calculations leaded us to perform our own experiments that allowed us to investigate the *TCR* value for doped silicon.

4.3.3.3 Offset thermal drift measurement

As we mentioned earlier, not exactly the offset value is important but its drift. We have used the same set of samples and measured the temperature drift of the offset. We changed the temperature for 23°C to 40°C and measured the offset values assuming that the offset changes linearly with the temperature. The result of such a measurement for rectangular (Fig. 4.30) and square (Fig. 4.31) sensors are shown below.

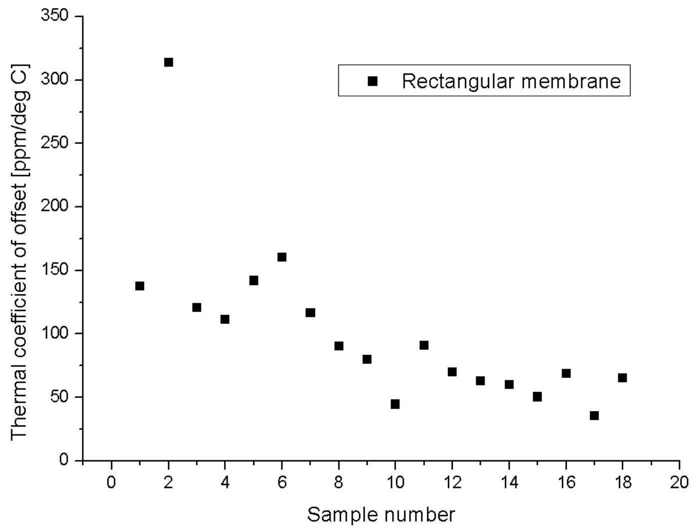

Fig. 4.30 Thermal coefficient of the offset voltage for rectangular sensors.

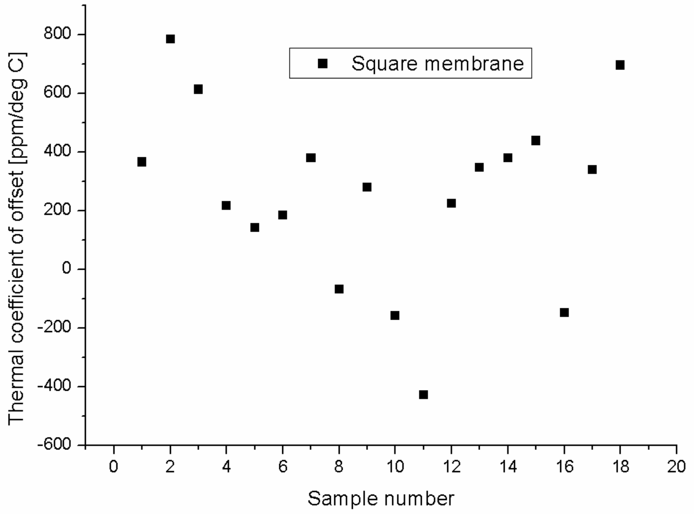

Fig. 4.31 Thermal coefficient of the offset voltage for square sensors.

As one can see, for the square sensors values are much more dispersed than for the rectangular sensors reaching the average value of 255 ppm with the standard deviation value of 308 ppm. For the rectangular sensors the mean value is equal to 89 ppm with the standard deviation value of 36 ppm.

Recall that the thermal drift of the offset voltage for a Wheatstone bridge depends only on the **difference** between *TCR* of the each resistance in a bridge (equation 2.49), the first conclusion could be that the mismatch between *TCR* should be greater for the square sensors. Consequently, having in mind that the *TCR* coefficient depends only on the doping level, the difference in doping level between gauges should be also greater for the square sensors. The problem is that it is contradictory to the results that we obtained for the offset measurement that were presented earlier. The offset value was much smaller for the square sensors where gauges have same orientation and only the asymmetry is rather responsible for the offset value.

The hypothetical explanation of such a behavior may be based on the thermomechanical stress appearance. As there is a thin oxide layer between the membrane and the silicon substrate (Fig. 4.7), it is possible that due to the difference of thermal coefficient of dilatation the thermomechanical stress appears at the interface of these two materials. Having in mind that in case of square sensors gauges are placed near the clamping region, such a stress may affects stronger such a region and be quite dispersed as the real clamping point is difficult to control perfectly due to the imperfect etching process. For the rectangular membranes gauges are placed on their centers so very far form the clamping zone and thus, probably the influence of the thermomechanical stress may be lower.

4.3.4 Experimental verification of mobility values

As we may notice, despite some reports [59, 96] confirming Arora's model, there is a quite large mismatch between the *TCR* coefficient obtained by using this model and experimental results. Therefore, we tried to investigate more deeply *TCR* values for different doping levels. As it was shown in chapter 2, the doping profiles plays a key role in the correct modeling of the mobility in the diffused layer. Thus, we decided to fabricate the resistances with different but **uniformly distributed** doping levels and then measure their *TCR* values. In order to do that, we used the SOI wafers with the very thin device layer with controlled thickness. Among many products available on the market we decided to use the product of SOITEC®. The basic characteristics of the wafer are presented in the Table 4.7.

Table 4.7 The parameters of SOI wafers that were used.

Parameter	Value
Device layer thickness	340 nm ± 25nm
Box oxide thickness	400 nm ± 5 nm
Overall wafer thickness	523 µm ± 15 µm
Doping level of the device layer	P-type (boron) 10^{15} at/cm^3

Such a thin layer allows us to implant the selected dose and then anneal the sample in order to redistribute the dopants **quasi uniformly** over the device layer depth. The word quasi is used because some boron will diffuse into the oxide layer due to the phenomenon of the boron out-diffusion [97],[98]. Nevertheless obtained profile should be considered as uniform what will be proven by the SIMS analysis.

4.3.4.1 Design and fabrication of test structures

The test structures consists of resistors that are implanted into the device layer. In the beginning, the SOI wafer (Fig. 4.32 a)), is oxidized in order to obtain the thin screening oxide layer (Fig. 4.32 b)).

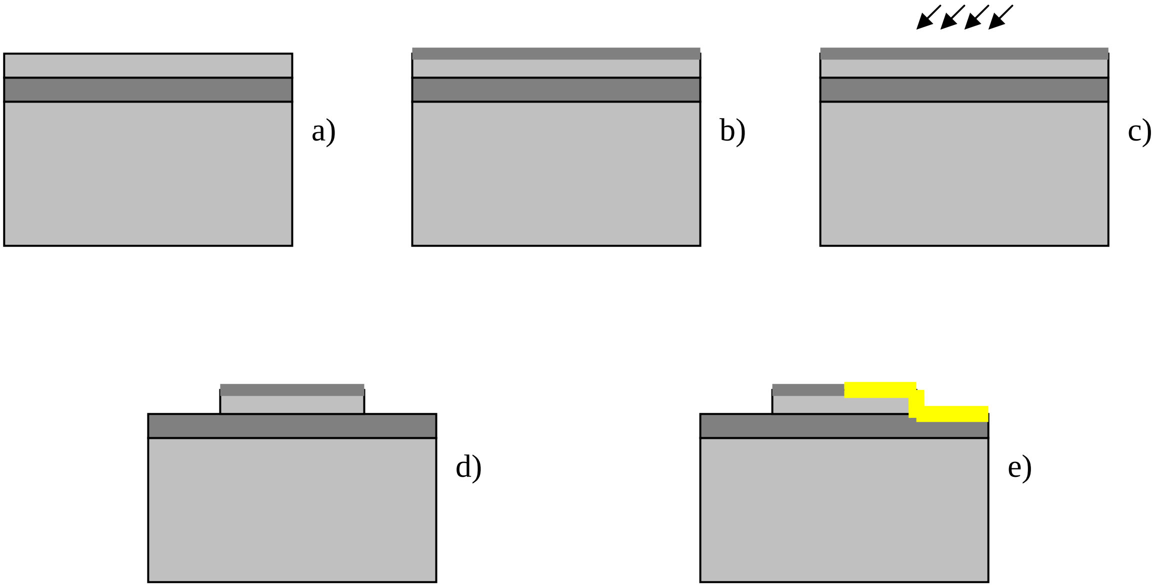

Fig. 4.32 The simplified process view. After oxidation b) the ion implantation and annealing is performed c). Then the device layer around gauges is etched d) and metallic interconnections are created d).

Then, resistors and highly doped interconnections are subsequently created by using the ion implantation technique and the high temperature annealing (Fig. 4.32 c)). Finally, we etch the silicon device layer around gauges and interconnections in order to obtain good electrical isolation (Fig. 4.32 d)). As the last step, access holes in the oxide layer are etched and metallic interconnections are deposited and formed using the lift-off process (Fig. 4.32 e)).

The mask of the designed cell, which is in fact the pressure sensors, are depicted below (Fig. 4.33).

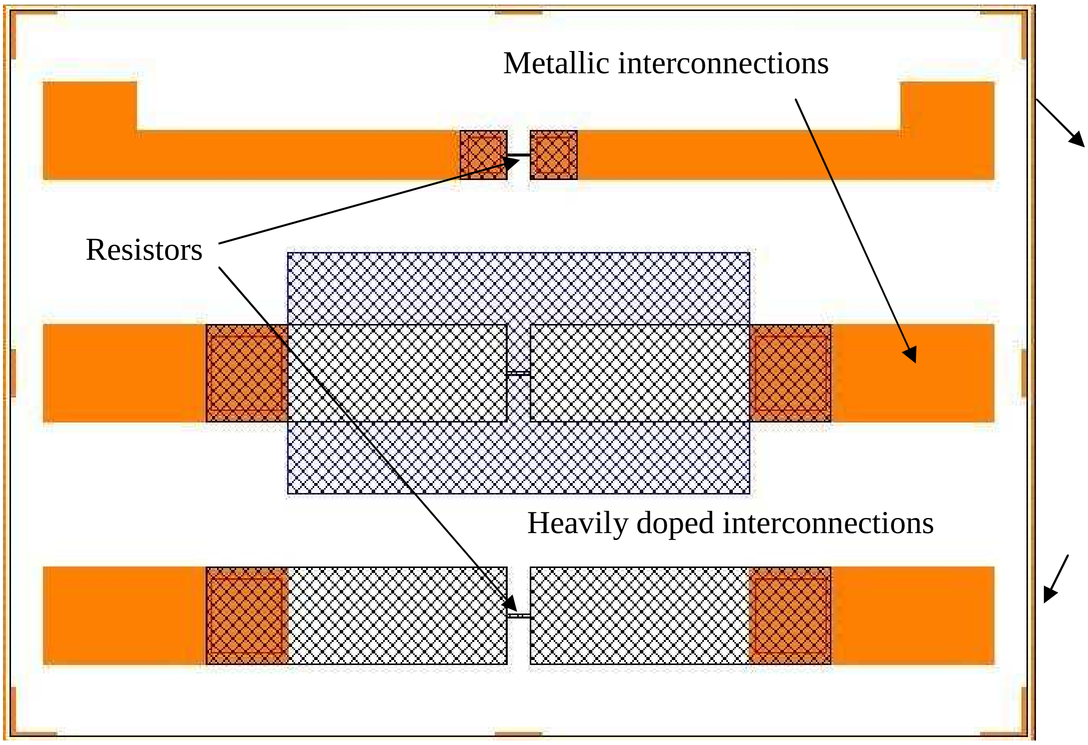

Fig. 4.33 The designed cell used for the *TCR* measurement.

In fact the basic cell consists of three gauges where one is connected directly to the metal via highly Boron doped vias in order to preserve good ohmic contact. Two other gauges are connected to the metal by highly doped interconnection layers and one of them is placed on the membrane what may be used in future for the experimental verification of the piezoresistance coefficient.

According to the process shown in Fig. 4.32, six different doses where implanted ranging from 10^{14} at/cm^3 to $5{\cdot}10^{14}$ at/cm^3 in order to obtain different doping levels. Such a range is rather used while the resulting sheet resistance value varies from about 200 Ω/square to 1500 Ω/square. As we remarked earlier, the **quasiuniform** doping profile may be achieved by using such a fabrication process. If we, for example, consider the implanted dose of 10^{14} at/cm^3 ,simulations performed in the process simulator provided us with the final dopants distribution. Nevertheless, during the annealing stage, as it was mentioned earlier, the Boron has the tendency to diffuse into oxide layer. As a result, the real doping profile obtained during such a process that was extracted by using the SIMS technique (Fig. 4.34).

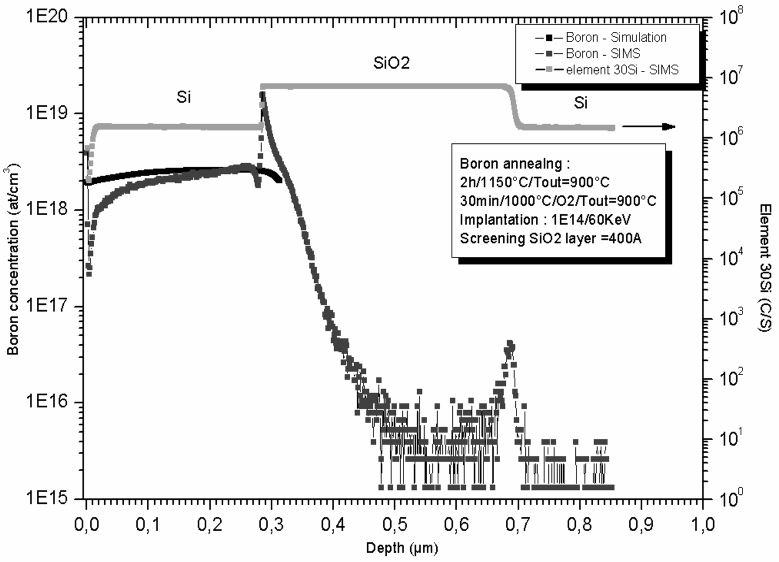

Fig. 4.34 Simulation of the dopants distribution for the implanted dose of 10^{14} at/cm^3 and corresponding SIMS analysis.

As one can see, the boron that was near the surface diffused into the oxide layer what, as a result, caused that the fabricated profile differs from the one obtained by the simulation. Nevertheless, we may say that the obtained profile may be considered as quasi uniform while the dopants concentration varies approximately from 10^{18} at/cm^3 to $2\cdot10^{18}$ at/cm^3 over the whole structure depth. We then performed the SIMS analysis for the other implanted doses that vary form 10^{14} at/cm^3 to $5\cdot 10^{14}$ at/cm^3 and compared it to the simulation as it is shown on Fig. 4.35 ÷ Fig. 4.38.

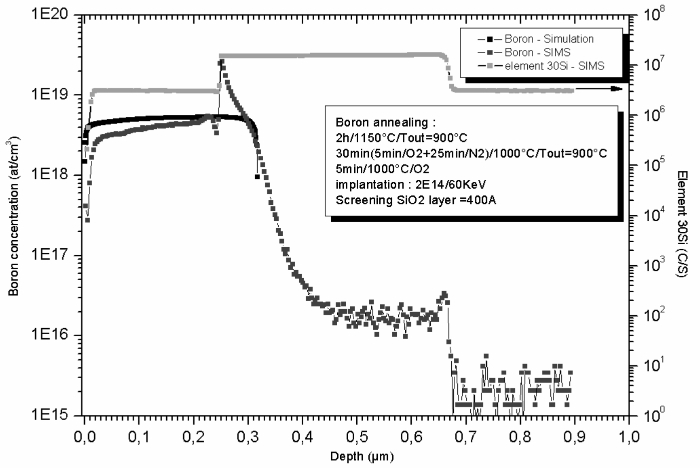

Fig. 4.35 Simulation and SIMS profile of the dopants distribution for the implanted dose of $2\cdot10^{14}$ at/cm^3.

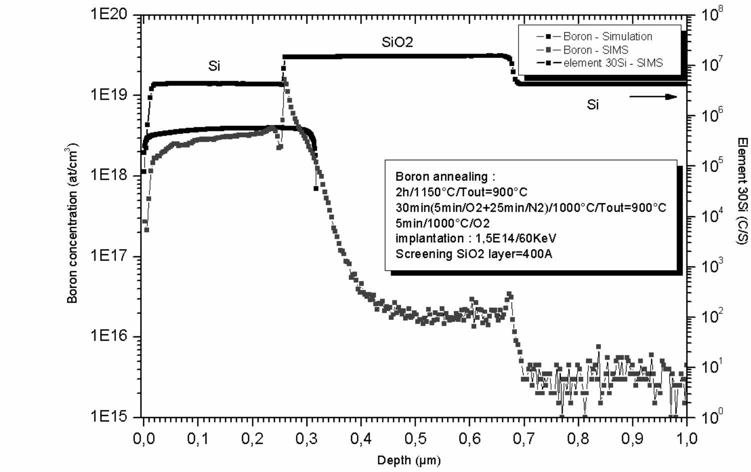

Fig. 4.36 Simulation and SIMS profile of the dopants distribution for the implanted dose of 1,5·10^{14} at/cm^3

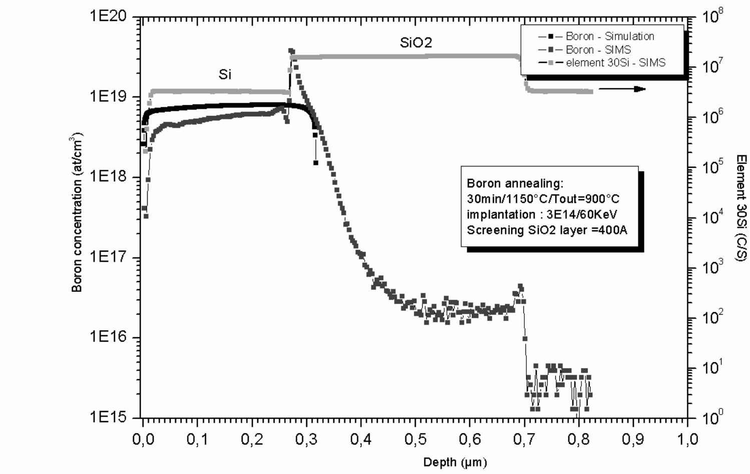

Fig. 4.37 Simulation and SIMS profile of the dopants distribution for the implanted dose of 3·10^{14} at/cm^3

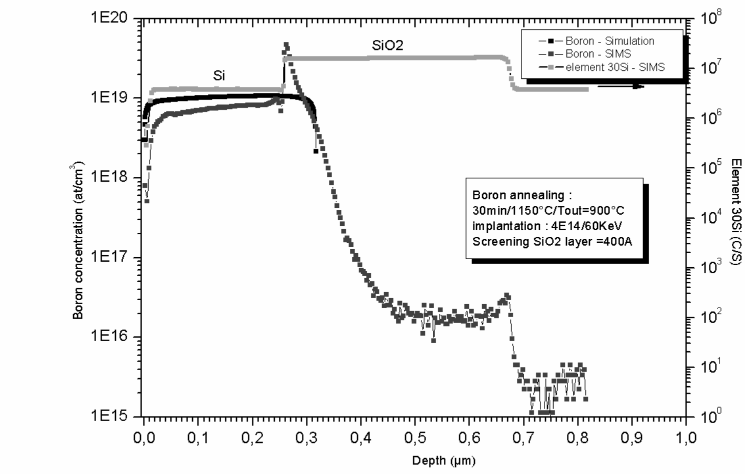

Fig. 4.38 Simulation and SIMS profile of the dopants distribution for the implanted dose of 4·10^{14} at/cm^3.

4.3.4.2 TCR measurements

We used the same measurement setup and methodology that was used in case of the gauges *TCR* measurement. Measurements were taken for about twenty samples for each implanted dose. The sample result for the doping level of $1.75 \div 2.5 \cdot 10^{18}$ is shown below (Fig. 4.39).

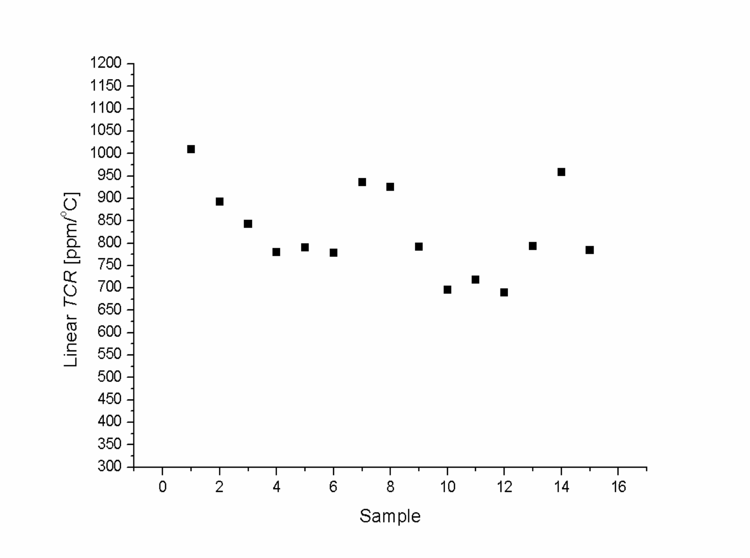

Fig. 4.39 Exemple set of measurements of the linear *TCR* coefficient.

Then, the statistical mean value and standard deviation was calculated. According to this methodology, linear and quadratic *TCR* coefficients were estimated for six different doping levels. Of course as we could see the doping level is not perfectly constant but if we consider it as linearly changing over the gauge thickness we may give it as the range of the doping concentration. The result of such an analysis is shown in Table 4.8.

Table 4.8 Linear and quadratic TCR coefficients for different doping levels.

Doping level	Linear *TCR* coefficient α [ppm/°C]	Quadratic *TCR* coefficient β [ppm/°C]
$1.75 \div 2.5 \cdot 10^{18}$	825	9.2
$2.5 \div 3.25 \cdot 10^{18}$	334	10.1
$4.8 \div 6.1 \cdot 10^{18}$	161	8.3
$6.8 \div 8.1 \cdot 10^{18}$	153	8.7
$8.2 \div 10 \cdot 10^{18}$	200	8.4

Let us then trace the obtained results in comparison to the ones predicted by the Arora's model for the linear and quadratic TCR coefficient (Fig. 4.40).

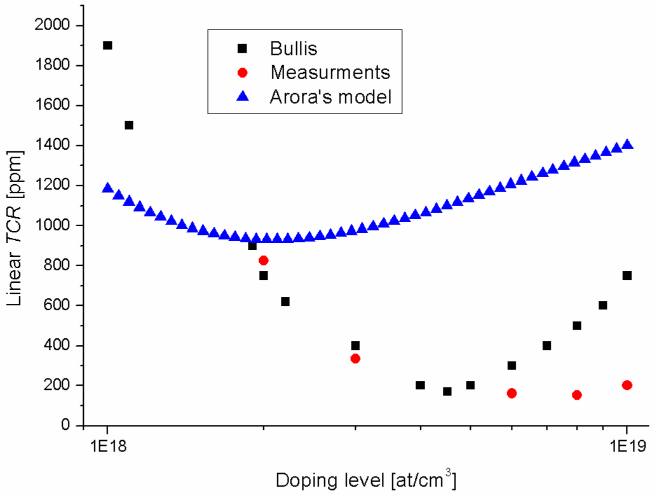

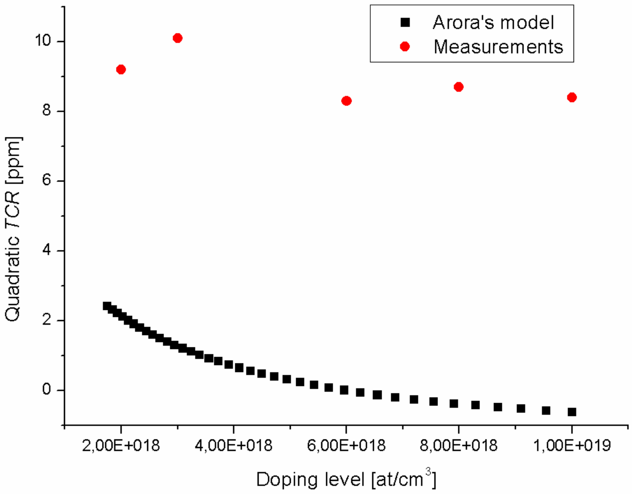

Fig. 4.40 values of the linear and quadratic components TCR in comparison to the predicted ones.

As one can clearly see, for the linear component of TCR there is quite large mismatch between the predicted and measured values. If we recall Fig. 2.18, we may then noticed that the experimental points published by Bullis are much closer to the measured ones and for the narrow range between 1 and $5 \cdot 10^{18}$ are almost identical. If we consider additionally the quadratic component, the analytical model also definitely fails. According to the author’s knowledge there is no report on the experimental determination of the quadratic component of the TCR coefficient so there is no comparison with any experimental data. As a conclusion, we may than say that despite some reports that confirm the Arora’s mobility model (more precisely the temperature dependence) results may not be always trustworthy. For example the minimum *TCR* value for mathematical model is about 1000 ppm while we measured values lower than 200 ppm what makes **five** times less. It also confirms that during the design stage it has to be taken into account while some assumption about the *TCR* were crucial like in case of the temperature auto compensation (see p. 31). Some more detailed study should be conducted in the area of *TCR* approximation in order to find an analytical formula that allows us to predict correct thermal behavior of the doped resistances and this issue remains a future problem. Nevertheless, we may conclude that near the room temperature, the data published by Bullis or modified Arora’s model should be rather used in order to correctly predict sensor performance.

5 Conclusions

5.1 Summary

In this work, an overview on the modeling and optimization of a piezoresistive pressure sensor was given. It was shown that such a process is definitely not a trivial task as it is necessary to perform a multi domain analysis which includes all specific phenomena that occurs in such a system. We started with the basic theory concerning the mechanical behavior of the membrane in the linear regime and presented the analytical description concerning three basic geometrical shapes of perfectly clamped membranes. It was followed by a detailed presentation of the piezoresistivity phenomenon in Silicon along with its analytical description that is commonly used in order to model it. Then experimental data that are available up to now and justify the choice of the model that was used to simulate the pressure sensor were presented. Consequently, some details about the mobility modeling in silicon and some existing models were shown. Then, the overview of the Wheatstone's bridge, the simplest electronic readout circuit used for the resistance measurement was discussed along with the power supply issues that may affect the sensor characteristics.

The important problem that was discussed concerned the detailed strain gauge modeling which takes into account the nonuniform profile of the diffused layer. It was shown that the doping profile of such a layer may be successfully described by the Gaussian approximation and based on it, we derived formulas that allow us to calculate the interesting "effective" gauge parameter like resistance value, *TCR* and piezoresistive coefficient. Moreover, it was presented that the doping nonuniformity of the profile affects significantly first two parameters and under some condition also the third one, so it has to be taken into account if one wants to design sensor correctly.

Finally, it lead us to the description of the most used technique in the Microsystems design-the FEM analysis. We showed the possible methods of model building and focused on the detailed strain gauge modeling. Then, the comparative analysis between FEM and analytical approach was performed and advantages, as well as drawbacks, of two methodologies were

discussed. It was pointed out that the difference between two methodologies are rather in the mechanical domain and two basic phenomena that may make results of the analytical model invalid are thermomechanical stresses and real clamping conditions. We quantitatively estimated the error that may appear if we take into account such phenomena and discussed at which conditions it occurs.
As a result, the simulation tool that was created by using the MATLAB® environment which uses the complete analytical model of the piezoresistive pressure sensor and allows the designer to perform the rapid analysis of the defined system was presented.

The next part of this work was dedicated to the optimization tool for the sensor design. We introduced the basics of optimization techniques and explained how to use the developed rapid analytical model in order to perform the fast optimization stage. Moreover, some explanation about how to deal with the multiobjective problem using the standard single objective algorithms that are widely known was given. We then tried to propose the different design methodology that may decrease the time-consuming optimization loop performed usually by the FEM analysis. The results allowed us to present the optimizer tool that was created in order to help the designer to obtain the design that fulfils defined project requirements in a fast and simple way what was shown in the case study example.

Additionally, we extended our design methodology by the statistical analysis which may be helpful from the manufacturing point of view. The statistical analysis was chosen because our model is extremely rapid and, at the same time, quite complicated analytically what increases the complexity of the standard derivative based method. Such an analysis, if properly used, may response to many questions including the estimated production yield at the simulation stage. The price that one have to pay is the necessity of the particular cleanroom equipment characterization what may be done rather when one use processes that are well characterized. Such an analysis is essential from the industrial point of view if one plans to deliver reliable product as in the case of the project that was the base of this work. Consequently, we proposed the statistical analysis tool that may cooperate with the first two tools giving the designer the possibility of estimating the sensor characteristics taking into account the process imperfection.

In the last part, the experimental results were presented in order to validate the proposed methodology. We presented the fabrication processes that were used for both, differential and absolute pressure sensor where in the second case we put some light onto bonding technique that is one of the base of today's pressure sensors. In case of differential pressure sensor we explained the problem of the DRIE overetching what caused the high mismatch between experimental and predicted results. After taking into account all fabrication imperfections we have shown that the mechanical and piezoresistive model worked correctly in terms of sensitivity for the applied pressure within the limits shown in the second chapter concerning real clamping conditions.

Nevertheless, the mobility dependence on temperature did not match experimental data and thus, the own investigation was conducted in order to gather the experimental data on the *TCR* coefficient as a function of the doping level. The test structures were then designed and fabricated. After the measurements, we have shown that despite some works confirming the Arora's model experimentally, we found that the Bullis experimental data are much closer to the reality while the modeled values differs even few times from the one that were measured. In conclusion, such data have to be rather used if one wants to predict the thermal behavior of the piezoresistive pressure sensor correctly.

5.2 Perspectives

As a result of this work, methodology that may decrease time to market during the piezoresistive pressure sensor design was proposed. Nevertheless, as one could remark the existing models not always match the reality. Thus, the own investigation of the author in order to gather the experimental data on *TCR* coefficient was conducted. Obtained experimental results, even covering the narrow range of the doping levels, are very encouraging for future work where more test structures will be fabricated in order to cover much wider range of implanted doses. Moreover, similar types of structures may be designed in order to verify the temperature drift of piezocoefficents experimentally what, as it was presented in this work, is crucial in the proper design of the sensor.

If we consider again the methodology, the interesting continuation of this work may be application of the design for reliability approach where one may combine the statistical design tool with the optimizer in order to optimize the project to be not only high performance but also reliable and fabricated at high yield. We may, for example, easily imagine that the optimizer will not only try to maximize the sensitivity value but also minimize its standard deviation value using the statistical analysis, Nevertheless for such an approach, the more detailed study on the cleanroom equipment reproducibility should be conducted in order to verify the proposed method.

6 References

1. H. Nathanson, W. Newell, R. Wickstrom and J. Davis, “The resonant gate transistor,” *IEEE Transactions on electronic devices*, 1967.

2. www.enablingmnt.com/

3. www.electronics.ca/

4. K. J. Rebello, “Applications of MEMS in Surgery,” *IEEE Proceedings*, vol. 92, No. 1, January 2004.

5. M. Mack, “Minimally invasive and robotic surgery,” *J. Amer. Med. Assoc.*, vol. 285, no. 5, Feb. 7, 2001, pp. 568–572.

6. “Micro and nano technologies: A world wide view,” *Associazione Italiana per la Ricerca Industriale*, Rome, Italy, 2001.

7. K. Dewdney, “Nanotechnology: Wherein molecular computers control tiny circulatory submarines,” *Sci. Amer.*, vol. 258, Jan. 1988, pp. 100–103.

8. Lauks, “Microfabricated biosensors and microanalytical systems for blood analysis,” *Acc. Chem. Res.*, vol. 31, no. 5,1998, pp. 317–324.

9. R. L. Courant, “Variational Methods for the Solution of Problems of Equilibrium and Vibration,” *Bulletin of the American Mathematical Society*, No. 49, 1943, pp. 1-23.

10. F. Bennini, J. Mehner and W. Dötzel, „Computational Methods for Reduced Order Modeling of Coupled Domain Simulations,” *11 International Conference on Solid State Sensors and Actuators (Transducers 01)*,p. 260-263, Germany 2001.

11. E. Landau, F. Lifschitz, *Theory of elasticity* (2nd edition), Pergamon Press, 1970

12. E. Ventsel, T. Krauthammer, *Thin Plates and Shells: Theory, Analysis, and Applications*. Marcel Dekker, Inc., New York, New York, 2001.

13. L. Euler, “De motu vibratorio tympanorum,” *Novi Commentari Acad Petropolit*, Vol. 10, 1766, pp. 243 – 260.

14. J. Bernoulli, “Essai theorique sur les vibrations de plaques elastiques rectangularies et libers,” *Novi Commentari Acad Petropolit*, Vol. 5, 1789, pp. 197-219.

15. G. R. Kirchhoff, “Uber das gleichgewichi und die bewegung einer elastishem scheibe,” *J. Fuer die Reine und Angewandte Mathematik*, Vol. 40, 1850, pp. 51 –88.

16. J. L. Lagrange, *Ann Chim*, Vol. 39, 1828, pp. 149 – 207.

17. S. D. Poisson, “Memoire sur l’equilibre et le mouvement des corps elastique,” *Mem Acad Sci*, Vol. 8, 1829, p. 357.

18. S. P. Timoshenko, “Sur la stabilite des systemes elastiques,” *Ann des Points et Chaussees*, Vol. 13, 1913, pp. 496 – 566.

19. S. P. Timoshenko, and S. Woinowsky-Krieger. *Theory of Plates and Shells* (2nd edition), McGraw-Hill, New York, New York, 1959.

20. K. Petersem „Silicon as a mechanical material,” *Proceedings of the IEEE*, vol. 70, no. 5, May 1982, pp. 420-457.

21. Tai-Ran Hsu, *MEMS and Microsystems: Design and Manufacture.* McGraw-Hill, New York, 2002

22. J. F. Nye, *Physical properties of crystal,* Oxford University Press, London, 1957

23. J. Wortman, R. Evans, „Young’s modulus, Shear modulus and Poisson ratio in Silicon and Germanium” *Journal of Applied Physics*, vol. 36, no. 1, Jan 1965, pp. 153-156

24. M. Mehregany, M. Allen „The use of micromachined structures for the measurement of mechanical properties and adhesion of thin films” *IEEE 1986 Solid-State Sensors Workshop*, June 1986

25. F. Kerrour, F. Hobar, “A novel numerical approach for the modelling of the square shaped silicon membrane,” *Journal Semiconductors, Physics, Quantum Electronics and Optoelectronics,* 2006, vol. 9, no.4, pp. 52-57.

26. W. Ko, M. Bao, “A high sensitivity integrated circuit capacitive pressure transducer,” *IEEE Transaction on Electron Devices*, vol. ED-29, no. 1, 1982, pp. 48-56.

27. G. Blasquez, Y. Naciri, “Static response of capacitive pressure sensor with square or rectangular silicon Diaphragm” *Journal of Applied Physics,* vol. 22/7, 1987, pp. 505-510.

28. B. L. Hulme, “Discrete Galerkin and Related One-Step Methods for Ordinary Differential Equations” *Mathematics of Computation*, vol. 26, No. 120., Oct., 1972, pp. 881-891.

29. N. Ben Moussa, “Conception, modélisation et réalisation d’un capteur de pression capacitif Microélectronique” *PhD Thesis, Universite Paul Sabatier, Toulouse, 1985.*

30. C. S. Sander, J. W. Knutti, “A monolithic capacitive pressure sensor with pulse-period output” *IEEE Transactions on Electron Devices*, vol. 27, no. 5, 1980, pp. 927- 930.

31. Y. Ohasi, “Bending of a Thin Elliptic Plate of an Orthotropic Material Under Uniform Lateral Load,” *Zeitschrift fur Angewandte Mathematik und Physik,* vol. 3, No. 3, 1952, pp. 212-224.

32. P. W. Bridgman, „The effect of the homogeneous mechanical stress on the electrical resistance of crystals” *Phys. Rev*. vol. 42, Dec 1932, p.858.

33. C. S. Smith, “Piezoresistance effects in Germanium and Silicon”, *Physical Review,* vol. 94, No. 1, April, 1954, p. 42.

34. W. P. Mason, R. N. Thurston, “Use of Piezoresisive Materials in the Measurement of displacement, force and torque,” *Journal of the Acoustical Society of America*, vol. 29, No. 10, October, 1957, p. 1096.

35. W. G. Pfann, R. N. Thurston, “Semiconducting stress transducers utilizing the transverse and shear piezoresistance effect”, *Journal of Applied Physics,* vol. 32, No. 10, October 1961, p.2008.

36. O. N. Tufte, E. L. Steltzer, “Piezoresistive properties of Silicon diffused layers,” *Journal of Applied Physics*, vol. 34, No. 2, October 1963, p.313.

37. D. R. Kerr, A. G. Milnes, “Piezoresistance of diffused layers in cubic semiconductors,” *Journal of Applied Physics*, vol. 34, No. 4, April 1963, p.727.

38. Y. Kanda, “A graphical representation of the piezoresistance coefficients in Silicon,” *IEEE Transaction on Electron Devices*, vol. 29, No. 1, January 1982, pp. 64–70.

39. K. Suzuki, H. Hasegawa, and Y. Kanda, “Origin of the linear and nonlinear piezoresistance effects in p-type silicon,” *Jpn. J. Appl. Phys.*, vol. 23, 1984, pp. L871–L874.

40. P. Kleimann, B. Semmache, M. Le Berre, and D. Barbier, “Stress-dependent hole effective masses and piezoresistance properties of p-type monocrystalline and polycrystalline silicon,” *Phys. Rev. B*, vol. 57, 1998, pp. 8966–8971.

41. Y. Ohmura, “Numerical study of the piezoresistance effect in p-type Si,” *J. Phys. Soc. Jpn.*, vol. 61, 1992, pp. 217–226.

42. G. E. Pikus and G. L. Bir, *Symmetry and Strain-Induced Effects in Semiconductors*. New York: Wiley, 1974.

43. C. K. Kim, M. Cardona, and S. Rodriguez, “Effect of free carriers on theelastic constants of p-type silicon and germanium,” *Phys. Rev. B*, vol. 13, 1976, pp. 5429–5441.

44. J. K. Lenkkeri, “Nonlinear effects in the piezoresistivity of p-type silicon,”*Phys. Stat. Sol.*(b), vol. 136, 1986, pp. 373–385.

45. T. Toriyama, S. Sugiyama, „Analysis of Piezoresistance in p-type Silicon for Mechanical Sensors,” *Journal of MEMS*, vol. 11, No. 5, October 2002.

46. H. Wilson, *Theory of Metals*, (2nd edition), Cambridge University Press, Cambridge, England, 1953.

47. O. N. Tufte, E. L. Steltzer, “Piezoresistive properties of heavily doped n-type silicon,” *Phys. Rev*., vol. 133, 1964, p.A1705-A1716.

48. R. A. Smith, *Semiconductors*, Cambridge University Press, Cambridge, England, 1959.

49. W. B. Joyce and R. W. Dixon, *Appl. Phys.Lett.*, **31**, 1977, pp. 354.

50. N. G. Nilsson, *Phys. Sta. Solidi (a)*, ***19***, K75, 1973.

51. J. A. Harley, T. W. Kenny, “1/F Noise Considerations for the Design and Process Optimization of Piezoresistive Cantilevers,” *Journal of MEMS*, March 2002.

52. D.M. Caughey, R.E. Thomas, “Carrier mobilities in silicon empirically related to doping and field”, *Proc. IEEE*, vol. 55, 1967, pp 2192-2193.

53. N.D.Arora, J.R.Hauser, D.J.Roulston, “Electron and hole mobilities in silicon as a function of concentration and temperature”, *IEEE Trans. Electron Devices*, vol. 29, 1982, pp 292-295.

54. D. B. M. Klaassen, “A Unified Mobility Model for DeviceSimulation – I. Model Equationsand Concentration Dependence”, *Solid-State Electronics*, vol. 35, 1992, pp. 953-959.

55. J. M. Dorkel and PH. Leturcq, “Carrier Mobilities in Silicon Semi-Empirically Related toTemperature, Doping and Injection Level”, *Solid-State Electronics*, vol. 24, 1981, pp. 821-825.

56. Boukabache, P. Pons, „Doping effects on thermal behaviour of silicon resistor,” *Electronic letters*, vol. 38, No. 7, March 2002.

57. W. M. Bullis, F. H. Brewer, C. D. Kolstad, L. J. Swartzendruber, „Temperature coefficient of resistivity of Silicon and Germanium near room temperature”, *Solid-State Electron*. ,vol. 11, 1968, pp. 639-646.

58. D. Tanaskovic, Z. Djuric, Z. Lazic, „Influence of Impurity Distribution on Thermal Coefficients of Resistivity and Piezoresistivity of Diffused Layers of Silicon”, *Proc. of 20th International Conference on Microelectronics MIEL ’95*, vol. 2, pp. 573, 1995.

59. U. Sridhar, R. Foster, „Temperature coefficient of resistance of piezoresistors," *Technical Digest of Solid-State Sensor and Actuator Workshop*, 1992, pp.54-57.

60. G. Spitzlsperger, *Very brief introduction to ion implantation for semiconductors manufacturin*g, http://www.gs68.de/tutorials/, May 2003.

61. Hachicha, "Contribution au développementd'une méthode d'extraction des paramètres technologiques et physiques de structures bipolaires", *Phd Thesis, December 1995,University Bordeaux I, France*

62. J. Philibert, „One and a Half Century of Diffusion: Fick, Einstein, before and beyond", *Diffusion Fundamentals 2*, 2005, 1.1-1.10.

63. C. Bergaud, E. Cocheteau, L. Bary, R. Plana, B. Belier, „Formation of implantem piezoresistors under 100 nm thick for nanoelecromechanical systems, *Proc. IEEE MEMS 2002*, pp.360-363.

64. Benninghoven, F. G. Rudenauer, H. W. Werner, *Secondary Ion Mass Spectroscopy: Basic Concepts, Instrumental Aspects, Applicarions and Trends,* Wiley, New York, 1987.

65. Nyquist, H., "Thermal Agitation of Electric Charge in Conductors," *Phys. Rev.*, Vol. 32, 1928, pp. 110-113.

66. Hooge, F. N., "1/f Noise," *Physica*, Vol. 83B, 1976, pp. 14-23.

67. T. Pancewicz, R. Jachowicz, Z. Gniazdowski, Z. Azgin, P. Kowalski, „The empirical verification of the FEM model of semiconductor pressure sensor" , *Sens. Actuat.* A 76, 1999, pp. 260–265.

68. Chih-Tang Peng, Ji-Cheng Lin, Chun-Te Lin, Kuo-Ning Chiang, „Performance and package effect of a novel piezoresistive pressure sensor fabricated by front-side etching technology", *Sens. Actuat*. A 119 ,2005, pp. 28–37.

69. X. Chauffleur, "Modelisation par la methode des elements finis du comportement thermomecanique de capteurs de pression capacitifs et piezoresistifs en silcium", *Phd Thesis, January 1998,University Toulouse III, France*

70. ANSYS® 10.0 Documentation

71. G. Strang, G. Fix, *An Analysis of the Finite Element Method,* Englewood Cliffs, Prentice-Hall, 1973.

72. Liwei Lin, Huey-Chi Chu, and Yen-Wen Lu, „A Simulation Program for the Sensitivity and Linearity of Piezoresistive Pressure Sensors", *Journal of Microelectromechanical Systems*, vol. 8, No. 4, December 1999, pp.514.

73. C. Fechner, A. Erlebach, A. Terterian, A. Scholze, M. Johnson, „New implantation tables for B, BF_2, P, As, In and Sb," *Proc. of 14th Ion Implantation Technology Conference*, 2002.

74. http://www.ee.byu.edu/cleanroom

75. Mordecai, *Nonlinear Programmin: Analysis and Methods*, Dover Publishing, 2003.

76. K. H. Elster, *Modern Mathematical Methods of Optimization*, Vch Pub, 1993.

77. J. Nocedal, S. J. Wright, *Numerical Optimization,* Springer, 2006.

78. T. F. Coleman, Y. Li; *SIAM J. Optimization*, vol. 6, (1996), pp 418-444.

79. Powell, M.J.D., "A Fast Algorithm for Nonlinearly Constrained Optimization Calculations," *Numerical Analysis*, ed. G.A. Watson, Lecture Notes in Mathematics, Springer Verlag, Vol. 630, 1978.

80. MATLAB® 2007 Documentation

81. E. Mezura-Montes and C. A. Coello, „A Numerical Comparison of Some Multiobjective-Based Techniques to Handle Constraints In Genetic Algorithms Departamento de Ingenieria Electrica," *CINVESTAV_IPN*, Mexico, Tech. Rep. EVOCINV-03-2002, Sep. 2002.

82. F. Y. Edgeworth, *Mathematical Physics*. London, U.K.: P. Kegan,1881.

83. V. Pareto, *Course D'Economie Politique*. Lausanne: F. Rouge, ,vol. I and II, 1896.

84. http://www.icyield.com

85. Papoulis, *Probability, Random Variables, and Stochastic Processes*, New York U.S.A., McGraw-Hill. pp. 113-114.

86. X. Li , I. Bao , and S. Stell, „Maskless Anisotropic Etclhing **-** A novelmicromachining technology for multilevel microstructures" *Proc. of Transducers 97 conference*, 1997.

87. S. M. Sze, *Semiconductor Devices: Physics and Technology*, Wiley, 1981.

88. K. Ikeda et al.**,** "Silicon pressure sensor with resonant strain gagesbuilt into diaphragm," in *Tech. Dig. 7th Sensor Symp*.**,** 1988, pp.55-58.

89. P. W. Barth, F. Pourahmadi, R. Mayer, J. Poydock, and K. Petersen,"A monolithic silicon accelerometer with integral air damping andoverrange protection," in *Tech. Dig., IEEE Solid-State Sensorand Actuator Workshop* (Hilton Head, SC), June 6-9, 1988, pp. 35-38.

90. M. A. Schmidt, „Wafer-to-Wafer Bonding for Microstructure Formation," *Proc. of IEEE*, vol. 6, No. 8, August 1998.

91. W. P. Maszara, "Silicon-on-insulator by wafer bonding: Areview," *J. Electrochem. Soc.*, vol. 138, no. 1, Jan. 1991, p. 341.

92. T. Abe, M. Nakano, and T. Itoh, "Silicon wafer bonding processtechnology for SOI structures," in *Proc. 4th Int. Symp. Siliconon-Insulator Technology and Devices*, 1990, p. 61.

93. J. Haisma, G. A. C. M. Spierings, U. K. P. Biermann, andJ. A. Pals, "Silicon-on-insulator wafer bonding-wafer thinningtechnological evaluations," *Jpn. J. Appl. Phys.*, vol. 28, no. 8, Aug. 1989, p. 1426.

94. www.suss.com

95. J. Bhardwaj, H. Ashraf, A. McQuarrie, *Annual meeting of the electorchemical society*, Kanada 1997.

96. Z. Duric, M. M. Smiljanic, K. Radulovic, Zarko Lazic, „Boron Redistribution During SOI Wafers Thermal Oxidation," *Proc. of 25th International Conference on Microelectronics MIEL '06*, 2006.

97. P. Morin, F. Wacquant, M. Juhel, C. Laviron, D. Lenoble, "Influence of the spacer dielectric processes on PMOS junction properties", *Mater Sci. Eng*., B 124-125, 2005, pp. 319.

98. R. B. Fair, „Physical Models of Boron Diffusion In Ultrathin Gate Oxides," *J. Electrochemical Society*, 144, 1997, pp.708.

Résumé:

Depuis 1954, où l'effet piézorésistif a été découvert dans Silicium, la démarche pour mesurer la pression a changé et de nouveaux dispositifs avec des performances remarquables sont apparus sur le marché. Grâce au développement des microtechnologies, une nouvelle famille de capteurs de pression piézorésistifs miniatures s'est ainsi progressivement imposée pour de nombreuses applications.

Même si le principe de fonctionnement des capteurs de pression piézorésistif en silicium reste le même depuis de nombreuses années, l'optimisation des capteurs pour une application donnée reste toujours une étape couteuse.

C'est pourquoi de nombreux travaux ont été effectués pour développer des outils de conception les plus performants possibles afin de limiter les phases de validation expérimentales. Il existe ainsi sur le marché des logiciels de simulation 3D multiphysiques qui permettent de prendre en compte aussi bien les phénomènes thermomécaniques qu'électriques qui sont nécessaires pour ce type de capteurs.

Malgré les progrès constants dans la puissance de calcul des ordinateurs, l'optimisation de ces capteurs par des méthodes de simulation élément fini peut s'avérer couteuse en temps si on veut prendre en compte l'ensemble des caractéristiques du capteur. C'est notamment le cas pour les jauges de contraintes en silicium dont le profil de dopage n'est pas constant dans l'épaisseur car les caractéristiques électriques et piézoélectriques dépendent du niveau de dopage.

Les travaux de cette thèse portent donc sur le développement d'un outil de simulation analytique qui permet d'une part une optimisation rapide du capteur par une technique multi-objectif semi-automatique et d'autre part une analyse statistique des performances pour estimer le rendement de fabrication potentiel.

Le premier chapitre décrit le contexte de ces travaux de thèse. Le second chapitre présente le principe de fonctionnement du capteur ainsi que tous les modèles analytiques mis en oeuvre pour modéliser le capteur. Ces modèles analytiques sont validés par des simulations élément finis. Le troisième chapitre porte sur l'outil d'optimisation et d'analyse statistique développé dans un environnement MATLAB. Le quatrième chapitre décrit la fabrication et la caractérisation des cellules de tests dont le comportement est ensuite comparé aux modèles analytiques. Ces caractérisations ont permis de montrer notamment que les modèles utilisés généralement pour décrire la dérive thermique des piézorésistances présentaient des erreurs notables. Des structures de tests spécifiques ont ainsi été mise en oeuvre pour avoir des données plus fiables. Finalement la dernière partie du manuscrit donne les conclusions générales ainsi que les perspectives de ce travail.

Les mots-clés:

MEMS, capteurs de pression piézoresistives, modélisation, optimisation

Abstract:

Since 1954, when the piezoresistive effect in semiconductors was discovered, the approach to the pressure measurement has changed dramatically and new devices with outstanding performances have appeared on the market. Along with the development of microtechnologies for integrated circuits, a new branch of MEMS called devices have stormed our world. One of the biggest branches of today's microsystems are pressure transducers which use the synergy of the piezoresistivity phenomenon and microfabrication technologies.

While the main idea of strain gauge-based pressure measurement has not changed over the last few decades, there has been always a need to develop the design methodology that allows the designer to deliver the optimized product in the shortest possible time at the lowest possible cost. Thus, a lot of work has been done in the field in order to create tools and develop the FTR (first time right) methodology. Obviously, the design of the device that best fulfills the project requirements needs an appropriate simulation that have to be performed at the highest possible details level. Such an approach requires the detailed model of the device and, in case of its high complexity, a lot of computing power. Although over the last decade the most popular approach is the FEM analysis, there are some bottlenecks in such an approach like the difficulty of the implanted layers modeling where the doping profile shape has to be taken into account especially in the coupled electro-mechanical analysis.

In this thesis, we try to present the methodology of the pressure sensor design which uses the analytical model of such a sensor that takes into consideration the nonuniform doping profile of the strain gauge, deals with the basic membrane shapes as well as with thermal and noise issues. The model, despite its limitations in comparison to the FEM one, gives trustworthy results which may be used for the reliable pressure sensor design in an extremely short time. In order to be quantitative, the analysis showing the drawbacks and advantages of the presented method in comparison to the FEM analysis using specialized tools like ANSYS ® and SILVACO-ATHENA® packages is also presented.

Then, the model is used in a multi-objective optimization procedure that semi-automatically generates the design of a sensor, taking into account project requirements and constraints. At the end, the statistical analysis that may be helpful to estimate the production yield is performed.

All three steps are included in the dedicated design and optimization tool created in a MATLAB ® environment and successfully tested. In the last section, the experimental results of fabricated samples are compared to those obtained by the developed tool.

Keywords:

MEMS, piezoresistive pressure sensors, modelling, optimization